On-Axis Acoustic Radiation Force-based Quantitative Elasticity for Skin Applications using a Bayesian Displacement Estimator

By

Kristy Michelle Walsh

Dissertation

Submitted to the Faculty of the

Graduate School of Vanderbilt University

in partial fulfillment of the requirements

for the degree of

DOCTOR OF PHILOSOPHY

in

Biomedical Engineering

December 17, 2022

Nashville, Tennessee

Approved:

Brett C. Byram, Ph.D.

Charles F. Caskey, Ph.D.

William A. Grissom, Ph.D.

Michael I. Miga, Ph.D.

Barbara A. Murphy, M.D.

To Cory and my parents, Kathy and Kel.

ACKNOWLEDGMENTS

I would like to thank Dr. Brett Byram for all his help and providing guidance and support during these many years. I am so grateful for having this time to learn for him and to complete this work.

I would like to thank my committee members, Dr. Caskey, Dr. Grissom, Dr. Miga, and Dr. Murphy, for their advice, expertise, and support throughout this process. Also, I would like to thank Dr. Mark Palmeri and Dr. Kathy Nightingale for their project insights and ideas that made this work possible. Additionally, I would like to thank Dr. Cynthia Reinhart-King and Stacey Satchell for helping me get to this point.

I would like to thank current and past members of the BEAM Lab, especially the OG members, Jaime Stanton and Kazuyuki Dei. I could not have asked for more helpful, smart, and encouraging people to go through this process with and I am so glad we met. A special thanks to the late Douglas Dumont who taught me everything from ultrasound basics to how to work on a compute cluster during my first year of graduate school. Thanks for patiently answering all my questions whenever I came knocking on the post-doc sanctuary door. To Katie, Abbie, Emelina, Chris, Preston, and Sigi, thanks for your encouragement, feedback, and camaraderie.

I would like to thank the funding sources that made this work possible, 5-T32-EB014841-03, and the Advanced Computing Center for Research and Education (ACCRE) at Vanderbilt University, Nashville, TN funded in part by NIH Grant S10 OD023680-01.

Last but not least, I would like to thank all my family and friends for their love and support.

TABLE OF CONTENTS

LIST OF TABLES

LIST OF FIGURES

Chapter 1

Background and Significance

1.1 Fundamentals of Diagnostic Ultrasound Imaging

Ultrasound is a medical imaging modality that is widely used in diagnostics and therapeutics. Diagnostic ultrasound can provide 2D or 3D cross-sectional images to visualize soft tissue structures in brightness mode (B-mode) or observe functional changes, such as blood flow, using Doppler imaging [1]. Ultrasound can also be used to image mechanical properties of tissues in elasticity imaging. Ultrasound has advantages over other imaging modalities, such as magnetic resonance imaging (MRI) and computed tomography (CT), because it is low-cost, real-time, and does not subject the patient to ionizing radiation [1]. This section will cover the fundamentals of conventional B-mode imaging and introduce elasticity imaging.

1.1.1 Conventional B-mode Ultrasound Imaging

Conventional brightness (B-mode) ultrasound imaging is used to visualize anatomical structures of soft tissue. Ultrasound typically uses a handheld transducer placed in contact with the body. The transducer has an array of piezoelectric elements that are electrically excited and transmit an acoustic signal into the tissue. The acoustic signal is a broadband signal that propagates in the tissue at frequencies of typically 1-15 MHz. These signals can be focused to a region of interest by applying time delays to the elements to create a converging wavefront [1].

The propagating sound wave is a physical longitudinal wave that travels through the medium by compression and rarefaction of particles [2]. If we consider the medium as a continuum, we can define the particles as small volume elements of matter, as shown

in Figure 1.1(a) [2]. The longitudinal waves can propagate in tissue that have elasticity (compressibility) and inertia (mass density) [3]. The speed of the longitudinal wave, i.e. the sound speed, depends on the properties of the medium [2]. As the sound wave propagates, it is attenuated through depth at each incidence by means of absorption and scattering. Ultrasound imaging relies on the portion of energy that is backscattered to the transducer. Scattering and reflection occur when the tissue has inhomogeneities in the acoustic impedance, Z. $Z = \rho_0 c$, where ρ_0 is the density and c is the sound speed of the tissue [1]. Scattering occurs when the acoustic particles are smaller than the wavelength of the sound wave. Reflection occurs when the particles are larger than the wavelength which includes most tissue structure boundaries within the body [1]. Ultrasound also relies on the fact that some sound energy is transmitted through an acoustic impedance boundary so that we can image deeper in tissue [1]. However, if there is a severe acoustic impedance mismatch, such as between tissue and air, the sound cannot penetrate further, which is why ultrasound tends to fail in regions such as the lungs or bowels.

The acoustic energy that is backscattered from the tissue is received by the transducer. The received signal from each element is time-delayed for a certain lateral location and depth [2]. To create a radiofrequency (RF) line or amplitude line (A-line), the signals from all delayed elements are summed together [1]. To create an image, the lateral transmit focus is swept across the field of view to generate RF lines for each lateral focus, forming a 2D image. The RF amplitude image is then log-compressed to generate a B-mode image. This delay-and-sum technique is a common method of ultrasound beamforming. B-mode images can be generated in real-time on a monitor to show a cross-section of the tissue echo amplitude. B-mode images show tissue structures with variations in acoustic impedance. The axial dimension is the prominent direction of the longitudinal wave propagation from the transducer into the body. The lateral direction is orthogonal to the axial direction and is the second dimension of a 2D cross-sectional image plane. In the 2D image, the elevational direction is the slice thickness [1].

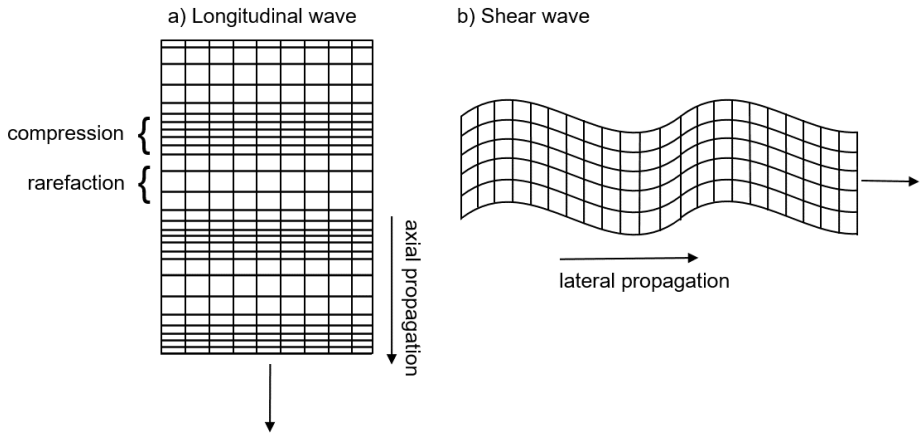

Figure 1.1: Particle displacement for waves propagating in an isotropic, solid medium. (a) Plane longitudinal (compressional) wave, (b) shear (transverse) wave. The particles are small volume elements of matter with constant properties. Particle displacement in longitudinal waves is in the same direction as the wave propagation. Particle displacement in shear waves is in the orthogonal direction.

1.1.2 Ultrasound Elasticity Imaging

Quantifying tissue stiffness is clinically useful in staging or monitoring many diseases and their treatments. Manual palpation can be the first indicator of a disease that causes changes in the mechanical properties of tissues, but it can be relatively subjective. Elasticity imaging evolved to better measure and visualize tissue mechanical properties.

First, a review of soft tissue biomechanics will describe the assumptions and elastic moduli commonly used to quantify elastic properties. In soft tissue, the stiffness is defined as the resistance of a material to deflections [4]. Most elasticity imaging methods describe the material's elastic moduli by relating stress and strain [5]. Stress represents a force per unit area that counteracts the applied force and strain represents the change in length per unit length of a material experiencing deformation [5]. To derive a constitutive equation relating stress and strain, we have to make some assumptions. We often assume the tissue is homogeneous, isotropic, linear, and elastic [6]. Under the small deformation approximation

and ignoring viscous forces, the constitutive equation relating stress and strain is,

$$\sigma_{ij} = \lambda e \delta_{ij} + 2\mu \varepsilon_{ij} \tag{1.1}$$

where σ_{ij} is the stress tensor, e is the dilatation (volume change), δ_{ij} is the identity matrix, ε_{ij} is the strain tensor, and λ and μ are Lamé constants [4, 5, 6]. Now we have a relationship using Lamé constants, but it is also common in elasticity to use engineering constants, such as Young's modulus [4]. Under uniaxial stress where only one normal stress component is nonzero, we can relate Young's modulus, E, to shear modulus, μ, by,

$$E = 2(1+\nu)\mu = 3\mu \tag{1.2}$$

where ν is the Poisson's ratio. The Poisson's ratio is the negative ratio of lateral to longitudinal strain and describes the material's desire to maintain volume. We often assume soft tissue, which is dominated by water, to be nearly incompressible tissue and has a Poisson's ratio between 0.495 and 0.4999 [4]. Young's modulus (E) and shear modulus (μ) are elastic moduli commonly used in elasticity imaging to describe the tissue's resistance to deformation and resistance to shear.

Elasticity imaging involves a source of excitation to deform the tissue and a way to monitor the tissue response. The mechanical excitations can be static, dynamic, or physiological [4]. Some of the first ultrasound-based elasticity methods used a static excitation to deform tissue using an external force, such as the transducer, to compress the tissue of interest (strain imaging) [7, 8]. In strain imaging, the tissue is compressed quasi-statically, monitored using ultrasound, and the strain field is reconstructed [4]. This method is useful in the easy implementation of displacement, but it relies heavily on uniform compression and accurate boundary conditions [4]. Dynamic elasticity imaging uses an internal or external applied stress that can be harmonic or impulsive [4]. Some methods use a mechanical excitation to cyclically displace tissue, such as in sonoelasticity, but the clinical applicabil-

ity is limited due to the mechanical excitation configurations and the lack of coupling to deeper tissues [4, 5, 9]. FibroScan® (EchoSens, Paris, France) is a transient elastography technique that can assess fibrosis in chronic liver disease [10, 11]. FibroScan® vibrates the tissue mechanically and uses ultrasound to measure the displacement through depth in the liver tissue [10, 11]. This method works well in the liver fibrosis application. However, it is difficult in obese patients and it cannot be performed using a clinical scanner. Other methods employ physiological motion, such as breathing, cardiac motion, or arterial pulsation, but those methods are limited to the applications of these particular structures and the distribution of stress is unknown [4, 5, 12]. An impulsive acoustic method, called acoustic radiation force (ARF), has been developed to generate a targeted force to deform a region of interest in tissue using a focused ultrasound beam [5, 13]. This dissertation will focus on impulsive acoustic radiation force excitations being monitored with ultrasound.

1.2 ARF-based Elasticity Imaging

Acoustic radiation force (ARF)-based elasticity imaging can provide stiffness information that is less operator dependent and at deeper depths which may be inaccessible by palpation [5, 13]. Prominent clinically-used ARF-based methods include acoustic radiation force impulse (ARFI) imaging, shear wave elasticity imaging (SWEI), and Supersonic Shear Imaging (SSI). ARFI imaging uses ultrasonic tracking techniques to measure tissue displacement within a region of excitation following an ARF excitation [14]. SWEI is a quantitative ARF-based technique that measures the speed of the shear wave speed produced by the ARF excitation. From the shear wave speed, tissue elastic moduli can be found using a mechanical model [15]. Other techniques exist using multiple pushing schemes, such as Supersonic Shear Imaging (SSI) which focuses the acoustic push at multiple on-axis depths to generate a constructively interfering shear wave that travels across several centimeters of tissue [16]. While multiple push locations may improve these techniques in certain applications, they will not be covered in this dissertation. The following

section will provide more detail on the ARF generation, ultrasonic methods to monitor the deformation response, and the two imaging methods: acoustic radiation force impulse (ARFI) imaging and shear wave elasticity imaging (SWEI).

1.2.1 Acoustic Radiation Force (ARF)

An acoustic radiation force is created when an acoustic wave transfers momentum into the propagation medium by absorption and/or reflection [17]. In soft tissues where the majority of attenuation is caused by absorption [18], the acoustic radiation force magnitude, $\vec{F}$ [kg/(cm^{2}s^2)], can be described as,

$$\vec{F} = \frac{2\alpha\vec{I}}{c}, \tag{1.3}$$

where $\vec{I}$ [W/cm^2] is the time-average intensity at a given spatial location, α [dB/cm/MHz] is the attenuation coefficient, and c [cm/s] is the speed of sound [17, 19]. When the tissue absorbs the energy from the acoustic radiation force excitation, it induces displacements in the direction of the longitudinal wave propagation within the focal region of the acoustic beam. These excitations create mechanical transverse waves called shear waves that propagate laterally away from the region of excitation (See the particle displacement in a shear wave in Figure 1.1(b)). ARFI imaging measures the displacement induced at the region of excitation and SWEI measures displacement caused by the shear wave at lateral locations.

1.2.2 Monitoring the Deformation Response

The quality of ARF-based stiffness estimation techniques greatly depends on the ability to measure tissue displacement induced by the applied force. After the ARF push is applied, conventional pulse-echo techniques monitor the tissue response. The tissue motion can be measured using displacement tracking algorithms that estimate displacement between two signals. Typically, we estimate displacement between a reference signal and a signal from

the same location after a time delay which is called the tracked signal. Correlation-based methods, such as normalized cross-correlation, measure the similarity between windowed lengths of RF data from the reference and tracked signals [20, 21]. The time-shift that results in the maximum cross-correlation value indicates where the two signals are most similar and represents the time used to form a displacement estimate [20, 21]. Phase-shift methods utilizes less memory-intensive in-phase and quadrature (IQ) data [5]. The phase-based methods use autocorrelation to estimate the displacement between a reference and tracked signal by measuring the average phase-shift with respect to the central frequency [21, 22, 23]. Normalized cross-correlation has better performance than phase-based time delay estimators, but has a higher computational cost [20, 21]. The performance of these estimators can be affected by a number of factors causing bias and jitter in the displacement estimates (i.e. noise, bandwidth, kernel size, sampling frequency, and signal decorrelation) [21]. For unbiased time-delay estimators operating on RF data, a theoretical performance limit predicting the standard deviation of the jitter is described by the Cramér-Rao lower bound [24]. Bayesian methods have been employed to reduce variance and perform better in a mean-square error sense than a Cramér-Rao lower bound-limited estimator by using a biased estimation scheme [25, 26]. This dissertation will discuss the advantage of using a Bayesian displacement estimator for this application as compared to normalized cross-correlation.

1.2.3 Acoustic Radiation Force Impulse (ARFI) Imaging

A typical ARFI image is a displacement image at a given time after the ARF excitation. To generate an ARF significant enough to displace tissue, the ultrasonic pulse is longer and higher intensity than a conventional imaging pulse [13]. At a single lateral location, a typical ARFI sequence consists of a reference pulse, a pushing pulse, and tracking pulses [4, 13]. The reference pulses are conventional imaging pulses (1 cycle, <1 μs) to establish a reference for the tissue before the ARF is applied. The pushing pulses are the higher

intensity, longer duration pulses (100-1000 cycles, <1 ms) to generate an ARF to displace tissue in the region of excitation. The tracking pulses are conventional imaging pulses, the same used for the reference pulses, immediately following the pushing pulse to monitor the tissue deformation response and recovery. Figure 1.2 shows an illustration of the reference, ARF push, and tracking pulses and the ARF-induced displacement measured over time. This ensemble of reference, pushing, and tracking pulses can be translated laterally to form

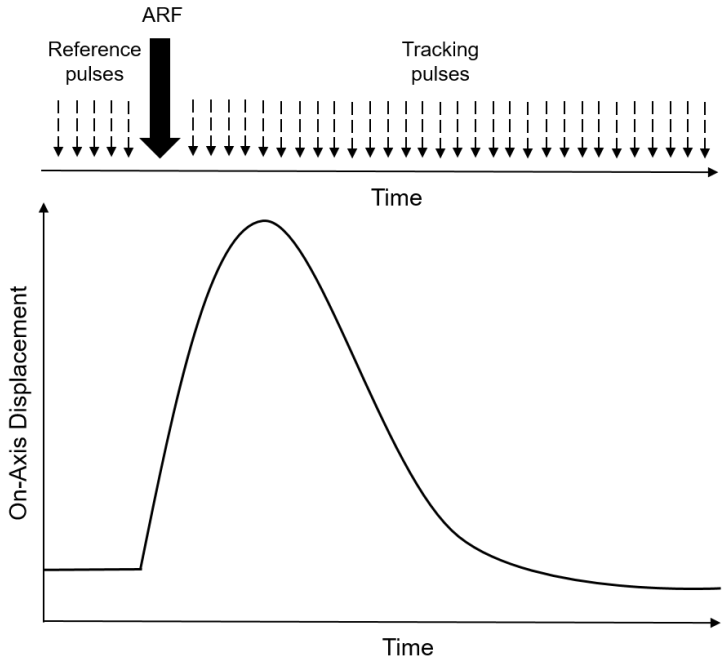

Figure 1.2: Typical acoustic radiation force (ARF) pulse sequence for one location. Conventional imaging reference pulses are taken to monitor tissue before the ARF push. The ARF push is applied and induces displacement. Then, tracking pulses, same as the reference pulses, measure the tissue's response over time.

a 2D image (lateral versus axial) of the deformation response. The typical displacement in the tissue is around 10-20 μm and is found using methods described in Section 1.2.2. Images are generated to show displacement at a specific time after the push, the time it takes to reach maximum displacement, or maximum displacement [5]. Typically, softer regions take longer to recover and have higher displacement, and stiffer regions recover more quickly and have smaller displacements [4, 13, 5]. ARFI imaging shows qualitative

stiffness information relative to the surrounding tissue.

Despite being a qualitative technique, ARFI imaging has been successful in many clinical areas, such as in abdominal imaging, and breast, prostate, and lymph node assessment [13]. ARFI imaging is also used to monitor the effects of treatment using radiofrequency (RF) ablations in the liver and cardiovascular tissues [27, 28]. ARFI imaging can also show mechanical properties of the arterial walls and plaques to help characterize atherosclerosis [29, 30]. ARFI imaging is useful clinically by giving B-mode images the additional contrast of elasticity information. However, it lacks the ability to give quantitative measurements of elasticity.

1.2.4 Shear Wave Elasticity Imaging (SWEI)

SWEI is a quantitative ARF-based elasticity technique that uses a mechanical model to convert shear wave speed to shear modulus [15, 31]. In SWEI, the tissue at a focused region of interest is excited and displaced using an ARF [15, 31]. The ARF excitation creates mechanical transverse waves called shear waves that propagate laterally away from the region of excitation. The shear waves are a finite train of equivoluminal waves that displace particles in the axial direction and propagate laterally, or perpendicular to the displacement (See Figure 1.1(b)) [2, 6]. The shear wave speed provides information about the tissue that was displaced at the focal region. Assuming the tissue is linearly elastic and isotropic, the shear wave speed, c_T, can be related to the tissues shear modulus, μ, by

$$c_T = \sqrt{\frac{\mu}{\rho}}, \tag{1.4}$$

assuming a constant density, ρ [6]. Common methods to reconstruct shear modulus use Equation 1.4 to convert the shear wave speed to shear modulus [31, 16]. In these shear wave elasticity methods, the shear wave is observed as a displacement outside the region of excitation (i.e. tracking pulses are positioned lateral to the push pulse). To find the shear

wave speed, time-of-flight-based methods often track the shear wave displacement and find the velocity based on its spatial and temporal locations [32, 33, 34]. Figure 1.3 shows the lateral location where the shear wave displacement is typically tracked at the green horizontal box in the third time frame. SWEI measures shear wave speed more accurately in mostly homogeneous regions where the shear wave is not as disrupted by tissue boundaries or structures. As one example, ARFI and SWEI have been commercialized on Siemens ultrasound systems as part of the Virtual Touch tissue quantification tool which provides qualitative ARFI images with quantitative stiffness information in the SWEI region of interest [35].

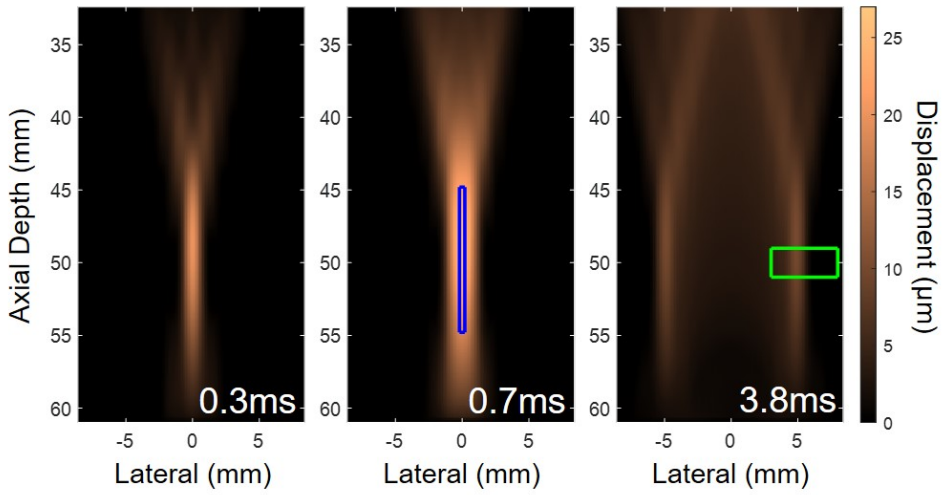

Figure 1.3: ARF simulation showing propagation of displacements over time. The green horizontal box in the third time frame shows where shear wave displacements are measured to calculate shear wave speed. The blue vertical box in the second time frame shows where on-axis displacements are measured along the axis of the ARF excitation region.

Clinically, quantifying stiffness is useful in staging diseases where the severity of the disease is linked to changes in stiffness. For example, shear wave speed can be used as a quantitative imaging biomarker for staging diseases, such as liver fibrosis [36, 37]. SWEI has been used to measure stiffness in breast, prostate, thyroid, muscular, lymph nodes and various abdominal tissue [13, 31, 38, 39].

1.3 Clinical Problem: Measuring Skin Elasticity

An area of ultrasound elasticity imaging that needs improvement is accurately measuring skin elasticity. Ultrasound elasticity imaging in the skin has been difficult due to the skin's thin nature and complicated surrounding structures, including subcutaneous fat, muscle, and bone [40, 41]. The skin structure also introduces new challenges to the mechanical models in elasticity because it is composed of thin layers bounded to the substrate, or subcutaneous tissue [40, 42]. This dissertation presents an acoustic radiation force-based elasticity method to quantify skin stiffness. The clinical goal will be to provide an easy way to document elasticity changes in post-treatment head and neck cancer patients who experience stiffening of skin and underlying muscles in the treatment areas due to developing fibrosis.

1.3.1 Lymphedema and Fibrosis in Post-Treatment Head and Neck Cancer Patients

Head and neck cancer (HNC) is the sixth most common cancer worldwide with over half a million survivors alive in the United States [43, 44]. These cancers affect critical areas, such as the mouth, tongue, larynx, oral pharynx, upper esophagus, sinus, face, and facial structures [45]. HNC often requires multi-modality therapy which includes some combination of surgery, radiation, or chemotherapy to attempt to cure the patient [45]. The epidemic of human papillomavirus-related HNCs along with early detection and better treatments have increased the number of HNC survivors [46, 47]. Although many patients are cured of cancer, the treatment leaves survivors with disrupted lymphatic structures and soft tissue damage. Therefore, HNC survivors are at a high risk for developing secondary lymphedema and fibrosis [48, 47]. Lymphedema is the swelling of soft tissues due to an inability to drain lymphatic fluid. Fibrosis can occur from radiation and soft tissue damage that leads to a local inflammatory response and extracellular matrix deposition causing stiffening of tissue structures [49]. Lymphedema and fibrosis (LEF) can occur in

certain areas individually or together. Although they are thought to have different underlying mechanisms, LEF can aggravate each other by contributing to soft tissue damage and the inflammatory response [50]. Without early detection and management of lymphedema, the affected tissues can become fibrotic [51, 52]. Developing lymphedema and fibrosis introduces more burden to the patient by causing new symptoms and worsening post-treatment symptoms that the patient is already experiencing (i.e. functional impairment, reduced range of motion, pain, difficulty eating, poor nutrition, depression, and an overall decreased quality of life) [53]. At most institutions, post-treatment HNC patients are not monitored for secondary lymphedema and fibrosis. Therefore, it is important to show documentation of this clinical problem and identify a reliable tool to monitor and diagnose LEF before it progresses.

Characterizing the stages of LEF could lead to an improvement in the standard of care in post-treatment HNC patients by monitoring the stages of the disease and intervening before it progresses. Currently, methods of staging LEF are not widespread. Deng et al. at Vanderbilt University has developed a Head and Neck External Lymphedema and Fibrosis Assessment Criteria that categorizes the tissue types as having lymphedema, fibrosis, or both and the level of severity [47, 44, 52]. The grading system relies on visual and digital inspection of tissue swelling, tightness, and compliance of affected regions in the face and neck [47, 44]. Deng et al. also developed a Head and Neck Lymphedema and Fibrosis Symptom Inventory to capture the symptoms and functional loss in this population [54]. These studies have been useful in creating an assessment criteria and showing significant patient burden. However, the criteria are subject to interrater and intrarater variability. There are efforts currently to validate the patient self-assessments of symptoms and clinician-reported outcomes with a quantitative imaging modality [54, 50, 44, 55]. Compared to CT and MRI, ultrasonography is favorable for this task because it could be used more easily in post-treatment check-ups and it is inexpensive and does not use radiation. Ultrasound can be used to show changes in size (i.e. swelling) in the soft tissue structures

experiencing lymphedema. For characterizing the level of fibrosis, ultrasound elasticity methods are being explored.

1.3.2 Challenges in Measuring Skin Elasticity

Currently, it is challenging to quantify the elasticity in skin due to the boundary conditions and complex structure. Some groups use an external vibration or apply a displacement to the surface of the skin and measure the response using ultrasound. Similar to the FibroScan® system for the liver, a dynamic elastography technique using a vibrator has been tested in the skin, but the proximity of the skin to the transducer and vibrator make it difficult to quantify any shear wave propagation in the skin layer [56]. Another method that has been tested in skin is strain imaging which applies a quasi-static displacement to the tissue surface using the ultrasound transducer and measures the strain. [57, 58]. Others have applied a vacuum suction to the tissue and use high frequencies, around 20 MHz, to measure the strain response [59]. These methods only estimate strain relative to the surrounding tissue and are not quantitative, or able to compare between patients [59, 57, 58]. They can also be subject to operator variability and often require a contralateral control measurement on the patient which may not be available in all patient populations if the disease is bilateral. Acoustic radiation forced-based methods can be used to induce a reproducible displacement. Currently, the most common method being developed to quantify the elasticity of skin is SWEI [41, 60, 61, 62]. However, shear wave speed is difficult to measure in heterogeneous and anisotropic regions where there are changes in stiffness and mechanical behavior based on orientation [31, 4]. Also, lesions or tissue boundaries have complex shear wave reflections that corrupt the shear wave speed measurements [4]. From these factors and the thin nature of the skin, SWEI measurements in the skin are biased based on the skin thickness [41]. Some groups attempt to offset this layer-dependent bias by normalizing the shear wave speed measurements by the width of the skin layer, but they still rely on measuring the velocity of a complex shear wave and do not have an analytical

model to convert to shear modulus [41, 61, 62]. Table 1.1 shows quantitative skin elasticity measurements from a few different groups. The suction and indention methods produce slightly different shear modulus estimates compared to the shear wave speed-derived estimates in healthy skin. The estimated moduli can depend on the applied force to the tissue. Additionally, Table 1.1 shows results from patients with systemic sclerosis and sclerotic graft versus host disease (GVHD). The modified Rodnan skin score (mRSS) is used to access skin thickness and disease involvement of systemic sclerosis with higher numbers meaning more disease involvement. We see an increase in shear wave speed and shear modulus with sclerotic diseases. However, the shear wave speed may not be the most accurate when there is a change in skin thickness. Yun Lee et al. showed there is a bias in shear wave speed based on the skin thickness and computed a normalized shear wave speed which greatly increases the measured moduli [41]. To get accurate measurements of elasticity from patient to patient, there needs to be an improved quantitative measurement technique. This dissertation will develop an ARF-based elasticity technique that measures on-axis displacement rather than lateral shear wave speed to reduce the effects of a complicated shear wave propagation in the skin. (Figure 1.3 shows the on-axis location in the box shown on the second time frame.) The impact of this technique would be early detection of fibrosis that may not be noticed in a physical examination of the skin. This could improve patients' quality of life, symptom management, and survival by informing the need for therapy before fibrosis progression.

Table 1.1: Quantitative skin elasticity estimates from different groups. Measurement results are reported in shear wave speed (m/s) or Young's modulus (kPa) and show the mean value and/or standard deviation or range. In the right column, the measurements are converted to shear modulus using Equation 1.4 under the assumptions that the tissue is linearly elastic and isotropic.

Reference, Method	Measurement: Shear Wave Speed (m/s) or Young's Modulus (kPa)	Shear Modulus (kPa)
Pederson et al. 2003 [63], DermaLab suction cup	Healthy (ventral side of forearm): Youngs Modulus: 5.10 (4.12-6.08) kPa	Healthy: 1.7 (1.37-2.03) kPa
Pailler-Mattei et al. 2008 [42], Indention with two-layer model	Healthy (inner forearm): Youngs Modulus: 4.5-8 kPa	Healthy: 1.5-2.3 kPa
Santiago et al. 2016 [64], SWS Virtual Touch	Healthy (anterior chest): 2.3 (0.7) m/s, Systemic Sclerosis (anterior chest): 2.7 (1.1) m/s, Healthy (upper arm): 2.2-2.3 (0.4-0.5) m/s, Systemic Sclerosis (upper arm): 2.5-2.9 (1.1-1.2) m/s	Healthy (chest): 5.3 (0.5) kPa, SSc (chest): 7.3 (1.2) kPa, Healthy (arm): 4.8-5.3 (0.2-0.3) kPa, SSc (arm): 6.3-8.4 (1.2-1.4) kPa
Hou et al. 2015 [60], SWS	Controls: 1.630 (1.420, 1.895) m/s, mRSS 0: 1.870 (1.505, 2.440) m/s, mRSS 1: 2.390 (1.800, 2.760) m/s, mRSS 2: 2.600 (2.220, 2.880) m/s, mRSS 3: 2.960 (1.750, 3.865) m/s	Controls: 2.66 (2.02, 3.59) kPa, mRSS 0: 3.50 (2.27, 5.95) kPa, mRSS 1: 5.71 (3.24, 7.62) kPa, mRSS 2: 6.76 (4.93, 8.29) kPa, mRSS 3: 8.76 (3.06, 14.9) kPa
Yun Lee et al. 2015 [41], Normalized SWS	Healthy (upper arm): 1.9-2.3 (0.2-0.3) m/s, Sclerotic GVHD (upper arm): 4.3-5.1 (0.2-0.6) m/s	Healthy: 3.6-5.3 (0.04-0.09) kPa, Sclerotic GVHD: 18.5-26.0 (0.04-0.4) kPa

Chapter 2

On-Axis Acoustic Radiation Force-based Elasticity: Preliminary Studies

This work was originally presented at and published in part as a proceedings paper in [65]: Walsh, Kristy, et al. "On-axis acoustic radiation force-based stiffness estimation in phantoms " *Proc. IEEE Int. Ultrason. Symp. (IUS)* (2016): 1-3.

2.1 Introduction

To address the issue of complicated shear wave propagation in a thin medium, like the skin, we present an on-axis stiffness estimation approach that can provide quantitative shear modulus estimates. To estimate shear modulus, we use a simulated look-up table that models the time-to-peak on-axis displacement for a certain imaging configuration. Measuring displacement at the location of the push requires an advanced displacement estimator. Palmeri et al. first performed this technique using normalized cross-correlation to estimate displacement [66]. The results had too high of a variance in displacement estimates to make feasible shear modulus estimates. This dissertation will apply a more advanced displacement estimation technique, a Bayesian displacement estimator. This chapter will describe the two displacement estimators used in this work: normalized cross-correlation and the Bayesian displacement estimator. Additionally, this chapter will introduce the on-axis stiffness estimation look-up table and show initial results.

2.2 Displacement Estimation

2.2.1 Bayesian Displacement Estimation

The quality of ARF-based stiffness estimation techniques greatly depends on the ability to measure displacement. Bayesian methods have been employed to reduce variance

and perform better in a mean square error sense than a Cramer-Rao Lower Bound (CRLB) limited estimate by using a biased estimation scheme [24, 25, 26, 67, 68]. We apply the Bayesian displacement estimator to RF data to calculate displacement and reduce estimation variance. The Bayesian displacement estimator uses the Bayes' Theorem to estimate a posterior probability density function (PDF) of a displacement estimate, τ_k, given the observed RF data, x, shown here as,

$$P_k(\tau_k|x) = \frac{P_k(x|\tau_k)P_k(\tau_k)}{P_k(x)}, \tag{2.1}$$

where $P_k(x|\tau_k)$ is the likelihood function, $P_k(\tau_k)$ is the prior PDF, and $P_k(x)$ is the marginal likelihood PDF [67]. To find the displacements, τ_k, that maximize the posterior PDF, we can describe the terms in Equation 2.1 in the log-domain as,

$$\ln(P_k(\tau_k|x)) \propto -\frac{1}{4\sigma_n^2}\sum_{s=0}^{M-1}(r_k[s] - t_k[s;-\tau_k])^2 - \frac{1}{p\lambda^p}\sum_{k,j\in B} w_j|\tau_k - \tau_j|^p, \tag{2.2}$$

where the log likelihood is the sum-squared difference between the reference RF signal, $r_k[s]$, and the tracked RF signal, $t_k[s;-\tau_k]$, delayed by $-\tau_k$ over the kernel length M. The likelihood term is weighted by an adaptive noise term, σ_n^2, to account for the noise and decorrelation in both RF signals as shown here,

$$\sigma_n^2 = \frac{P_{RF}}{SNR_\rho + 1}, \tag{2.3}$$

where P_{RF} is the power of the RF signal and SNR_ρ is derived from the peak correlation-coefficient estimate of the SNR shown here as,

$$SNR_\rho = \frac{\rho_{max}}{1-\rho_{max}}, \tag{2.4}$$

where ρ_{max} is the peak of the normalized cross-correlation between the two signals over the kernel k [25, 26]. The prior PDF term is represented in Equation 2.2 as a weighted prior term where w_j weights adjacent displacement estimates, τ_j, when calculating the current displacement estimate, τ_k, for a neighborhood B [69]. This weighted prior term also has tuning parameters λ and p which modulate the distribution of the prior PDF. In the Bayesian displacement estimator, a p of 2 gives the prior PDF a Gaussian distribution which is computationally faster and tends to more accurately preserve the axial displacement profile in a homogeneous region [67]. We chose λ empirically based on the median axial SNR_ρ and the maximum displacement of the prior. This allows the algorithm to scale the width of the prior without biasing the result away from the true displacement [67]. To find the displacement estimates, we apply the *maximum a posteriori* principle to Equation 2.2 for all N kernels in the dataset, shown as,

$$\hat{\vec{\tau}} = \text{argmax} \sum_{k=0}^{N-1} \ln P_k(\tau_k|x), \tag{2.5}$$

which maximizes the global log-posterior probability of displacements given our data. To solve for the vector of displacement estimates, we used a pre-existing MATLAB program called minFunc written by Schmidt (2005) that offers a variety of nonlinear unconstrained minimization solvers [70]. We used the quasi-Newton algorithm. Other methods to solve the Bayesian displacement estimator and improve computational time will be discussed later in the dissertation.

2.2.2 Normalized Cross-Correlation

We also computed on-axis displacements using the commonly used unbiased time-delay estimator, normalized cross-correlation [20, 21]. The normalized cross-correlation function, $c(j)$, between the reference signal, y_r, and the shifted signal, y_s, shifted by j

samples is described as,

$$c(j) = \frac{\sum_{i=-M/2}^{M/2} [y_r(i) - \bar{y}_r][y_s(i+j) - \bar{y}_s(j)]}{\sqrt{\sum_{i=-M/2}^{M/2} [y_r(i) - \bar{y}_r]^2 \sum_{i=-M/2}^{M/2} [y_s(i+j) - \bar{y}_s(j)]^2}}, \tag{2.6}$$

where $\bar{y}_r$ is the mean of the reference signal in the window M and $\bar{y}_s(j)$ is the mean of the shifted signal in the window shifted by j samples [21]. The peak of the correlation function is where the two signals are most similar to each other which corresponds to the displacement estimate.

Due to discrete sampling of signals in time, the true maximum of the normalized cross-correlation function may be between samples. Upsampling and interpolation techniques are used to improve accuracy of subsample estimates by reducing false peak errors and aliasing [21]. Before computing the normalized cross-correlation function, we upsampled the RF data (typically by a factor of three from 40 MHz to 120 MHz) using cubic splines [21]. To find the peak of the normalized cross-correlation function in Equation 2.6, we also performed a parabolic fit of the peak to get subsample displacement estimates [71].

Although normalized cross-correlation performs well in many applications, the Bayesian displacement estimator helps reduce the jitter caused by thermal noise and shearing-induced decorrelation. Figure 2.1 shows an example of this which has also been shown previously [67, 72, 65]. In a homogeneous tissue-mimicking phantom, Figure 2.1 shows on-axis displacement measurements at 1.6 ms after the ARF push and shows that the jitter is reduced when using the Bayesian algorithm. The Bayesian displacement estimator has also been shown to provide an improvement in displacement SNR and contrast-to-noise ratio over normalized cross-correlation in an SNR-limited environment [68].

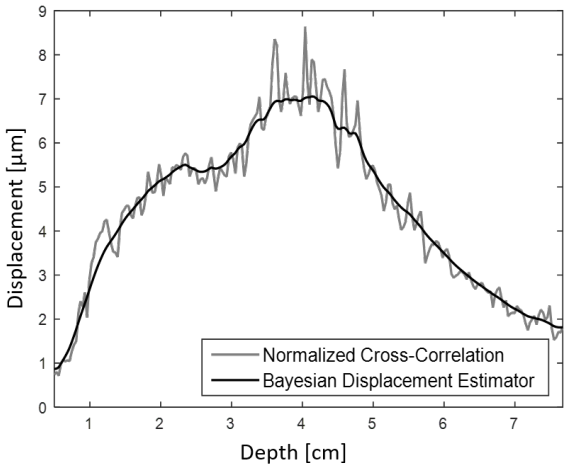

Figure 2.1: On-axis displacements through depth for one tissue-mimicking phantom 1.6 ms after the ARF push. Displacements are calculated using the Bayesian displacement estimator (black) or normalized cross-correlation (gray). The Bayesian displacement estimator reduces the variance in displacement estimates.

2.3 Preliminary On-Axis Stiffness Estimation Results

2.3.1 On-Axis Stiffness Estimation Approach

In the on-axis stiffness estimation method, we only measure on-axis displacement and quantify stiffness by using a look-up table based on simulations to reconstruct shear modulus. Like SWEI, we use acoustic radiation force to induce displacement; however, we only measure displacement along the axis of excitation shown in Figure 1.3 as the blue vertical box in the second time frame. After the ARF excitation is applied, the focal region reaches a maximum displacement that decays in magnitude as the shear waves propagate laterally away from the region of excitation. We measure the on-axis displacement through time and find the time-to-peak displacement. The time-to-peak displacement depends on depth and the spatial distribution of the excitation. Because we are not measuring the shear wave propagation, we cannot use Equation 1.4 to relate the shear wave speed to shear modulus. Instead, we find the time of peak on-axis displacement and use a lookup table with time-to-peak displacement as a function of depth for a certain excitation pulse and displacement sensing sequence [66]. Using a look-up table to relate the displacement to shear modu-

lus avoids assumptions limited by the analytical Gaussian solution for an ultrasound beam [16]. Measuring only on-axis displacements can simplify hardware required for a stiffness estimate. However, the challenge with measuring at the region of excitation is the large variance in the displacement estimates [66]. Consequently, this technique had a substantially higher variance in shear modulus estimates than traditional lateral shear wave-derived estimates [66]. To improve this, we apply an advanced displacement estimation technique using a Bayesian displacement estimator, that has been shown to reduce displacement estimation variance [25, 26, 72, 65].

2.3.2 Finite Element Simulations

Finite element responses to acoustic radiation force were simulated to generate a stiffness look-up table. The simulations mimic the response of tissues of varying stiffness to a certain transducer ARF push and tracking configuration. We simulated a range of stiffnesses in shear moduli from 1-15 kPa. Tissue properties were simulated using a 2,400,000 element, 3D mesh extending 8.0 cm axially, 1.5 cm laterally, and 0.2 cm in elevation. To ensure the elevation dimension had a sufficient width that did not create first-order effects, we also simulated meshes of 1, 3, 4, and 8 mm elevation depths. Figure 2.2 shows simulated on-axis displacements through time at the depth of the maximum displacement for each model thickness. Between the 2 mm and the 8 mm elevation depth cases, the difference in maximum displacement was only 0.03%, and there was no change in the location of time-to-peak displacement for widths of 2 mm and larger. The 1 mm and 8 mm cases had an 11% difference in peak displacement and a shift in the time-to-peak displacement that could create errors in this method. The 2 mm elevation depth was chosen to be sufficient for this study.

The material was modeled as linearly elastic, homogeneous, and isotropic with a constant density of 1.0 g/cm^3 and a Poisson's ratio of 0.495. Field II was used to calculate the pressure field of the experimental transducer configuration and the parameters are shown in

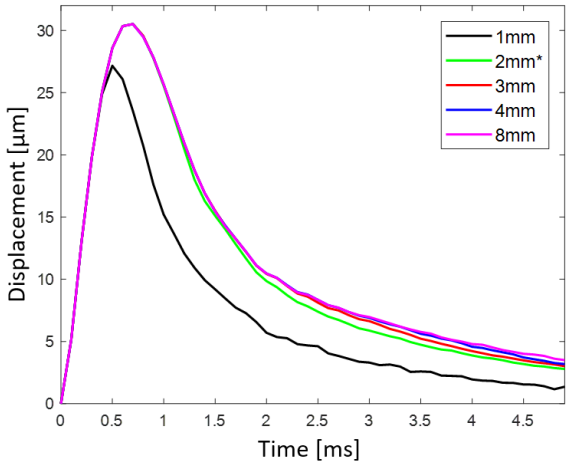

Figure 2.2: Mesh thickness comparison showing the on-axis displacement through time at the depth of maximum displacement. The difference in maximum displacement was 0.03% or less for 2, 3, 4, and 8 mm models, and there was no change in the location of time-to-peak displacement in those widths. The 1 mm and 8 mm cases had an 11% difference in peak displacement and a shift in the time-to-peak displacement that could create errors in this method. The 2 mm elevation depth (starred) was used for the model mesh in this work.

Table 2.1 [73]. LS-DYNA (Livermore Software Technology Corporation, Livermore, CA) was used to simulate the displacements induced by the ARF push [19]. An example of the FEM simulated displacements before tracking are shown in the left column of Figure 2.3. The 3D volume of displacements was imported into Field II to displace the point scatterers. The density of scatterers was 150,000 scatterers/cm^3 and over 50 scatterers per resolution cell to ensure fully developed speckle. We also used Field II to simulate on-axis ultrasonic tracking using the Siemens CH4-1 probe configuration [74].

2.3.3 Stiffness Look-up Table

The stiffness look-up table is based on the time-to-peak displacement at each depth for a range of stiffnesses. To generate the look-up table, we simulated 20 independent speckle realizations of each stiffness for shear moduli of 1, 3, 5, 7, 9, 11, 13, and 15 kPa using the method described in 2.3.2 and the parameters in Table 2.1. After simulating ultrasonic tracking using Field II to get received RF data, we use either the Bayesian displacement

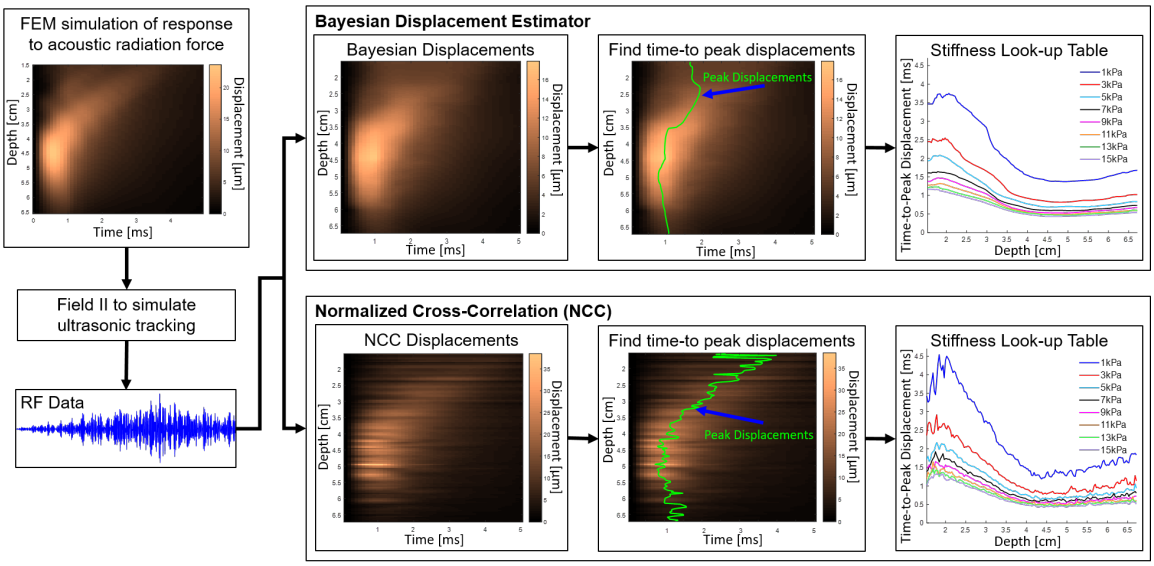

Figure 2.3: Overview of the generation of stiffness look-up tables. The first column shows on-axis displacements of an FEM simulation response to ARF. Then, we track the displacements using Field II to get on-axis RF data. We use either the Bayesian displacement estimator or normalized cross-correlation (NCC) to estimate the displacements. Next, we find peak displacement at each depth to get a time-to-peak displacement curve (shown in green). We simulate 20 realizations for each stiffness (shear modulus of 1-15 kPa) and average the time-to-peak displacement curves to generate the stiffness look-up table. The look-up tables perform best near the focal depth at 4.9 cm.

Table 2.1: CH4-1 simulation parameters

Transducer	CH4-1
Attenuation	0.7 dB/cm/MHz
Speed of Sound	1540 m/s
Excitation Focal Depth	4.9 cm
Excitation F/#	2.0
Receive F/#	0.5
Push Center Freq.	2.22 MHz
Track Center Freq.	3.08 MHz
Sampling Freq. (Simulation)	1 GHz
Sampling Freq. (Down-Sampled)	40 MHz
Tracking Pulse Repetition Freq. (PRF)	10 kHz

estimator or normalized cross-correlation to compute on-axis displacements described in Section 2.2. Then, we find the peak displacement at each depth. The third column of Figure 2.3 shows the peak displacement curve for a single realization for each estimator. Next, we average the time-to-peak displacement curves for 20 simulated speckle realizations for each of the stiffnesses. This gives the look-up tables shown in the last column of Figure 2.3. The shear modulus of an experimental case can be found by interpolating the look-up tables based on the time-to-peak displacement at each depth.

2.3.4 Phantom Experiment

We performed a preliminary experiment of the on-axis stiffness estimation in a tissue-mimicking phantom. We acquired 15 sets of RF data in response to an acoustic radiation force. We used a rotation platform to image 15 different speckle regions in the phantom using a CH4-1 probe. The imaging parameters are consistent with the parameters in Table 2.1 except we had a sampling frequency of 40 MHz and a tracking pulse repetition frequency (PRF) of 4.8 kHz. The ARF push had 400 cycles and a duration of 180 μs. We found on-axis displacements using the Bayesian displacement estimator and normalized cross-correlation described in Section 2.2.

Time-to-peak displacement estimates are sensitive to changes in the peak displacement. Because the peak changes as a function of motion, we need to filter out motion that is not due to the acoustic radiation force. We evaluated the performance of motion filters using linear, quadratic, and cubic fits and varied the number of displacement points used in the fit equations [75]. The quadratic filter had the lowest error in stiffness estimation results and those results are shown. The quadratic motion filter was applied to the on-axis displacement data at each depth. Figure 2.4 shows an example of a displacement curve before and after motion filtering at a single depth of 4.9 cm. To filter out the motion not due to the acoustic radiation force, we used displacement points outside of the time of the ARF motion to input into the quadratic fit equation. We used two points before the ARF push was applied

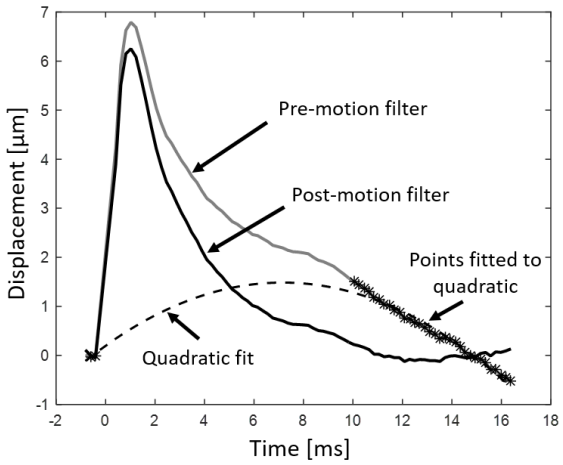

Figure 2.4: Phantom ARF displacement curves at a depth of 4.9 cm before and after a quadratic motion filter. The gray curve is the displacement before motion correction. The stars are the points used in a quadratic fit equation, including 2 points before the ARF push and all the points after most of the tissue has recovered from the displacement. The dotted line is the curve fit which we subtract from the gray displacement curve. The black line is the resulting fit after removing motion.

and all the points after most of the material recovered from displacement. The quadratic fit is shown in Figure 2.4 as the dotted curve. The pre-filtered curve is shown in gray. We subtracted the fitted dotted curve from the pre-filtered displacement curve to remove the motion which resulted in the black post-filtered curve. We performed the fitting and motion filtering at each depth.

After motion filtering, we found the time-to-peak displacement at each depth. Then, we used each look-up table to find a stiffness estimate based on time-to-peak on-axis displacement at each depth. Because we did not know the absolute stiffness of the phantoms, we computed a robust, lateral time-of-flight-based shear wave speed and converted to shear modulus [32]. The shear wave speed was measured three times for each location and we took the median estimate for each case. The error was computed between stiffness estimates using the lateral shear wave speed method and the on-axis method using the look-up table.

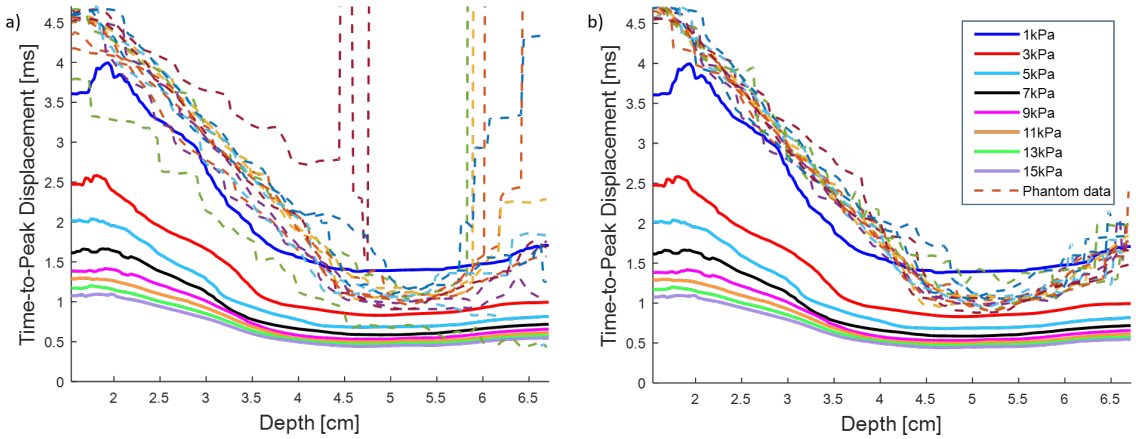

Figure 2.5: Phantom time-to-peak displacement estimates for each acquisition in one phantom (dotted lines) plotted on the Bayesian displacement-derived stiffness look-up table (solid lines) (a) before and (b) after the quadratic motion filter was applied. Using a lateral time-of-flight shear wave speed, the phantom acquisitions had a shear modulus of 2.07 +/- 0.12 kPa. After motion filtering, the phantom curves are between the 1 and 3 kPa look-up table lines at the focal depth of 4.9 cm where the method performs best.

2.3.5 Phantom Results

Figure 2.5 shows the time-to-peak displacement curves for the phantom results (a) before and (b) after applying a quadratic motion filter. The solid lines show the Bayesian displacement estimator-derived look-up table. The dotted lines are time-to-peak displacement curves for the 15 tissue-mimicking phantom cases. To find the stiffness of the phantom, we computed a shear wave speed using the lateral time-of-flight-based method. The phantom cases had a mean shear modulus of 2.07 kPa and a standard deviation of 0.12 kPa. Without motion filtering, some time-to-peak displacement curves are outside of the simulated look-up table and shear modulus estimates are unrealizable. After the motion filter, the phantom results more closely match the look-up table and generate expected shear modulus estimates especially within the depth of field of the ARF excitation.

Figure 2.6 shows the shear modulus results for the 15 tissue-mimicking phantom cases. The normalized cross-correlation stiffness results in gray are found using the normalized cross-correlation-derived look-up table and the Bayesian stiffness results in black are found

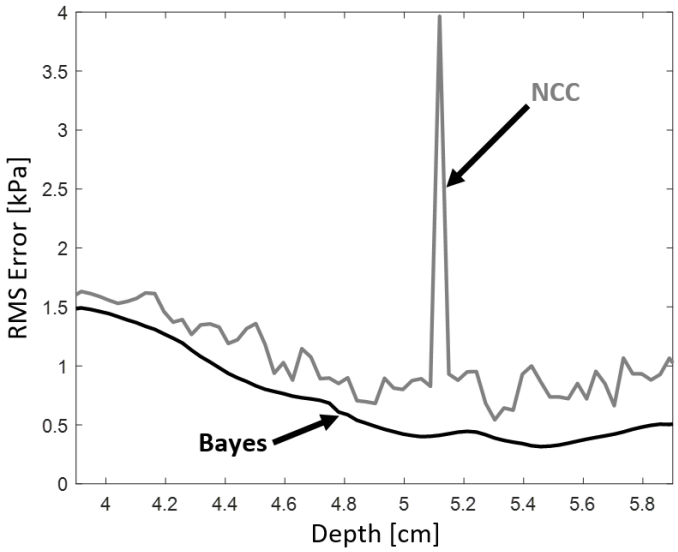

Figure 2.6: Root mean square (RMS) error of shear modulus in 15 tissue-mimicking phantoms. RMS error results using a Bayesian (Bayes) displacement estimator are shown in black and results using a normalized cross-correlation (NCC) displacement estimator are shown in gray. Bayes results have a lower RMS error at all depths within the focus' depth of field.

using the Bayesian displacement-derived look-up table. We computed the error between our results and the lateral shear wave speed-derived results. There is less variability and lower error in the Bayesian shear modulus results compared to normalized cross-correlation results.

Figure 2.7 is a Bland-Altman plot to compare the phantom shear modulus estimates using the lateral time-of-flight shear wave speed method and our on-axis method. The y-axis of the plots is the difference between the two estimates and the x-axis is the average of the two estimates. The gray lines show +/- 2 standard deviations away from the mean difference which is shown in the black line. Figure 2.7(a) shows the on-axis results using the Bayesian displacement estimator and Figure 2.7(b) shows the on-axis results using normalized cross-correlation. The Bayesian results show more agreement with the shear wave speed-derived results than normalized cross-correlation because there is a lower standard deviation in the mean difference between the estimates. We performed a t-test and found

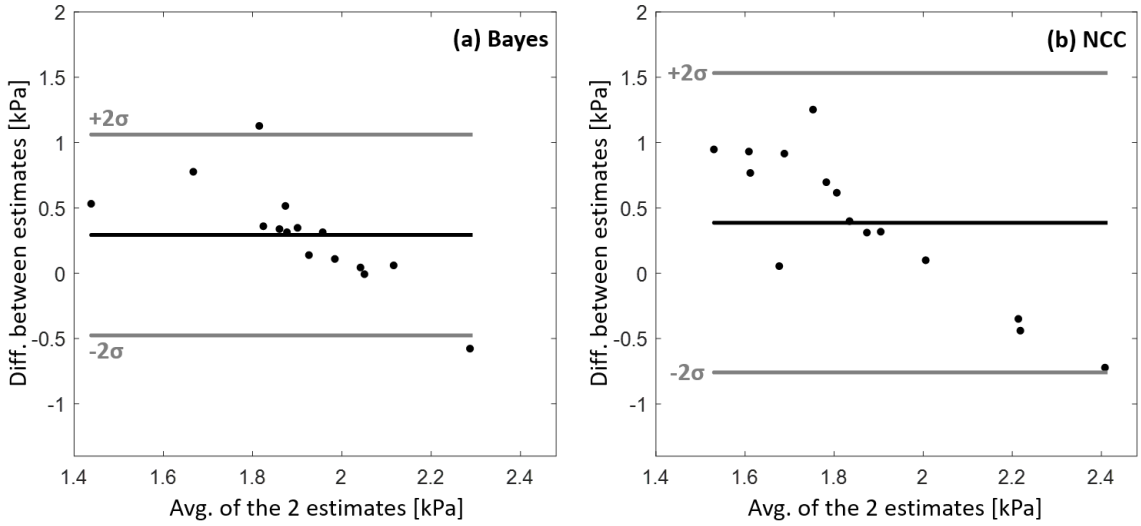

Figure 2.7: Bland-Altman plots comparing the phantom data shear modulus estimates using two methods: the on-axis method using (a) Bayesian displacement estimator or (b) normalized cross-correlation compared to the lateral shear wave speed-derived stiffness estimate. The y-axis is the difference in shear moduli between the two methods (on axis or lateral shear wave speed-derived estimate) and the x-axis is the average of the two estimates. The gray lines show +/- 2 standard deviations from the mean difference shown as the black line. On-axis Bayesian results agree more closely to shear wave speed-derived results. A t-test showed no significant bias in the means at a 5% significance level.

there was not a significant bias in the means at a 5% significance level. These phantom results show that on-axis methods coupled with a Bayesian displacement estimator produce stiffness estimates comparable to laterally offset shear wave methods [34].

2.3.6 Discussion and Conclusion

We have presented an acoustic radiation force-based method of quantifying shear modulus at the region of excitation. These preliminary results show that an advanced displacement estimator is needed to measure displacements on-axis of the acoustic radiation force push to generate stiffness estimates comparable to shear wave speed-derived stiffness estimates. It shows we can apply a simulated look-up table to real experimental phantom data. The method performs best within the focus' depth of field. The motion filtering also improves accuracy in the phantom data at the focus' depth of field as shown in Figure 2.5(b).

However, there could be some bias or simulation mismatch affecting the near-field time-to-peak displacements. The next chapter will discuss changes in attenuation or sound speed that could contribute to model mismatch.

Like SWEI, the error of our measurements increases when the tissue is stiffer due to higher variance in displacement estimates and the declining ability to track faster propagation of displacements. The stiffness estimation quality depends on how accurately we capture the on-axis displacement profile and the location of the maximum displacement. We may be able to improve estimating stiffer tissues by increasing the tracking pulse repetition frequency (PRF) to capture faster time-to-peak displacements with more sampling. This study used a PRF of 4.8 kHz and demonstrated initial feasbility in relatively soft phantoms (shear modulus of $\sim$2 kPa). We tested this same imaging sequence to measure stiffer phantoms, but the peak displacements occurred faster and were difficult to capture with this PRF. The next chapters will further study the on-axis stiffness estimation method in simulations and in phantoms of different elasticities while imaging with a higher PRF.

Chapter 3

On-Axis Acoustic Radiation Force-based Elasticity in Homogeneous Simulations

This work is currently in review for publication in Ultrasonic Imaging: Walsh, Kristy, et al. "On-Axis Acoustic Radiation Force-based Quantitative Elasticity using a Bayesian Displacement Estimator " *Ultrasonic Imaging*.

3.1 Introduction

The preliminary studies in Chapter 2 show initial feasibility of the on-axis elasticity method in soft homogeneous phantoms. The Bayesian displacement estimator also improves displacement estimates which leads to more accurate elasticity estimates. To evaluate the performance of the on-axis elasticity method in different tissue types, we perform a series of simulation studies. Many tissues can slightly vary from our assumptions of a constant sound speed and attenuation. This becomes especially important clinically when imaging tissues to detect diseases. Diseases can physiologically change tissue structures which results in a change of sound speed. For example, this is prevalent in the liver where fatty liver disease tends to lower sound speed, and livers with fibrosis and cirrhosis tend to have higher sound speeds [76, 77]. Livers with fatty liver disease have also been shown to have higher attenuations [78]. We have to model these parameters in our finite element simulations to make the elasticity look-up table. Therefore, choosing realistic parameters is important for this method.

Most imaging parameters in this chapter are similar to the settings in Section 2.3.2. However, we chose a different transducer which we can implement on our Verasonics Vantage System (Verasonics, Inc., Kirkland, WA) which we do in the following chapter. We also use a higher pulse repetition frequency to capture faster time-to-peak displacements.

The methods in this chapter describe the simulations used to make a look-up table to derive stiffness estimates. We test the on-axis stiffness estimation approach in simulations. We compare the performance of the Bayesian displacement estimator to the commonly used displacement estimator, normalized cross-correlation. We also test the performance of the on-axis method during changes of attenuation, signal-to-noise ratio, and sound speed.

3.2 Methods

3.2.1 Overview

Simulated data were used to make look-up tables to estimate stiffness using time-to-peak displacement as a function of depth for a known excitation configuration because stiffness changes the time-to-peak displacement behavior. Figure 3.1 shows the steps used to generate a stiffness look-up table from simulated ARF displacement data. We created two look-up tables using either the Bayesian displacement estimator or normalized cross-correlation. We can use the look-up table to extract stiffness information given a time-to-peak displacement value at a certain depth.

3.2.2 Finite Element Simulations

Finite element responses to acoustic radiation force were simulated to generate a stiffness look-up table. The simulations mimic the response of tissues of varying stiffness to a certain transducer ARF excitation push and tracking configuration. We simulated a range of stiffnesses in shear moduli from 0.33-15 kPa. Tissue properties were simulated using a 3,660,000 element, 3D mesh extending 6.1 cm axially, 2.0 cm laterally, and 0.3 cm in elevation. The material was modeled as linearly elastic, homogeneous, and isotropic with a constant density of 1.0 g/cm^3 and a Poisson's ratio of 0.495. Field II was used to calculate the pressure field of the experimental transducer configuration and the parameters are shown in Table 3.1 [73]. LS-DYNA (Livermore Software Technology Corporation, Liv-

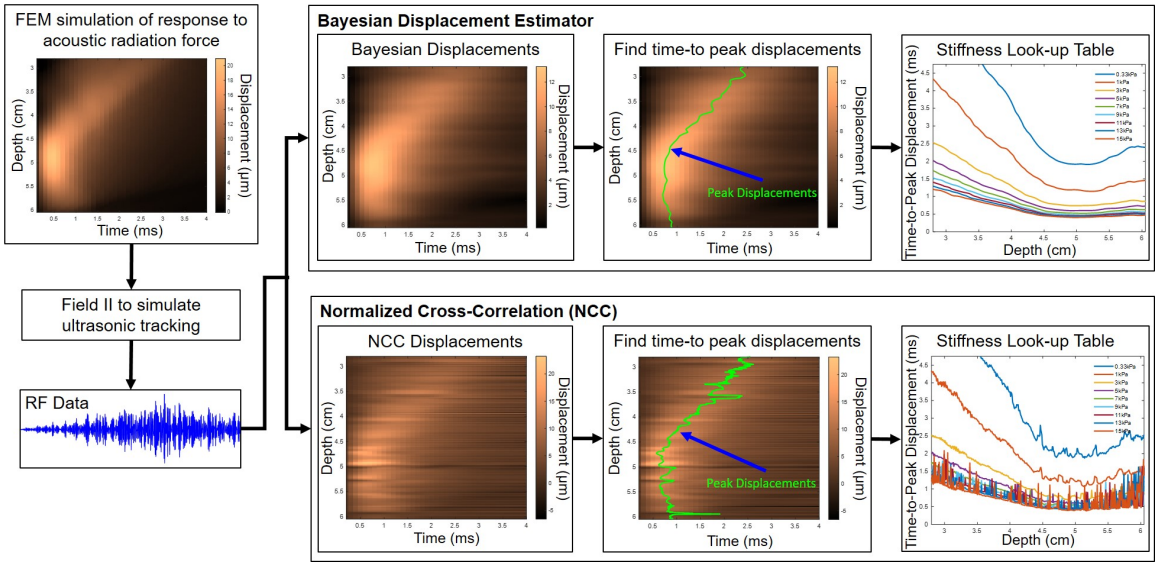

Figure 3.1: Overview of the generation of stiffness look-up tables. The first column shows on-axis displacements of an FEM simulation response to ARF. Then, we track the displacements using Field II to get on-axis RF data. We use either the Bayesian displacement estimator or normalized cross-correlation (NCC) to estimate the displacements. Next, we find peak displacement at each depth to get a time-to-peak displacement curve (shown in green). We simulate 20 realizations for each stiffness (shear modulus of 0.33-15 kPa) and average the time-to-peak displacement curves to generate the stiffness look-up table. The look-up tables perform best near the focal depth at 4.98 cm.

ermore, CA) was used to simulate the displacements induced by the ARF push [19]. An example of the FEM simulated displacements before tracking are shown in the left column of Figure 3.1. The 3D volume of displacements was imported into Field II to displace the point scatterers. The density of scatterers was 50,000 scatterers/cm^3 and over 15 scatterers per resolution cell to ensure fully developed speckle. We also used Field II to simulate on-axis ultrasonic tracking using the C5-2 probe configuration [74]. The simulated RF data were filtered using a 4^{th}-order, high-pass Butterworth filter with a cutoff frequency of 2.5 kHz to account for a simulation artifact.

3.2.3 Stiffness Look-up Table

The stiffness look-up table is based on the time-to-peak displacement at each depth for a range of stiffnesses. To generate the look-up table, we simulated 20 independent speckle

Table 3.1: C5-2 simulation parameters

Option	Parameter Value
Transducer	C5-2
Attenuation	0.7 dB/cm/MHz
Speed of Sound	1540 m/s
Push Center Freq.	2.3585 MHz
Excitation F/#	1.5
Excitation Focal Depth	4.98 cm
Push Duration	128 μs
Tracking Center Freq. (f_c)	3.125 MHz
Tracking Pulse Repetition Freq. (PRF)	10 kHz
Receive F/#	0.5
Sampling Freq. (Field-II Simulation)	160 MHz
Sampling Freq. (RF Down-Sampled)	40 MHz
Sampling Freq. f_s (Disp. Est.)	120 MHz
NCC Kernel Length	$3f_s/f_c$
Bayesian Likelihood Kernel Length	$3f_s/f_c$

realizations of each stiffness for shear moduli of 0.33, 1, 3, 5, 7, 9, 11, 13, and 15 kPa using the method described in Section 3.2.2 and the parameters in Table 3.1. Often, a lower push frequency is used to broaden the push beam width compared to the track beam width to reduce effects of speckle shearing that lead to underestimation of the tracked tissue displacement [74, 79]. After simulating ultrasonic tracking using Field II to get received RF data, we use either the Bayesian displacement estimator or normalized cross-correlation to compute on-axis displacements described in Section 2.2. In both the Bayesian displacement estimator and normalized cross-correlation, we used a progressive reference so that the displacement was computed between each consecutive RF line. Then, we find the peak displacement at each depth. The third column of Figure 3.1 shows the peak displacement curve for a single realization for each estimator. Next, we average the time-to-peak displacement curves for 20 simulated speckle realizations for each of the nine stiffnesses. This gives the look-up tables shown in the last column of Figure 3.1. Figure 3.2 shows both the Bayesian displacement-derived and normalized cross-correlation-derived stiffness look-up tables on the same plot to show comparison between the displacement estimators.

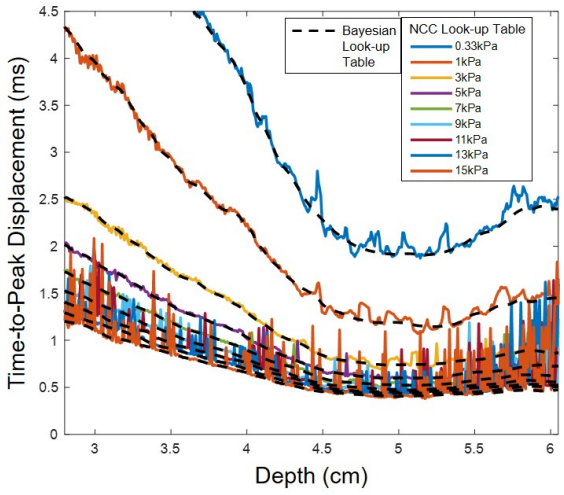

Figure 3.2: Comparison of stiffness look-up tables. The normalized cross-correlation (NCC) look-up table is shown by the solid colored lines and the Bayesian displacement estimator look-up table is plotted over each stiffness curve in black dotted lines. The Bayesian displacement estimated look-up table has less variance in time-to-peak displacement curves compared to the normalized cross-correlation look-up table.

The shear modulus of an experimental case can be found by interpolating the look-up tables based on the time-to-peak displacement at each depth.

3.2.4 Simulation Experiments

The simulation experiments used the method described in Section 3.2.2 and the parameters in Table 3.1. We simulated 20 independent realizations of a linearly elastic, homogeneous, and isotropic medium with a shear modulus of 2 kPa. We applied both the Bayesian displacement estimator and normalized cross-correlation to each realization. We found time-to-peak displacement at each depth and used the corresponding look-up table (Bayesian or normalized cross-correlation) to extract a stiffness estimate. The error was calculated based on the known shear moduli of the simulations.

3.2.5 Attenuation Mismatch Analysis

An assumption of the look-up table is that the tissue attenuation is constant at 0.7 dB/cm/MHz. To test the performance of our method in the presence of attenuation changes in tissues, we simulated media with attenuations different from the simulated look-up table attenuation. We used the look-up table derived from simulations with parameters shown in Table 3.1 that had an attenuation of 0.7 dB/cm/MHz. The experimental simulations had attenuations of 0.5, 0.7, and 0.9 dB/cm/MHz. These cases used the Bayesian displacement estimator and the Bayesian displacement estimator-derived look-up table to get shear modulus estimates.

3.2.6 Signal-to-Noise Ratio Analysis

To test the performance of the on-axis method at different signal-to-noise ratios (SNRs), we varied the noise level in the RF data of our simulations. Along with the simulations at 2 kPa, we also studied the performance of two stiffer experimental simulations at shear moduli of 6 and 10 kPa. We added white Gaussian noise to our experimentally simulated RF data before calculating the displacements using the Bayesian displacement method. We varied the SNR to 0, 10, 20, 30, 40, and 50 dB by adding the respective amount of noise based on the signal power to reach the desired SNR. We used the Bayesian displacement estimator and the Bayesian displacement estimator-derived look-up table to get shear modulus estimates. A shear modulus estimate is found for each case by taking the mean shear modulus in the focus' depth of field. The root mean square (RMS) error is found based on the known shear modulus (2, 6, or 10 kPa) of the simulations and is computed over the 20 realizations for each stiffness and SNR.

3.2.7 Sound Speed Error Analysis

We varied the sound speed in our experimental simulations to show the performance of the on-axis stiffness estimation when the tissue has different sound speeds as compared to the look-up table. Many tissues can slightly vary from our assumption of a constant sound speed of 1540 m/s. This becomes especially important clinically when imaging tissues to detect diseases. Diseases can physiologically change tissue structures which results in a change of sound speed. This is prevalent in the liver where fatty liver disease tends to lower sound speed, and livers with fibrosis and cirrhosis tend to have higher sound speeds [76, 77]. In this study, we changed the sound speed in the experimental simulations while assuming the sound speed was constant at 1540 m/s. This created errors in our FEM simulations and the transmit and receive focusing delays during pushing and tracking. We set the sound speeds between -10% and +10% error of the assumed sound speed of 1540 m/s. We used the Bayesian displacement estimator and the Bayesian displacement estimator-derived look-up table to get shear modulus estimates. A shear modulus estimate is found for each case by taking the mean shear modulus in the focus' depth of field. The RMS error is found based on the known shear modulus of 2 kPa for these simulations and is computed over the 20 simulations for each sound speed error.

3.3 Simulation Results

Figure 3.3 shows the shear modulus results for 20 simulated experimental realizations at a shear modulus of 2 kPa. Figure 3.3 is plotting the root mean square (RMS) error of the shear modulus. The reference value used to compute the error was the shear modulus value of the FEM simulations. The normalized cross-correlation stiffness results are found using the normalized cross-correlation-derived look-up table, whereas the Bayesian stiffness results are found using the Bayesian displacement-derived look-up table. The normalized cross-correlation RMS error shown in red is higher at nearly all depths as compared to the

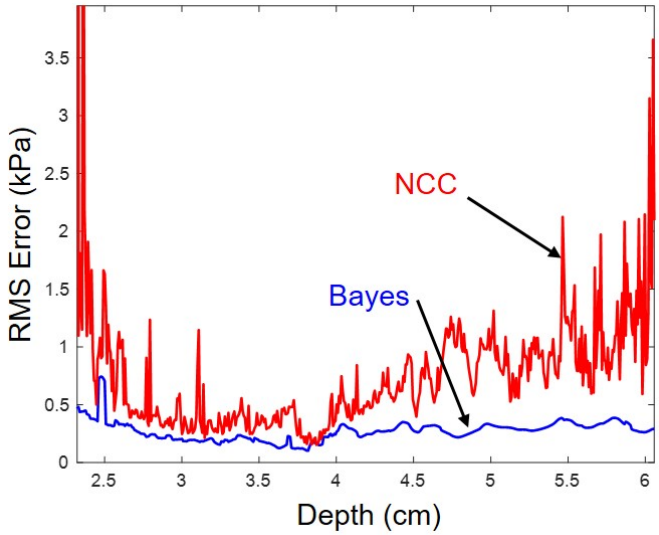

Figure 3.3: Root mean square (RMS) error of shear modulus of 20 simulated stiffnesses at a shear modulus of 2 kPa. RMS error results using a Bayesian (Bayes) displacement estimator are shown in blue and results using a common motion estimator, normalized cross-correlation (NCC), are shown in red. Bayesian results have a lower RMS error at almost all depths.

Bayesian results shown in blue. There is also higher variability in the normalized cross-correlation results as compared to the Bayesian results. The simulations had a RMS error between 0.22-0.39 kPa using the Bayesian displacement estimator and 0.40-2.1 kPa using normalized cross-correlation 1cm around the focal depth. The average percent bias around the focal depth was -11% and -54% for the Bayesian displacement estimator and normalized cross-correlation, respectively.

Figure 3.4 shows the results of the attenuation mismatch study using a Bayesian displacement estimator. All shear modulus estimates are found from a look-up table using simulations with an attenuation of 0.7 dB/cm/MHz. Figure 3.4 shows the RMS error in shear modulus for simulations at 0.5, 0.7, and 0.9 dB/cm/MHz attenuations. The 0.7 dB/cm/MHz attenuation simulations are the same results shown in Figure 3.3. Figure 3.4 shows that attenuation mismatches between the look-up table simulations and experimental cases can create errors in the stiffness results. Changing the attenuation to 0.5 or 0.9 dB/cm/MHz results in an increase in RMS error in shear modulus estimates, but the error is lower closer

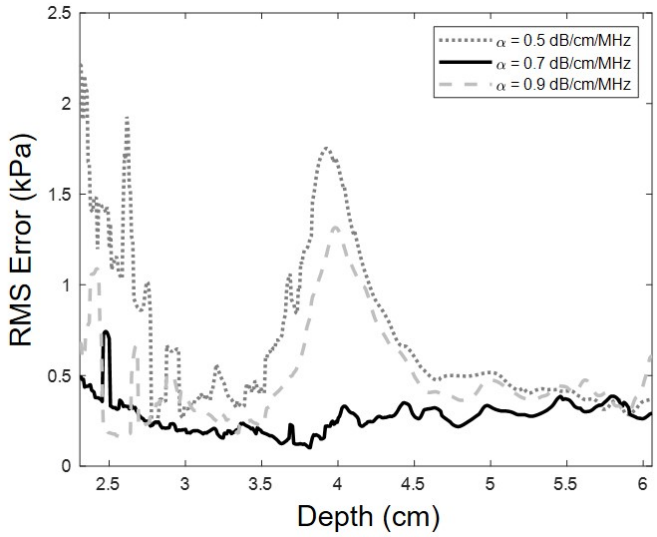

Figure 3.4: Root mean square (RMS) error of shear modulus of 20 simulated stiffnesses at a shear modulus of 2 kPa for each attenuation. The simulations had attenuations, α, of 0.5, 0.7, and 0.9 dB/cm/MHz and all used a look-up table simulated at an attenuation of 0.7 dB/cm/MHz.

to the focus and at deeper depths. For our phantom experiments in the following chapter, we use the data near the focal depth between 4.5 and 5.5 cm to compute a stiffness estimate using the look-up table.

Figure 3.5 shows the RMS error in shear modulus for the on-axis method using the Bayesian displacement estimator under different levels of signal-to-noise. At very low levels of SNR, the shear modulus estimate is unreliable. As the SNR increases, the RMS error approaches the RMS error of our noise-free simulation results. The percent error in each phantom is consistent, especially at higher levels of SNR. There is higher error in stiffer media due to the higher velocities and the nature of the look-up table; however, this could be improved by increasing the PRF in tracking.

Figure 3.6 shows the RMS error in shear modulus for the on-axis method using the Bayesian displacement estimator when there are sound speed errors. We introduced errors from -10% to +10% of 1540 m/s. As the sound speed of the simulations gets further away from 1540 m/s, there is an increase in stiffness estimate error. The lowest error occurs at

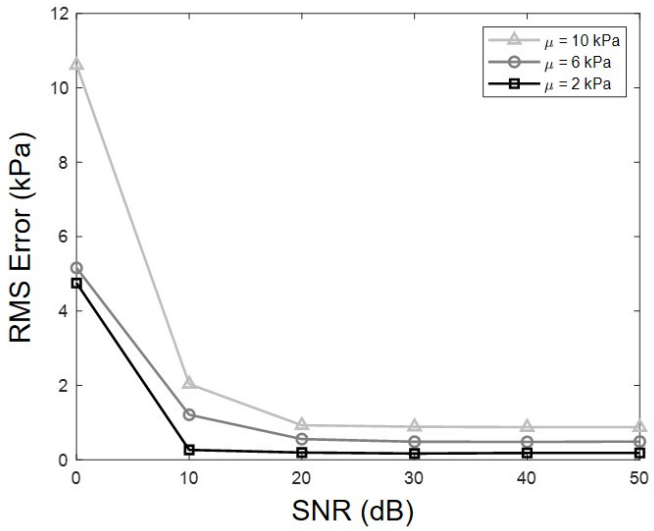

Figure 3.5: Root mean square (RMS) error of shear modulus of 20 simulated stiffnesses at shear moduli of 2, 6, and 10 kPa for each signal-to-noise ratio (SNR). Each stiffness estimate was found by taking the mean shear modulus in the focus' depth of field. The best performance is at or above an SNR of 20 dB.

the sound speed of 1540 m/s. Between sound speeds of 1501.5-1578.5 m/s, the error is less than 16.5%.

3.4 Discussion and Conclusion

Assumptions about the tissue being interrogated need to be considered when generating the stiffness look-up table. In our simulation results and analyses, we show that the quality of this method can depend on signal-to-noise ratio of the RF data. Our best performance occurs at SNRs at or above 20 dB (Figure 3.5). Assumptions about the tissue properties, such as attenuation coefficient and sound speed, can cause errors in the look-up table and affect the estimation performance (Figures 3.4 and 3.6). Also, physiological changes in tissue, such as disease progression, can cause changes in tissue mechanical properties. A major application of SWEI is staging liver fibrosis. The tissues in different stages of this disease can exhibit a change in sound speed and attenuation [76, 77, 78]. These assumptions about the tissue properties suggest the need to add additional dimensions to the look-up table to

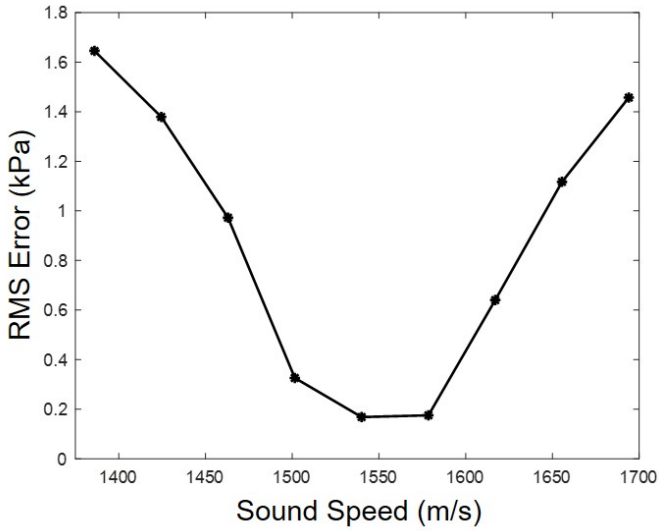

Figure 3.6: Root mean square (RMS) error of shear modulus of 20 simulated stiffnesses at a shear modulus of 2 kPa for each sound speed error from -10% to +10% of 1540 m/s. Each stiffness estimate was found by taking the mean shear modulus in the focus' depth of field. As sound speed of the simulations deviates further away from the assumed 1540 m/s, we see an increase in estimation error.

account for attenuation, sound speed, and perhaps viscosity in these applications.

We tested the on-axis elasticity estimation approach in simulations. We compared the performance of the Bayesian displacement estimator to the commonly used displacement estimator, normalized cross-correlation. We also tested the performance of the on-axis method during changes of attenuation, signal-to-noise ratio, and sound speed. The simulation results provide insight into the importance of an advanced displacement estimator and selection of realistic parameters for the simulation model, such as sound speed and attenuation. We have also shown the performance of the on-axis elasticity method in different simulated elasticities and signal-to-noise ratios.

Chapter 4

On-Axis Acoustic Radiation Force-based Elasticity in Homogeneous Phantoms

This work is currently in review for publication in Ultrasonic Imaging: Walsh, Kristy, et al. "On-Axis Acoustic Radiation Force-based Quantitative Elasticity using a Bayesian Displacement Estimator " *Ultrasonic Imaging*.

4.1 Introduction

Quantifying tissue stiffness is clinically useful in staging or monitoring many diseases and their treatments. Manual palpation can be the first indicator of a disease that causes changes in the mechanical properties of tissues, but it can be relatively subjective. Acoustic radiation force (ARF)-based elasticity imaging can provide stiffness information that is less operator dependent and at deeper, inaccessible depths [13, 5]. Elasticity imaging methods have been successful in detecting diseased tissue where mechanical changes can be an indication of the severity. ARF-based techniques are used for abdominal imaging [80], cardiac imaging [81], biopsy guidance in prostate, lymph node, and breast exams [82, 83], monitoring radiofrequency (RF) ablations in the liver and cardiovascular tissues [27, 28], and characterizing atherosclerosis [29, 30]. Elasticity imaging is useful in clinical ultrasound, especially when it can provide quantitative stiffness measurements. For example, shear wave speed can be used as a quantitative imaging biomarker for staging liver fibrosis [36, 37, 84].

As discussed in Section 1.2.4, shear wave elasticity imaging (SWEI) is a quantitative ARF-based technique that can estimate tissue elastic properties using a mechanical model. In traditional SWEI, shear waves are generated within tissue by the acoustic radiation force of a focused ultrasound beam [15]. Acoustic radiation force is created when an acoustic

wave transfers momentum into the propagation medium by absorption and/or reflection [17]. In soft tissues where the majority of attenuation is caused by absorption [18], the acoustic radiation force magnitude, $\vec{F}$ [kg/(cm^{2}s^2)], can be described as,

$$\vec{F} = \frac{2\alpha\vec{I}}{c}, \tag{4.1}$$

where $\vec{I}$ [W/cm^2] is the time-average intensity at a given spatial location, α [dB/cm/MHz] is the attenuation coefficient, and c [cm/s] is the speed of sound [17, 19]. This acoustic radiation force excitation induces displacements in the direction of the longitudinal wave propagation within the focal region of the acoustic beam. These excitations create mechanical transverse waves called shear waves that propagate laterally away from the region of excitation. The shear waves are a finite train of equivoluminal waves that displace particles in the axial direction and propagate laterally or perpendicular to the displacement [6]. The shear wave speed provides information about the tissue that was displaced at the focal region. Assuming the tissue is linearly elastic and isotropic, the shear wave speed, c_T, can be related to the tissue's shear modulus, μ, by

$$c_T = \sqrt{\frac{\mu}{\rho}}, \tag{4.2}$$

assuming a constant density, ρ [6]. Common methods to reconstruct shear modulus use Equation 4.2 to convert the shear wave speed to shear modulus [31, 16]. In these shear wave elasticity methods, the shear wave is observed as a displacement at a lateral location outside the region of excitation. To estimate the shear wave speed, time-of-flight-based methods often track the shear wave displacement and find the velocity based on its spatial and temporal locations [32, 33].

In this work, we only measure on-axis displacement and quantify stiffness by using a look-up table based on simulations to reconstruct shear modulus. Like SWEI, we use an acoustic radiation force to induce displacement; however, we only measure displacement

along the axis of excitation. After the ARF excitation is applied, the focal region reaches a maximum displacement that decays in magnitude as the shear waves propagate laterally away from the region of excitation. We measure the on-axis displacement through time and find the time-to-peak displacement. The time-to-peak displacement depends on depth and the spatial distribution of the excitation. Because we are not measuring the shear wave propagation, we cannot use Equation 4.2 to relate the shear wave speed to shear modulus. Instead, we find the time of peak on-axis displacement and use a lookup table with time-to-peak displacement as a function of depth for a certain excitation pulse and displacement sensing sequence [66]. Using a look-up table avoids assumptions limited by the analytical Gaussian solution [15, 16]. Measuring only on-axis displacements can simplify hardware required for a stiffness estimate. However, the challenge with measuring displacements at the region of excitation is the large variance in displacement estimates [66]. Consequently, this technique had a substantially higher variance in shear modulus estimates than traditional lateral shear wave speed-derived estimates [66]. To improve this, we apply an advanced displacement estimation technique using a Bayesian displacement estimator, that has been shown to reduce displacement estimation variance [25, 26, 72, 65, 85].

The methods in this chapter use the same simulated look-up table as described in Chapter 3. We create on-axis acoustic radiation force imaging sequences on a programmable research scanner, Verasonics Vantage 128 System (Verasonics Inc., Kirkland, WA), and describe our gelatin phantom making procedure. We test the on-axis stiffness estimation approach in four tissue-mimicking gelatin phantoms of different elasticity. We compare the performance of the Bayesian displacement estimator to the commonly used displacement estimator, normalized cross-correlation. We also compute a lateral time-of-flight-based shear wave speed and convert to shear modulus to compare on-axis to lateral shear modulus estimates [32, 79].

4.2 Methods

4.2.1 Gelatin Phantom Construction

We tested our on-axis stiffness estimation method in four tissue-mimicking phantoms made of different concentrations of gelatin to vary the stiffness [86, 87, 88]. We mixed gelatin powder (Gelatin from porcine skin, 300 Bloom strength, Sigma-Aldrich, St. Louis, MO) with degassed, deionized water and isopropyl alcohol to increase the sound speed. We stirred and heated the solution until the gelatin powder was dissolved and the solution turned clear. We also degassed the solution to further remove air bubbles. While it was still in liquid form, we stirred in 6% concentration by weight of graphite (General Pencil Company, Inc., Jersey City, NJ) for scattering properties. The solution was poured into phantom molds, securely sealed, and slowly rotated for about four hours until it cooled and congealed. We rotated the phantoms so that the graphite did not settle to bottom while congealing. The gels were then refrigerated overnight. By increasing the gelatin concentration, it increases the stiffness. We created phantoms with 2, 3, 4, and 5% gelatin concentrations.

4.2.2 Acquisition Sequences

In each gelatin phantom, we imaged 15 sets of acquisitions using the Verasonics Vantage 128 System (Verasonics Inc., Kirkland, WA) and a C5-2 curvilinear transducer. We rotated the phantoms to image 15 different speckle regions in each. At each location, we ran two imaging sequences to acquire on-axis data as well as a shear wave speed. The shear wave speed sequence is described by Deng et al. (2017) for the C5-2 transducer and posted on a Github repository [79]. The on-axis imaging sequence parameters were consistent with the look-up table's simulation parameters described in Chapter 3 and shown in Table 3.1 except we used an axial sampling frequency of 12.5 MHz. The phantom imaging parameters are shown in Table 4.1 using a C5-2 curvilinear array and a focused push and focused tracking sequence.

Table 4.1: C5-2 gelatin phantom imaging parameters

Option	Parameter Value
Transducer	C5-2
Push Center Freq.	2.3585 MHz
Excitation F/#	1.5
Excitation Focal Depth	4.98 cm
Push Duration	128 μs
Tracking Center Freq. (f_c)	3.125 MHz
Tracking Pulse Repetition Freq. (PRF)	10 kHz
Receive F/#	0.5
Sampling Freq. (Acquired)	12.5 MHz
Sampling Freq. (Up-Sampled)	37.5 MHz
Sampling Freq. (f_s) (Disp. Est.)	112.5 MHz
NCC Kernel Length	$3f_s/f_c$
Bayesian Likelihood Kernel Length	$3f_s/f_c$

4.2.3 Post-Processing

4.2.3.1 Displacement Estimation

We found on-axis displacements using the Bayesian displacement estimator and normalized cross-correlation as described in Section 2.2. We also upsampled the acquired RF data by a factor of three from 12.5 MHz to 37.5 MHz. Due to discrete sampling of signals in time, the true maximum of the normalized cross-correlation function may be between samples. Upsampling and interpolation techniques are used to improve accuracy of sub-sample estimates by reducing false peak errors and aliasing. We further upsampled the RF data by another factor of three for both displacement estimators using cubic splines [21]. The normalized cross-correlation and Bayesian likelihood kernel lengths in samples are described in Table 4.1 in terms of the sampling frequency, f_s, and tracking center frequency, f_c, which are approximately 0.76 mm. Kernel lengths of 3λ are typically used in small deformation elastography to preserve the accuracy in the average displacement over the kernel length and also still be able to resolve changes in displacement [21]. To find the peak of the normalized cross-correlation function in Equation 2.6, we also performed

a parabolic fit of the peak to get subsample displacement estimates [71]. In the Bayesian displacement estimator, we used a neighborhood, B, of 3, which includes the two adjacent axial kernels on either side of the current estimate, with a uniform weighting, w_j, of 0.5. We also used a p of 2 for a Gaussian shaped prior. In both the Bayesian displacement estimator and normalized cross-correlation, we used a progressive reference so that the displacement was computed between each consecutive RF line.

4.2.3.2 Motion Filtering

Time-to-peak displacement estimates are sensitive to changes in the peak displacement. Because the peak changes as a function of motion, we filtered out motion that is not due to the acoustic radiation force. We evaluated the performance of motion filters using linear, quadratic, and cubic fits and varied the number of displacement points used in the fit equations [75]. A quadratic filter is commonly used for removing physiological motion and also has been helpful to reduce non-ARF-induced motion in phantoms [75]. The quadratic filter performed the best and we used those results for this work. The quadratic motion filter was applied to the on-axis displacement data at each depth. Figure 4.1 shows an example of a displacement curve before and after motion filtering at a single depth of 4.98 cm. To filter out the motion not due to the acoustic radiation force, we used displacement points outside of the time of the ARF-induced motion to input into the quadratic fit equation. We used one point before the ARF push was applied (0 ms) and all the points after most of the material recovered from displacement (4.8 to 7.8 ms). The quadratic fit is shown in Figure 4.1 as the dotted curve. The pre-filtered curve is shown in gray. We subtracted the fitted dotted curve from the pre-filtered displacement curve to remove the motion which resulted in the black post-filtered curve. We performed the fitting and motion filtering at each depth.

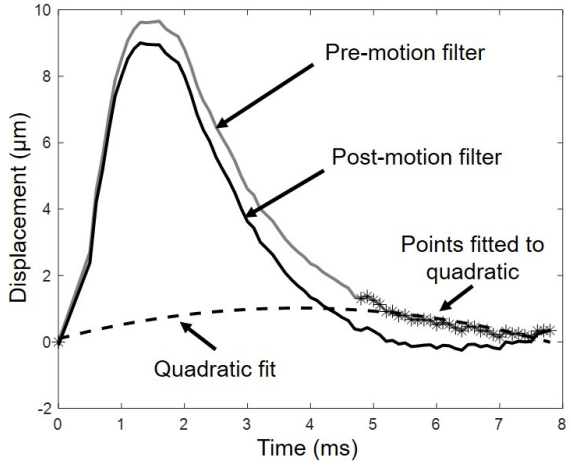

Figure 4.1: Phantom ARF displacement curves at a depth of 4.98 cm before and after a quadratic motion filter. The gray curve is the displacement before motion correction. The stars are the points fit to a quadratic equation, including one point before the ARF push and all the points after most of the tissue has recovered from the displacement. The dotted line is the curve fit which we subtract from the gray displacement curve. The black line is the resulting fit after removing motion.

4.2.3.3 Stiffness Estimation

After motion filtering, we found the time-to-peak displacement at each depth by performing a quadratic subsample peak estimation to find the time of maximum displacements. Then, we used each look-up table to find a stiffness estimate based on time-to-peak on-axis displacement at each depth. We also computed a robust, lateral time-of-flight-based shear wave speed and converted to shear modulus [32, 79]. The error was computed between stiffness estimates using the lateral shear wave speed method and the on-axis method using the look-up table.

4.3 Homogeneous Phantom Results

Figure 4.2 shows an example of a 2% gelatin phantom result. The top row (a-c) shows the results using a Bayesian displacement estimator and the bottom row (d-f) shows the normalized cross-correlation results for the same acquisition. Subplots a) and d) show the on-axis displacements after motion filtering with the peak displacements at each depth in

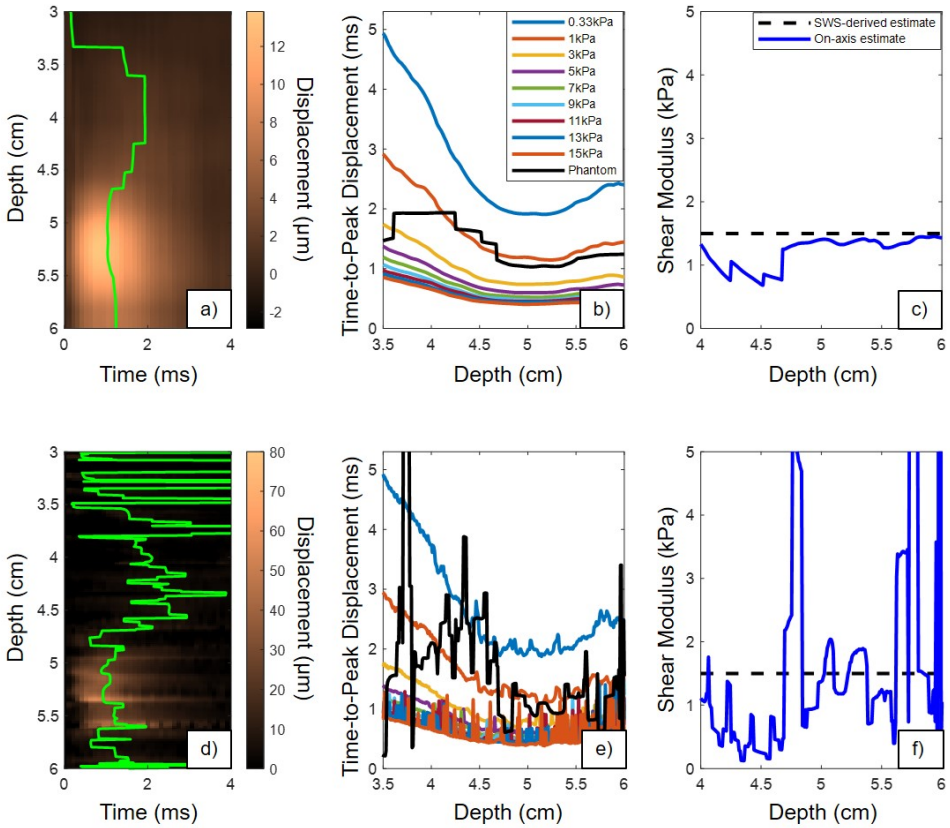

Figure 4.2: 2% gelatin phantom results using the Bayesian displacement estimator on the top row (a-c) and normalized cross-correlation on the bottom row (d-f). (a, d) On-axis displacements with the time-to-peak displacement in green. (b, e) Time-to-peak displacement curves for each phantom result (black) plotted on each look-up table. (c, f) Shear modulus results using the lateral time-of-flight based method as the gold standard (black dashed line) and the on-axis estimates (blue). The Bayesian displacement can produce a more accurate stiffness estimate than normalized cross-correlation by reducing error and variance in the on-axis displacement estimates.

green. Subplots b) and e) show each look-up table in the colored lines and the black lines show the time-to-peak displacements of the phantom. Subplots c) and f) show each shear modulus result. To find the stiffness of the phantoms, we computed a shear wave speed using the lateral time-of-flight-based method. This phantom case had a shear modulus of 1.5 kPa shown in the black dotted line. The Bayesian displacement estimator reduces the error and variance in the displacement estimates which results in a more accurate shear modulus estimate.

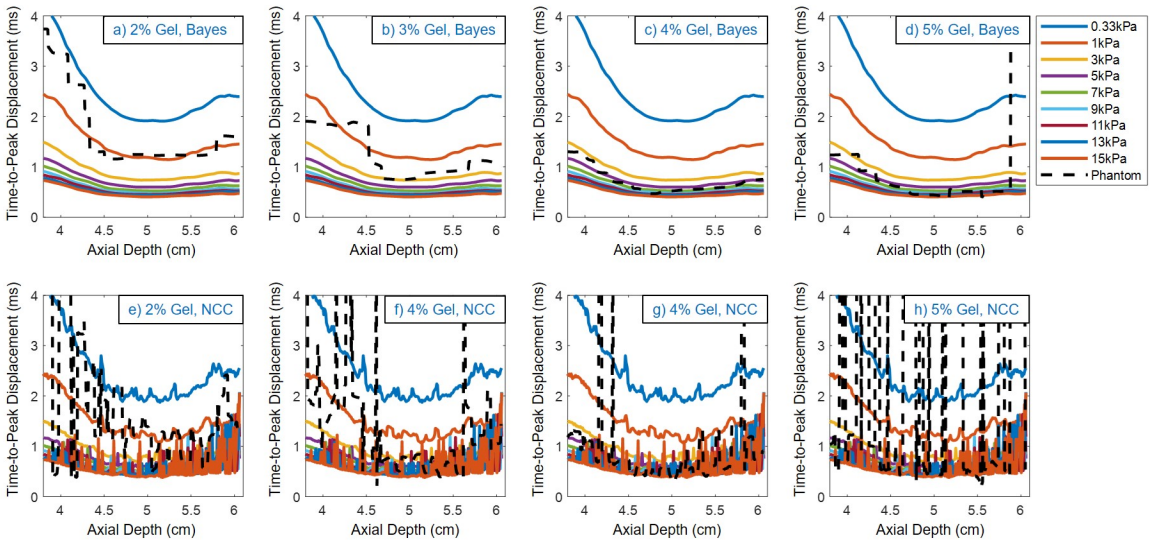

Figure 4.3: Phantom time-to-peak displacement curves (dotted lines) plotted on the Bayesian (Bayes) displacement-derived stiffness look-up table (top row, a-d) and the normalized cross-correlation (NCC)-derived look-up table (bottom row, e-h). Each subplot shows one acquisition from each phantom (2, 3, 4, 5% gelatin) with the same acquisition in each column to compare each displacement estimator.

Figure 4.3 shows the time-to-peak displacement curves for one acquisition from each gelatin phantom using either the Bayesian displacement estimator (top row) or normalized cross-correlation (bottom row) to estimate displacements in the phantoms and the corresponding look-up tables. In the stiffer phantoms with higher concentrations of gelatin, the time-to-peak displacement occurs faster as shown in the black dotted lines. The shear wave speed-derived shear moduli for these acquisitions were 1.5, 3.2, 7.5, and 11 kPa for the 2, 3, 4, and 5% gelatin phantoms, respectively. The stiffest phantom with 5% gelatin may be approaching the limit of how stiff this acquisition set-up can estimate stiffness.

Figure 4.4 is a Bland-Altman plot to compare the phantom shear modulus estimates using the lateral time-of-flight shear wave speed method and our on-axis method. Each acquisition was paired to its subsequent shear wave speed-derived estimate at the same location in the phantom. The y-axis of the Bland-Altman plots is the difference between the two estimates and the x-axis is the average of the two estimates. The red lines show +/- 2 standard deviations away from the mean difference which is shown in the black line.

Table 4.2: Phantom shear wave speed-derived shear moduli

	Mean (kPa)	St. Deviation (kPa)
2% Gelatin	1.5	0.05
3% Gelatin	3.0	0.15
4% Gelatin	7.4	0.39
5% Gelatin	12.3	1.7

The left column shows the normalized cross-correlation results and the right column shows the Bayesian displacement estimator results. The x and y axis ranges were kept constant in each row to compare the bias and performance of each displacement estimator in each phantom. In the softest phantom, the Bayesian displacement estimator had lower error and less variance in the mean difference between the estimates, but slightly more bias than normalized cross-correlation. In the three stiffer phantoms, the Bayesian displacement estimator had lower error and was less biased in the shear modulus estimates than normalized cross-correlation. Table 4.2 shows the shear wave speed-derived shear moduli for each phantom which was used as the gold standard. Table 4.3 shows the on-axis shear modulus estimates and error statistics for each phantom. The Bayesian displacement estimator results show more agreement with the shear wave speed-derived results than normalized cross-correlation. These phantom results show that on-axis methods coupled with a Bayesian displacement estimator can produce stiffness estimates comparable to laterally offset shear wave methods.

4.4 Discussion

We have presented an acoustic radiation force-based method of quantifying shear modulus at the region of excitation. The results show that an advanced displacement estimator is needed to measure displacements on-axis of the acoustic radiation force push to generate stiffness estimates comparable to shear wave speed-derived stiffness estimates. When tracking displacements on-axis at the push location, there is high signal decorrelation and

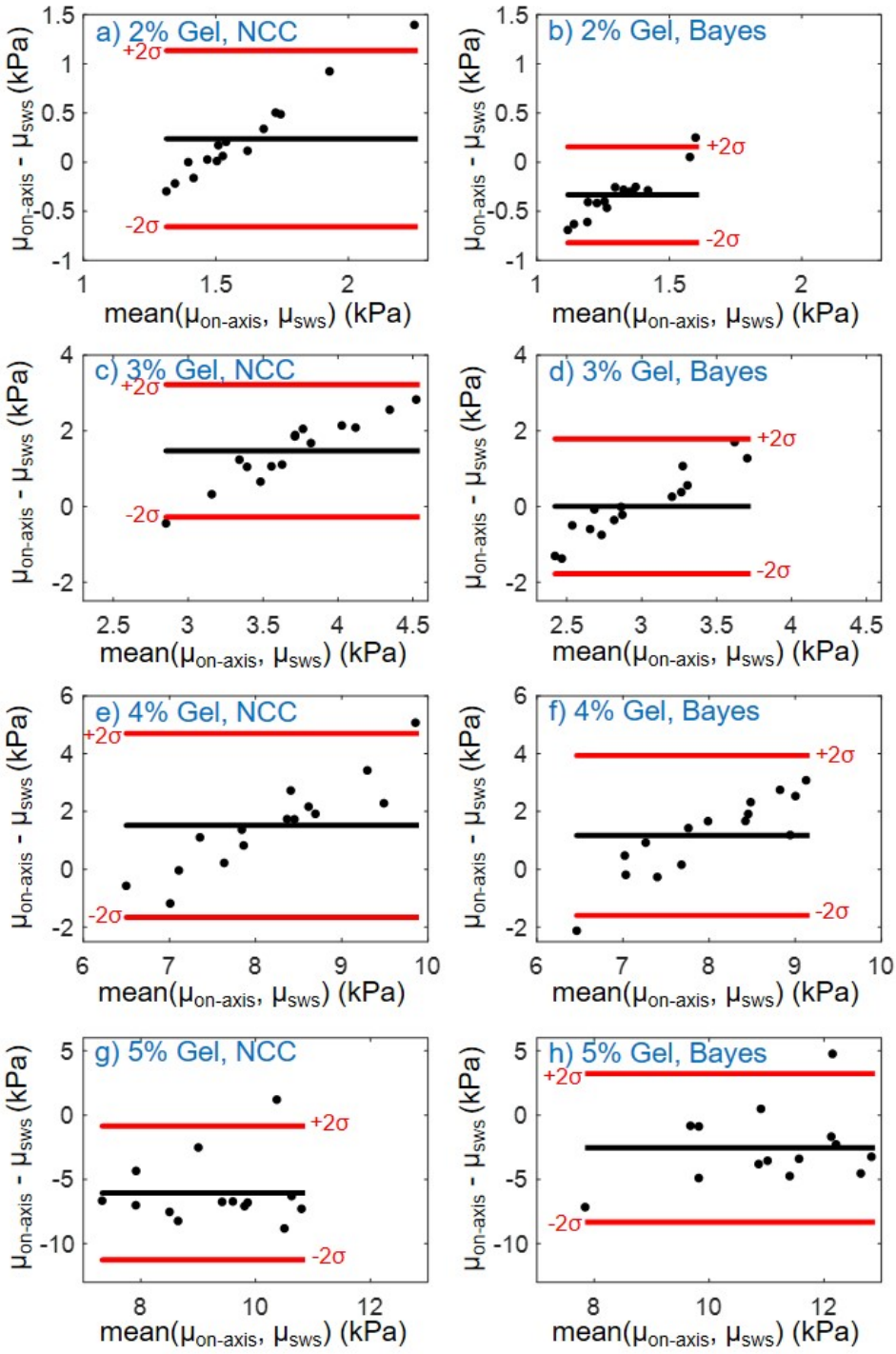

Figure 4.4: Bland-Altman plots comparing the phantom data shear modulus estimates using two methods: the on-axis method using (left column) normalized cross-correlation (NCC) or (right column) Bayesian (Bayes) displacement estimator compared to the lateral shear wave speed-derived stiffness estimate. The y-axis is the difference in shear moduli between the two methods (on-axis or lateral shear wave speed-derived estimate) and the x-axis is the average of the two estimates. The red lines show +/- 2 standard deviations from the mean difference shown as the black line. Compared to NCC, the on-axis Bayesian displacement estimator results show more agreement in all of the phantoms.

Table 4.3: Phantom shear modulus results using the on-axis method. Mean, standard deviation (st. dev.), root mean square error (RMSE), and bias. The error and bias were calculated using the shear wave speed-derived shear moduli as the gold standard.

	Mean (kPa)	St. Dev. (kPa)	RMSE (kPa)	Bias (kPa)
2% Gelatin				
Bayesian	1.1	0.26	0.41	-0.33
NCC	1.7	0.47	0.49	0.24
3% Gelatin				
Bayesian	3.0	0.84	0.86	0.003
NCC	4.4	0.87	1.7	1.5
4% Gelatin				
Bayesian	8.6	1.5	1.8	1.2
NCC	8.9	1.7	2.2	1.5
5% Gelatin				
Bayesian	9.8	2.3	3.8	-2.6
NCC	6.3	1.8	6.6	-6.1

shearing within the point spread function that causes commonly used displacement estimators, such as normalized cross-correlation, to fail. We applied a Bayesian displacement estimator, which lowered the variance in the displacement estimates, allowing us to capture more accurate time-to-peak displacements. The simulation and phantom results show that the error in shear modulus estimates is reduced when using the Bayesian displacement estimator over normalized cross-correlation. The phantom results show we can apply the simulated look-up tables to experimental data and there is good performance of the on-axis method at the focal depth. The error in our shear modulus estimates is on the order of traditional shear wave speed measurement errors [34].

Like SWEI, the error of our measurements increases when the tissue is stiffer due to the declining ability to track faster propagation of displacements. The stiffness estimation quality depends on how accurately we capture the on-axis displacement profile and the location of the maximum displacement. We can improve the stiffness estimation quality by increasing the tracking PRF to better identify the location of the peak. This can also

improve our stiffness estimates in stiffer tissues. However, we capture less samples in our displacement profile when the peak on-axis displacement occurs faster which contributes to lower estimation accuracy in stiffer phantoms. For example, we have better stiffness estimates in the softer gelatin phantoms, but the 5% gelatin phantom has worse performance due to this aspect of the look-up table (Figure 4.3). Also, the method would fail when you cannot accurately capture the peak, so it is necessary to acquire a sample before the tissue reaches the maximum displacement to ensure you are not sampling after the peak on-axis displacement has occurred.

The look-up table is modeled using assumptions about the acoustic radiation force applied to the tissue. When the ARF is applied, the transfer of momentum into the tissue medium is not rigorously modeled in the FEM framework, which could introduce errors in our algorithm. Because this method relies on the time-to-peak displacement, any additional time for the transfer of momentum to occur in tissue could introduce bias. Also, the acoustic radiation force is modeled using Equation 4.1 which is based on the assumption that other sources of attenuation are negligible compared to absorption. If there are other sources of attenuation, this could introduce errors.

Compared to traditional SWEI, we could reduce the transducer hardware because we only use on-axis data. We could provide an elasticity point measurement that could be implemented in a single element probe rather than a typical array-based system. This method also differs from SWEI in the use of a stiffness look-up table. The relationship between stiffness and time-to-peak displacement is formed in simulations based on our transducer configuration. Our look-up table approach does not use Equation 4.2 to get a stiffness estimate. Therefore, we may be able to better estimate different types of tissue structure, such as anisotropic tissues, by measuring on-axis to reduce the effects of complicated wave propagation as a shear wave propagates in anisotropic media. Future work includes applying the on-axis stiffness elasticity method to non-homogeneous phantoms and tissues and *in vivo* data.

4.5 Conclusion

We have demonstrated a method to use a simulated stiffness look-up table for on-axis acoustic radiation force-based elasticity estimation. The phantom results show the on-axis method coupled with a Bayesian displacement estimator produce stiffness estimates comparable to laterally offset shear wave methods and we can apply a simulated look-up table to real experimental data. We have shown that we can produce quantitative stiffness estimates at the acoustic radiation force location in phantoms of different elasticities.

Chapter 5

Improving Speed of Advanced Bayesian Displacement Estimation Algorithm with Analytical Derivatives and Newton's Method

This work is currently in preparation for publication: Walsh, Kristy, et al. "Improving Speed of Advanced Bayesian Displacement Estimation Algorithm with Analytical Derivatives and Newton's Method ".

5.1 Introduction

The quality of acoustic radiation force-based elastography greatly depends on the ability to measure tissue displacement, especially in high shear, noisy environments, or measuring displacement directly at the push location. The previous chapters have shown the importance of using an advanced displacement estimator at the push location. However, the downside is a higher computational cost. The Bayesian displacement estimator described in Section 2.2.1 is solved as a recursive, nonlinear optimization problem. The original publications used quasi-Newton, line-search methods to implement the minimization [67, 68]. These methods did not use analytical derivatives to reach the solution, but approximated the derivatives using finite differences. To reach a solution faster and reduce the computational cost, we have solved for the gradient and Hessian of the Bayesian displacement estimator equation and implemented Newton's method.

5.2 Methods

5.2.1 Bayesian Displacement Estimation

As described in Section 2.2.1, Bayesian methods have been employed to reduce variance and perform better in a mean square error sense than a Cramer-Rao lower bound

(CRLB) limited estimate by using a biased estimation scheme [24, 25, 26, 67, 68]. We apply the Bayesian displacement estimator to RF data to calculate displacement and reduce estimation variance. The Bayesian displacement estimator uses the Bayes' Theorem to estimate a posterior probability density function (PDF) of a displacement estimate, τ_k, given the observed RF data, x, shown here as,

$$P_k(\tau_k|x) = \frac{P_k(x|\tau_k)P_k(\tau_k)}{P_k(x)}, \tag{5.1}$$

where $P_k(x|\tau_k)$ is the likelihood function, $P_k(\tau_k)$ is the prior PDF, and $P_k(x)$ is the marginal likelihood PDF [25, 26, 67]. In short, the Bayesian displacement estimator finds the displacements, τ_k, that maximize the posterior PDF of a set of displacement estimates and the observed RF data. We can describe the terms in Equation 5.1 in the log-domain as,

$$\ln(P_k(\tau_k|x)) \propto -\frac{1}{4\sigma_n^2}\sum_{s=0}^{M-1}(r_k[s] - t_k[s;-\tau_k])^2 - \frac{1}{p\lambda^p}\sum_{k,j\in B} w_j|\tau_k - \tau_j|^p, \tag{5.2}$$

which is advantageous and allows us to separate the likelihood term and prior term. The first term in Equation 5.2, the log likelihood, represents the quality of the current estimate kernel. The likelihood term is the sum-squared difference between the reference RF signal, $r_k[s]$, and the tracked RF signal, $t_k[s;-\tau_k]$, delayed by $-\tau_k$. The second term in Equation 5.2, the prior PDF term, incorporates the additional information into the posterior PDF and is modeled as a generalized Gaussian Markov Random Field (GGMRF) prior that assumes displacement estimates, τ_j, that are spatially adjacent from the current displacement estimate, τ_k, are a reasonable source of knowledge for describing the prior information [89, 67]. The likelihood and prior terms will be described in more detail in the next sections.

To find the displacement estimates, we apply the *maximum a posteriori* principle to Equation 5.2 for all N kernels in the dataset, shown as,

$$\hat{\vec{\tau}} = \text{argmax}\sum_{k=0}^{N-1}\ln P_k(\tau_k|x), \tag{5.3}$$

which maximizes the global log-posterior probability of displacements given our data. To solve for the vector of displacement estimates, optimization routines can be used to find the minimum of the negative global log-posterior probability. The original publications used quasi-Newton, line-search methods to implement the minimization [67, 68]. These methods did not use analytical derivatives to reach the solution, but approximated the derivatives using finite differences which was computationally expensive. In the next sections, we derive analytical derivatives of the two terms of the Bayesian displacement estimator: the likelihood function and the prior function. Then, we describe the optimization methods used to find the displacement estimates with and without the analytical derivatives and evaluate the execution times.

5.2.2 Likelihood Function

As described in Section 2.2.1, the likelihood function of the Bayesian displacement estimator is derived from a minimum mean square error estimator, the sum squared difference. The log likelihood function $f_L(\tau_k)$ is described as,

$$f_L(\tau_k) = -\frac{1}{4\sigma_n^2} \sum_{s=0}^{M-1} (r_k[s] - t_k[s; -\tau_k])^2, \tag{5.4}$$

which includes the sum-squared difference between the reference RF signal, $r_k[s]$, and the tracked RF signal, $t_k[s; -\tau_k]$, delayed by $-\tau_k$ over the kernel length M. The likelihood term is weighted by an adaptive noise term, σ_n^2, to account for the noise and decorrelation in both RF signals shown as,

$$\sigma_n^2 = \frac{P_{RF}}{SNR_\rho + 1}, \tag{5.5}$$

where P_{RF} is the power of the RF signal. SNR_ρ is derived from the peak correlation-coefficient estimate of the SNR shown as,

$$SNR_\rho = \frac{\rho_{max}}{1 - \rho_{max}}, \tag{5.6}$$

where ρ_{max} is the peak of the normalized cross-correlation between the two signals over the kernel k [25, 26].

5.2.2.1 Gradient of Likelihood Function

The gradient of a function is a vector of first partial derivatives of the function at points k. It can be interpreted as the direction and rate of fastest increase or decrease. In optimization, you can maximize or minimize the function to find where the derivative is zero and solve for an optimal set of values for a certain parameter. The gradient of the Bayesian displacement estimator in Equation 5.2 can be described as,

$$\nabla f(\tau_k) = \begin{bmatrix} \frac{\partial f}{\partial \tau_1} \\ \frac{\partial f}{\partial \tau_2} \\ \frac{\partial f}{\partial \tau_3} \\ \vdots \\ \frac{\partial f}{\partial \tau_N} \end{bmatrix} \tag{5.7}$$

which is a vector of derivatives with respect to the displacement τ_k at the axial location k [90]. The gradient of the likelihood function in Equation 5.4 is evaluated as,

$$\nabla f_L(\tau_k) = \frac{\partial f_L}{\partial \tau_k} = \frac{1}{2\sigma_n^2} \sum_{s=0}^{M-1} (r_k[s] - t_k[s;-\tau_k]) \left(\frac{\partial t_k[s;-\tau_k]}{\partial \tau_k} \right). \tag{5.8}$$

To analytically solve for $\left(\frac{\partial t_k[s;-\tau_k]}{\partial \tau_k} \right)$, the derivative of the tracked signal, we first upsample the delayed RF signal and model it as a polynomial. This is calculated only on the first iteration and updated with the new displacements, τ_k, on each iteration. We also compute a forward and backward difference at the edges to approximate the gradient at the boundaries.

5.2.2.2 Hessian of Likelihood Function

The Hessian is an N-by-N matrix of partial derivatives of a function [91]. It is interpreted as the local curvature of a function and like the gradient, it can be used in optimization to find a local minima or maxima. We describe it here and use it later in Newton's method. The Hessian of the Bayesian displacement estimator can be described as,

$$\mathbf{H}_f = \begin{bmatrix} \frac{\partial^2 f}{\partial \tau_1^2} & \frac{\partial^2 f}{\partial \tau_1 \partial \tau_2} & \frac{\partial^2 f}{\partial \tau_1 \partial \tau_3} & \cdots & \frac{\partial^2 f}{\partial \tau_1 \partial \tau_N} \\ \frac{\partial^2 f}{\partial \tau_2 \partial \tau_1} & \frac{\partial^2 f}{\partial \tau_2^2} & \frac{\partial^2 f}{\partial \tau_2 \partial \tau_3} & \cdots & \frac{\partial^2 f}{\partial \tau_2 \partial \tau_N} \\ \frac{\partial^2 f}{\partial \tau_3 \partial \tau_1} & \frac{\partial^2 f}{\partial \tau_3 \partial \tau_2} & \frac{\partial^2 f}{\partial \tau_3^2} & \cdots & \frac{\partial^2 f}{\partial \tau_3 \partial \tau_N} \\ \vdots & \vdots & \vdots & \ddots & \vdots \\ \frac{\partial^2 f}{\partial \tau_N \partial \tau_1} & \frac{\partial^2 f}{\partial \tau_N \partial \tau_2} & \frac{\partial^2 f}{\partial \tau_N \partial \tau_3} & \cdots & \frac{\partial^2 f}{\partial \tau_N^2} \end{bmatrix}. \tag{5.9}$$

In terms of the partial derivatives in the Hessian, the likelihood function only has dependence on τ_k which is the displacement estimate at the current axial location. Therefore, the likelihood function only contributes to the diagonal of the Hessian matrix and all other terms are zero. The Hessian of the likelihood function is,

$$\mathbf{H}_{f_L} = \begin{bmatrix} \frac{\partial^2 f_L}{\partial \tau_1^2} & 0 & 0 & \cdots & 0 \\ 0 & \frac{\partial^2 f_L}{\partial \tau_2^2} & 0 & \cdots & 0 \\ 0 & 0 & \frac{\partial^2 f_L}{\partial \tau_3^2} & \cdots & 0 \\ \vdots & \vdots & \vdots & \ddots & \vdots \\ 0 & 0 & 0 & \cdots & \frac{\partial^2 f_L}{\partial \tau_N^2} \end{bmatrix}. \tag{5.10}$$

The diagonal terms in the Hessian matrix are found by taking the derivative of Equation 5.8 (the gradient of the likelihood function) with respect to τ_k. Using the product rule, we evaluated the second derivative of the likelihood function as,

$$\frac{\partial^2 f_L}{\partial \tau_k^2} = \frac{1}{2\sigma_n^2} \sum_{s=0}^{M-1} \left[(r_k[s] - t_k[s; -\tau_k]) \left(\frac{\partial t_k^2[s; -\tau_k]}{\partial \tau_k^2} \right) - \left(\frac{\partial t_k[s; -\tau_k]}{\partial \tau_k} \right)^2 \right]. \tag{5.11}$$

Similar to $\left(\frac{\partial t_k[s;-\tau_k]}{\partial \tau_k}\right)$, we can find $\left(\frac{\partial t_k^2[s;-\tau_k]}{\partial \tau_k^2}\right)$ analytically on the first iteration using the second order central difference equation on the delayed RF signal that has been upsampled and modeled as a polynomial. We also approximate the second derivatives at the edges using forward and backward second differences.

5.2.3 Prior Function

The second term of the Bayesian displacement estimator is the prior probability function. As described in Section 2.2.1, the prior probability function includes the additional information from the surrounding axial displacement estimates, τ_j, and is written as,

$$f_{Prior}(\tau_k) = -\frac{1}{p\lambda^p} \sum_{k,j \in B} w_j |\tau_k - \tau_j|^p, \tag{5.12}$$

where τ_k is the current displacement estimate, w_j weights the adjacent displacement estimates in the neighborhood B [69]. In this work, we chose a neighborhood B of 3 which means $j = k-1, k, k+1$. The weighted prior term also has tuning parameters λ and p which modulate the distribution of the prior PDF. In the Bayesian displacement estimator, a p of 2 gives the prior PDF a Gaussian distribution which is computationally faster and tends to more accurately preserve the axial displacement profile in a homogeneous region [67]. We chose λ empirically based on the median axial SNR_ρ and the maximum displacement of the prior. This allows the algorithm to scale the width of the prior without biasing the result away from the true displacement [67]. In practice, the absolute value $|\tau_k - \tau_j|^p$ is approximated by a smooth function $\left(\sqrt{((\tau_k - \tau_j)^2 + \varepsilon)}\right)^p$ where ε is a small number ($\varepsilon = 10^{-6}$) [67, 92].

5.2.3.1 Gradient of Prior Function

The gradient from Equation 5.7 can be applied to the prior function and solved as,

$$\frac{\partial f_{Prior}}{\partial \tau_k} = \left(-\frac{w_j}{\lambda^p}\right) \sum_{k,j \in B} \left[(\tau_k - \tau_j) \left((\tau_k - \tau_j)^2 + \varepsilon \right)^{\left(\frac{p}{2}-1\right)} \right], \tag{5.13}$$

where $(\tau_k - \tau_j)$ is the difference between the current displacement estimate and adjacent displacement estimates and is summed over a neighborhood B $(j = k-1, k, k+1)$. When computing $(\tau_k - \tau_j)$ and $(\tau_k - \tau_j)^2$, it is also necessary to include boundary conditions at the edge locations where the neighborhood is undefined. We approximated the displacements at the boundaries using finite differences.

5.2.3.2 Hessian of Prior Function

In the gradient of the prior function in Equation 5.13, there is dependence on variables at the current location k and at locations j that surround k. The partial derivatives with respect to the j location can also be found analytically and used to create a Hessian matrix of second partial derivatives. The neighborhood of $j = k-1, k, k+1$ will give us a tridiagonal Hessian matrix. We constructed a Hessian matrix of the prior function shown as,

$$\mathbf{H}_{f_{Prior}} = \begin{bmatrix} \frac{\partial^2 f_{Prior}}{\partial \tau_1^2} & \frac{\partial^2 f_{Prior}}{\partial \tau_1 \partial \tau_2} & 0 & \cdots & 0 \\ \frac{\partial^2 f_{Prior}}{\partial \tau_2 \partial \tau_1} & \frac{\partial^2 f_{Prior}}{\partial \tau_2^2} & \frac{\partial^2 f}{\partial \tau_2 \partial \tau_3} & \cdots & 0 \\ 0 & \frac{\partial^2 f_{Prior}}{\partial \tau_3 \partial \tau_2} & \frac{\partial^2 f_{Prior}}{\partial \tau_3^2} & \cdots & 0 \\ \vdots & \vdots & \vdots & \ddots & \vdots \\ 0 & 0 & 0 & \cdots & \frac{\partial^2 f_{Prior}}{\partial \tau_N^2} \end{bmatrix}. \tag{5.14}$$

The diagonal of the Hessian matrix of the prior is the second partial derivative with

respect to τ_k which is,

$$\frac{\partial^2 f_{Prior}}{\partial \tau_k^2} = \left(-\frac{w_j}{\lambda^p}\right) \sum_{k,j \in B} \Bigg[(\tau_k - \tau_j)^2 (2-P) \left((\tau_k - \tau_j)^2 + \varepsilon\right)^{\left(\frac{p}{2}-2\right)} + \left((\tau_k - \tau_j)^2 + \varepsilon\right)^{\left(\frac{p}{2}-1\right)} \Bigg]. \tag{5.15}$$

The second partial cross derivative terms in Equation 5.14 at the j locations are,

$$\frac{\partial^2 f_{Prior}}{\partial \tau_k \partial \tau_j} = \left(-\frac{w_j}{\lambda^p}\right) \sum_{k,j \in B} \Bigg[(\tau_k - \tau_j)^2 (2-P) \left((\tau_k - \tau_j)^2 + \varepsilon\right)^{\left(\frac{p}{2}-2\right)} - \left((\tau_k - \tau_j)^2 + \varepsilon\right)^{\left(\frac{p}{2}-1\right)} \Bigg], \tag{5.16}$$

which will constitute the upper and lower diagonals of the Hessian matrix. Each term is still summed over the neighborhood B.

5.2.4 Run Time Experiments

The run time was evaluated in simulations modeling the response of homogeneous tissue to an acoustic radiation force-induced displacement. The simulation method is described in Section 3.2.2 and the parameters are listed in Table 3.1 [19]. We simulated a linearly elastic, isotropic phantom with a shear modulus of 6 kPa. Field II was used to calculate the pressure field of the experimental transducer configuration [73]. LS-DYNA (Livermore Software Technology Corporation, Livermore, CA) was used to simulate the displacements induced by the ARF push [19]. The 3D mesh extended 6.1 cm axially, 2.0 cm laterally, and 0.3 cm in elevation. The transducer was a C5-2 and the ARF push used an F/1.5, center frequency of 2.3585 MHz, duration of 128 μs, and focus of 4.98 cm in depth. The ultrasonic tracking used a center frequency of 3.125 MHz. After Field II simulated the tracked response, additive white Gaussian noise was added to the RF signals to achieve an SNR of 10 or 30 dB. We simulated 100 independent speckle realizations for each SNR and

tested the run time for the displacement estimation algorithms using two RF lines of the acoustic radiation force-based displacement data.

5.2.5 Optimization Routines

The Bayesian displacement estimator in Equation 5.2 is solved as a minimization problem. Equation 5.3 is summed axially over the region-of-interest to solve for a vector of displacements, τ_k, that maximize the global log-posterior probability (i.e., minimizes the negative global log-posterior probability) given our data and the adjacent displacement estimates. We implemented the minimization routines described in the following sections in MATLAB (The Mathworks Inc., Natick, MA, USA) on a Dell Precision T5600 Intel Xeon 3.1 GHz computer with 16 GB memory.

5.2.5.1 Unconstrained Minimization Solvers

We tested two pre-existing nonlinear unconstrained minimization solvers. The first was a MATLAB function, fminunc. The second optimizer was a program called minFunc written by Schmidt (2005) that offers a variety of nonlinear unconstrained minimization solvers, similar to MATLAB's fminunc [70]. We used a quasi-Newton method with a low-memory BFGS and line search algorithm for each solver. First, we supplied the full Bayesian displacement estimator in Equation 5.2. The solvers use finite differences to estimate the gradient. Then, they use the estimated gradients to approximate a Hessian which is why it is not a full Newton's method. We tested the run time and observed the displacement estimation output and compared it to normalized cross-correlation described in Section 2.2.2.

The solvers can also be supplied with the analytical gradient of the function to be optimized. This will save computation time because it will not have to use finite differences to solve for the gradient or approximate the Hessian. The gradient of the Bayesian displacement estimator is the sum of the gradient of the likelihood and prior functions from

Equations 5.8 and 5.13, respectively, and shown as,

$$\nabla f_i = \frac{\partial \ln(P_k(\tau_k|x))}{\partial \tau_k} = \frac{\partial f_L}{\partial \tau_k} + \frac{\partial f_{Prior}}{\partial \tau_k}. \tag{5.17}$$

We tested the performance of the solvers using a quasi-Newton algorithm with the analytical gradient in Equation 5.17 included.

We also tested inputting the analytical Hessian matrix into each solver. The Hessian of the Bayesian displacement estimator includes the second partial derivatives of the likelihood function and the prior function from Equations 5.10 and 5.14, respectively, and is shown as,

$$\mathbf{H}_i = \mathbf{H}_{\ln(P_k(\tau_k|x))} = \mathbf{H}_{f_L} + \mathbf{H}_{f_{Prior}}. \tag{5.18}$$

In MATLAB's fminunc, we used the trust-region algorithm which uses the gradient and Hessian to approximate the search region that is being minimized. In minFunc, we used the full Newton's method algorithm (described more in the next section) with the gradient and Hessian inputs. We tested the run time of each solver.

5.2.5.2 Newton's Method

In this section, we describe using Newton's method that we manually coded in MATLAB without using a pre-existing solver. Newton's method is used in optimization to find a minimum of a function that has multiple variables and is twice differentiable. It uses the gradient and Hessian described in the previous section. Newton's method requires the function to have an invertible Hessian matrix. In the Bayesian displacement estimator, we have an analytically solvable gradient and Hessian and a defined number of axial locations that determine the size of our Hessian matrix that is not too costly to compute. In this Newton's method, we find the vector of displacements, $\hat{\vec{\tau}}_{i+1}$, by iterating the equation,

$$\hat{\vec{\tau}}_{i+1} = \tau_i - \gamma[\mathbf{H}_i]^{-1}(\nabla f_i) \tag{5.19}$$

where τ_i is the displacement estimate vector for the current iteration, γ is the relaxation step size, $\mathbf{H}_i$ is the Hessian matrix from Equation 5.18, and ∇f_i is the gradient from Equation 5.17. This is iterated until it reaches below a tolerance in the change of overall probability or a specified number of iterations. We ran Newton's method using the full analytical gradient and Hessian for various relaxation step sizes and showed the performance.

The Bayesian displacement estimator is supplied with an initial guess of the displacement estimates before minimization. In Newton's method, we can also set an initial guess for the displacement estimates at the first iteration for $\tau_{i=0}$. Typically when solving the Bayesian displacement estimator, the initial guess is set to the normalized cross-correlation solution. To test an uninformed guess, we can supply the estimator with initial displacements of zero. We compare the performance of the estimator with the informed (normalized cross-correlation displacements) and uninformed (zero) initial guesses.

The two terms of the Bayesian displacement estimator, the likelihood and the prior, are separable. Therefore, we can also solve the equation using either term. We can solve for the likelihood function solution by turning the prior weights to zero and implementing Newton's method. This implementation would only include the gradient of the likelihood term in Equation 5.8 and the Hessian of the likelihood term from Equation 5.10 which only includes the center diagonal. We tested the likelihood function solution using Newton's method without the prior information and reported the run time and result.

5.3 Results

5.3.1 Unconstrained Minimization Solvers

The two pre-existing optimization solvers used were MATLAB's fminunc and Schmidt's minFunc [70]. The Bayesian displacement estimator equation is solved first without using analytical derivatives. Two examples of simulated phantoms with SNRs of 10 and 30 dB are shown in Figure 5.1. We timed the solvers to compute the displacement estimate be-

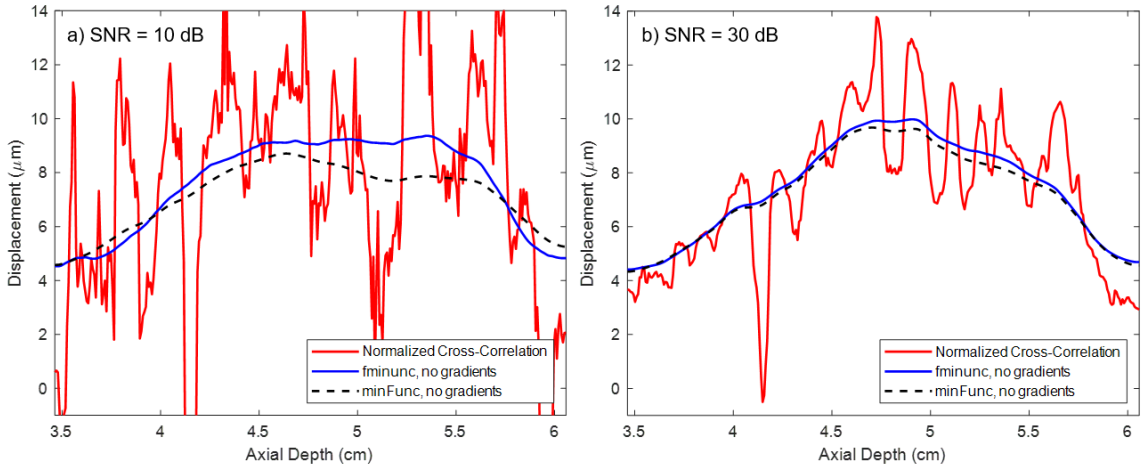

Figure 5.1: Bayesian displacement estimator results for the pre-existing minimization solvers, fminunc and minFunc, without using analytical derivatives in one example for each SNR a) 10 dB and b) 30 dB. Also, normalized cross-correlation is shown in red. The Bayesian displacement estimator was initialized with normalized cross-correlation and ran until it reached a convergence tolerance ($10e^{-6}$) or a maximum of 1000 iterations.

tween two RF lines for 100 cases for each SNR. The execution time results are shown in Table 5.1. For an SNR of 30 dB, normalized cross-correlation took 0.092±0.03 seconds (s), and for reaching a Bayesian displacement estimator solution, fminunc took 90.86±0.96 s, and minFunc took 228.1±77.2 s. To reach a regularized Bayesian solution, this method has a high computational cost for estimating the displacement of only one RF line.

Including the analytical gradient into the solvers greatly reduces the computational time. Figure 5.2 show the results of each solver with the analytical gradient included. Both fminunc and minFunc are using a quasi-Newton algorithm and line search methods. The execution time results are shown in Table 5.1. For an SNR of 30 dB, fminunc took 1.07±0.19 s, and minFunc took 0.83±0.21 s. Both solvers perform similarly well, but minFunc has faster convergence.

Additionally, the full Hessian matrix can be used as an input to these solvers. In fminunc, it uses the trust-region algorithm to solve the equation when the full Hessian is an input. In minFunc, we used full Newton's algorithm. The displacement results are shown in Figure 5.3. Both solvers actually took longer when the Hessian was included, so it does not

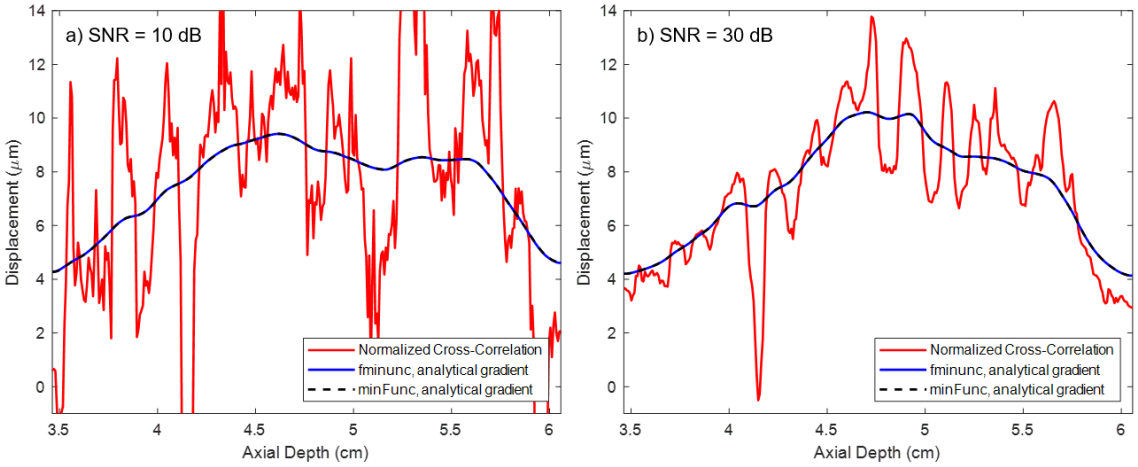

Figure 5.2: Bayesian displacement estimator results for the pre-existing minimization solvers, fminunc and minFunc, using analytical derivatives as inputs in one example for each SNR a) 10 dB and b) 30 dB. Also, normalized cross-correlation is shown in red. The Bayesian displacement estimator was initialized with normalized cross-correlation and ran until it reached a convergence tolerance ($10e^{-6}$) or a maximum of 1000 iterations.

provide a computational benefit for these methods. For the 30 dB SNR cases, MATLAB's fminunc took 20.4±4.33 s and minFunc took 74.4±54.1 s. The additional time is due to computational checks that the optimizing algorithms perform on the inputted Hessian prior to starting the optimization.

5.3.2 Newton's Method

To eliminate any extra computations in the pre-existing solvers, we coded our own Newton's method to solve the Bayesian displacement estimator using Equation 5.19 and the analytical gradient and Hessian matrix. Using the full Hessian matrix from Equation 5.18, we solved the Bayesian displacement equation with the cross derivatives incorporating the neighboring displacement estimate information into the prior terms. We started with the normalized cross-correlation solution for the initial guess of the displacement estimates to show the performance of an informed initial guess. Figure 5.3 shows the displacement results for our Newton's method using the gradient and full Hessian matrix after 1000 iterations with a dotted magenta line. The method is able to converge to a solution using a large

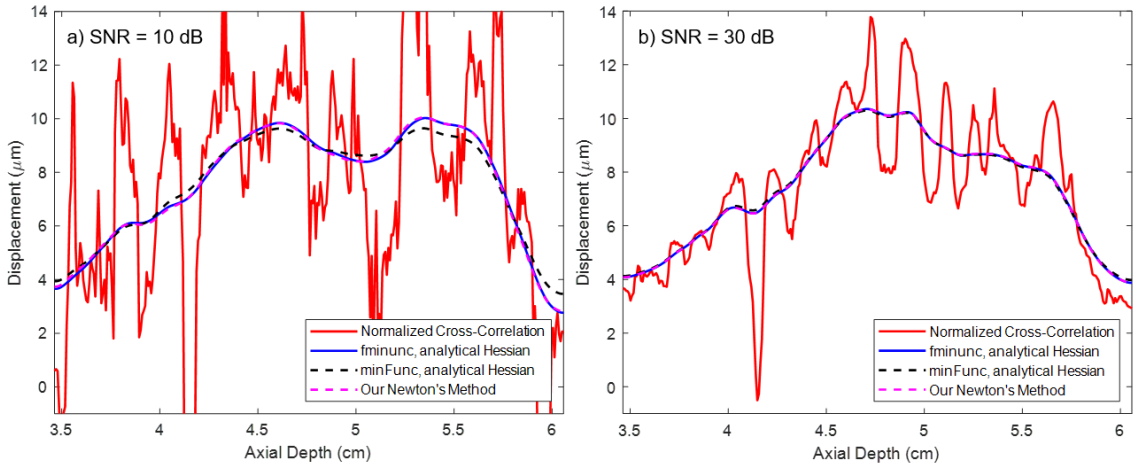

Figure 5.3: Bayesian displacement estimator results for the pre-existing minimization solvers, fminunc and minFunc, using analytical gradient and Hessian as inputs in one example for each SNR a) 10 dB and b) 30 dB. Also, normalized cross-correlation is shown in red. The Bayesian displacement estimator was initialized with normalized cross-correlation and ran until it reached a convergence tolerance or a maximum of 1000 iterations.

relaxation step size of 1. Figure 5.4a) shows the negative global log-posterior probability that is being minimized at each iteration for this 30 dB SNR example. Figure 5.4b) also shows the displacement estimate at iterations 50, 200, and 1000 as it is converging. For 1000 iterations over 100 simulations at an SNR of 30 dB and a relaxation step size of 1, the coded Newton's method takes 3.75$\pm$0.12 s. The maximum number of iterations can be reduced (or tolerance can be increased) to provide less regularization, but still give a more favorable displacement estimate over normalized cross-correlation. At 200 iterations, the method takes 0.99$\pm$0.04 s at SNRs of 30 dB. These run time results are reported in Table 5.1.

The chosen relaxation step size, γ, can also affect the rate of convergence. If the Hessian matrix is set up incorrectly or becomes ill-conditioned, the method may only work for smaller relaxation step sizes and the optimization will take too long to reach a solution to provide a computational benefit. In Figure 5.5, we can see that the method works for larger relaxation step sizes up to 1 and even 1.5. Figure 5.5a) shows the negative global log-posterior probability that is being minimized at each iteration for this 30 dB SNR example

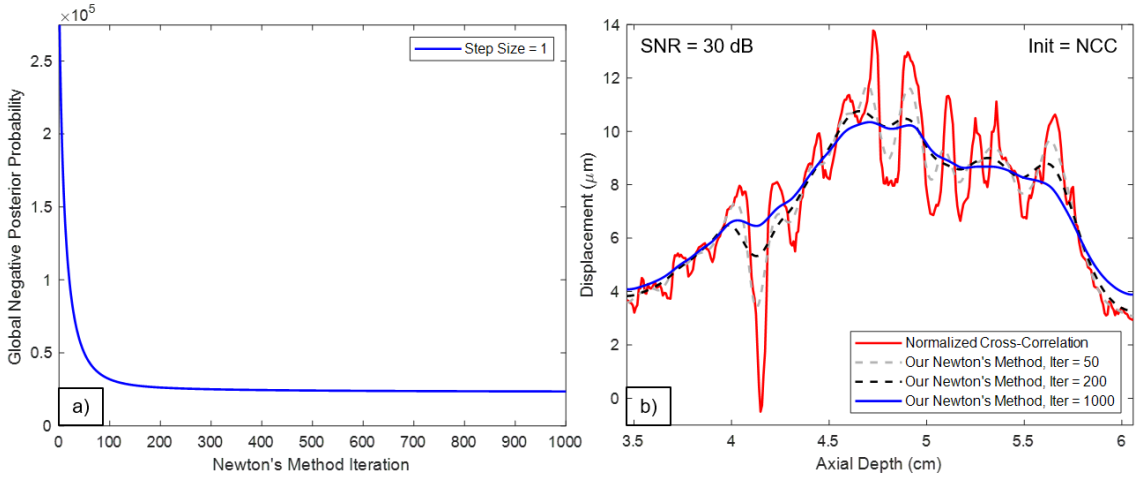

Figure 5.4: a) Negative global log-posterior probability being minimized at each iteration of Newton's method with a relaxation step size of 1. b) Displacement estimation results for normalized cross-correlation and the Bayesian displacement estimator solved with Newton's method at iteration 50, 200, and 1000. The Bayesian displacement estimator was initialized with normalized cross-correlation.

and Figure 5.5b) shows the displacement outputs at relaxation step sizes of 0.1, 0.5, 1, and 1.5 after 200 iterations of Newton's method and initialized with normalized cross-correlation. The run time for each of the relaxation step sizes 0.1, 0.5, 1, and 1.5 that are shown in Figure 5.5 are 1.02±0.04 s, 1.01±0.05 s, 0.99±0.04 s, and 1.01±0.04 s, respectively, for 200 iterations.

Next, we tested the performance of the Bayesian displacement estimator solved with Newton's method using an uninformed initial guess for the displacement estimates. We used the full Hessian matrix and started with initial displacement estimates of zeros. Figure 5.6 shows that we can minimize the global log-posterior probability with a zero initial guess and still converge to a regularized Bayesian displacement estimate. Figure 5.6a) shows the negative global log-posterior probability that is being minimized at each iteration for the 30 dB SNR example for the initial guess of zero with relaxation step sizes 1 and 1.5. For comparison, the minimization with normalized cross-correlation as an initial guess is also shown. Figure 5.6b) shows the displacement outputs for the uninformed initial guesses and informed guess after 1000 iterations of Newton's method. The uninformed initial guesses

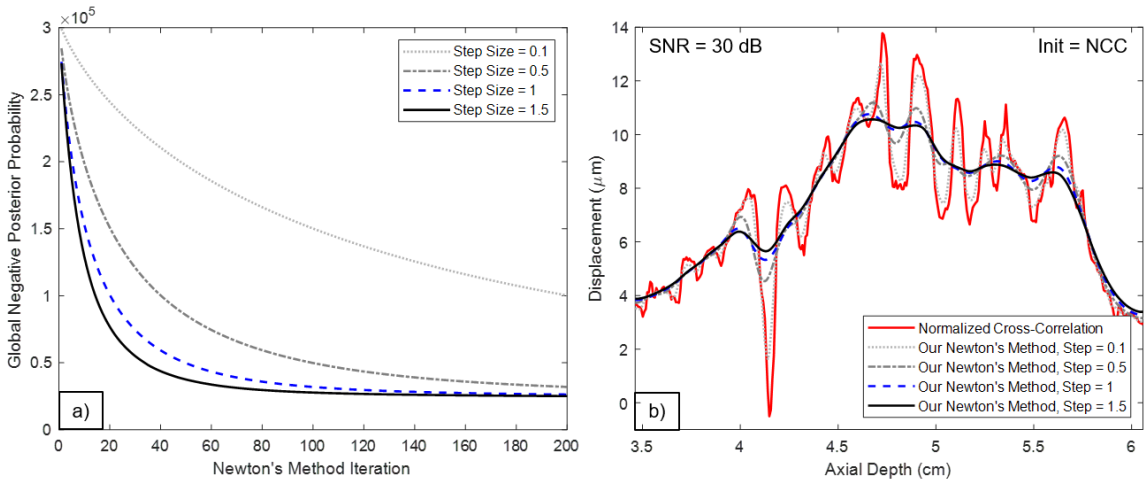

Figure 5.5: a) Negative global log-posterior probability being minimized at each iteration of Newton's method with relaxation step sizes of 0.1, 0.5, 1 and 1.5. b) Displacement estimation results for normalized cross-correlation and the Bayesian displacement estimator solved with Newton's method after 200 iterations using relaxation step sizes of 0.1, 0.5, 1, and 1.5. The Bayesian displacement estimator was initialized with normalized cross-correlation.

are also shown at iteration 200 for both relaxation step sizes and are converging from zero. The run time to reach 1000 iterations of Newton's method with an initial guess of zero is 3.60±0.12 s for a relaxation step size of 1 at 30 dB SNR.

To get a displacement estimate even faster, we can use Newton's method without the prior terms. This will only include the gradient of the likelihood term shown in Equation 5.8 and the Hessian of the likelihood term shown in Equation 5.10. The Hessian will now be only the diagonal of the matrix and the prior weights will be zero. The initial guess can be zero and we can reach a solution similar to normalized cross-correlation in only a few iterations. The five iterations shown in Figure 5.7 only take 0.087±0.006 s for SNRs of 30 dB. These run time results are shown in Table 5.1.

5.4 Discussion

In this section, we have shown methods for optimizing the Bayesian displacement estimator. Without solving for the analytical derivatives, it is computationally costly and can

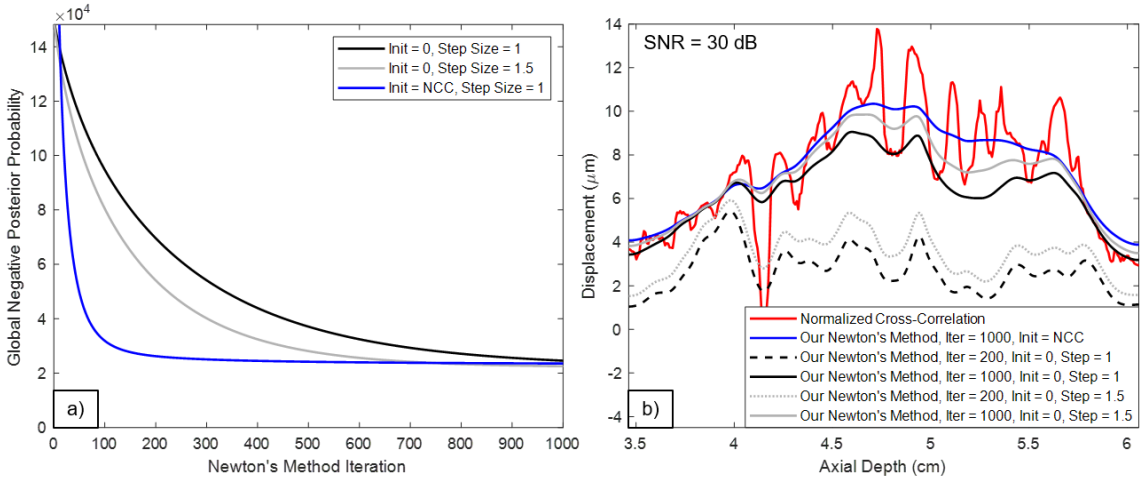

Figure 5.6: a) Negative global log-posterior probability being minimized at each iteration of Newton's method with an initial guess of zeros and relaxation step sizes of 1 and 1.5. The probability for the initial guess of normalized cross-correlation is also shown. b) Displacement estimation results for normalized cross-correlation and the Bayesian displacement estimator solved with Newton's method after 200 and 1000 iterations for the uninformed guess for relaxation step sizes of 1 and 1.5. The displacement estimate results for an initial guess of normalized cross-correlation are also shown.

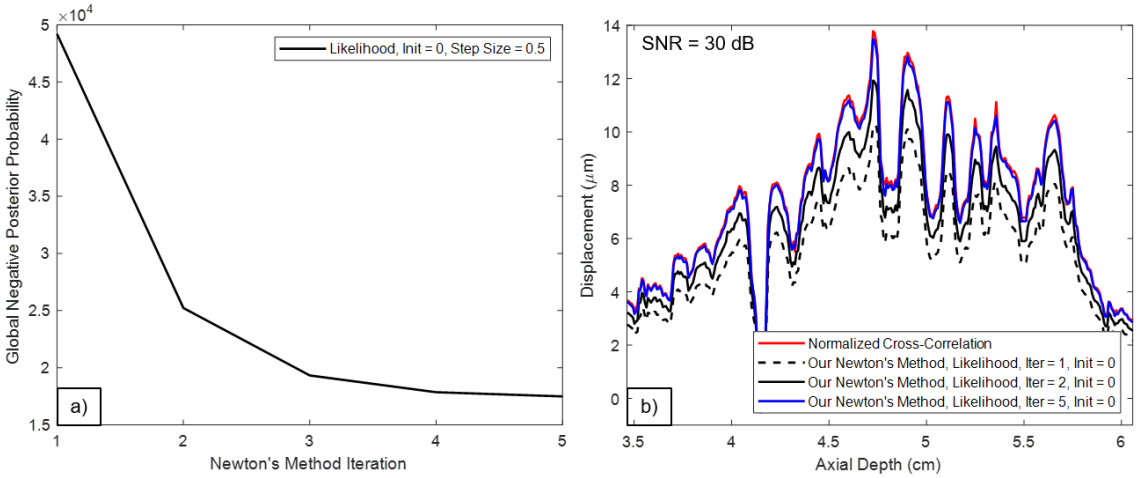

Figure 5.7: a) Negative global log-posterior probability being minimized at each iteration of Newton's method using only the gradient and Hessian of the likelihood function and the prior function is zero. b) Displacement estimation results for normalized cross-correlation and the Bayesian displacement estimator's likelihood function solved with Newton's method after 1, 2, and 5 iterations with an uninformed guess of zeros and a relaxation step sizes of 0.5.

Table 5.1: Simulation Run Time Results

	Execution Time (s)	Iterations
SNR = 10 dB (n = 100)		
NCC	0.093±0.04	—
fminunc, no gradient	90.50±1.55	—
minFunc, no gradient	320.0±83.8	—
fminunc, gradient	1.45±0.21	227.9±42.4
minFunc, gradient	1.08±0.22	159.6±30.4
fminunc, Hessian	15.9±5.57	1000
minFunc, Hessian	73.6±57.5	1000
Coded Newton's Method (Full Eqn, Init=NCC)	3.75±0.17	1000
Coded Newton's Method (Full Eqn, Init=NCC)	0.99±0.05	200
Coded Newton's Method (Likelihood, Init=0)	0.092±0.03	5
SNR = 30 dB (n = 100)		
NCC	0.092±0.03	—
fminunc, no gradient	90.86±0.96	—
minFunc, no gradient	228.1±77.2	—
fminunc, gradient	1.07±0.19	149.4±42.2
minFunc, gradient	0.83±0.21	106.1±19.8
fminunc, Hessian	20.4±4.33	1000
minFunc, Hessian	74.4±54.1	1000
Coded Newton's Method (Full Eqn, Init=NCC)	3.75±0.12	1000
Coded Newton's Method (Full Eqn, Init=NCC)	0.99±0.04	200
Coded Newton's Method (Likelihood, Init=0)	0.087±0.006	5

take over three orders of magnitude longer than normalized cross-correlation to compute Bayesian displacement estimates. Using the analytical gradient as an input to optimization functions can greatly reduce computational time and allow the Bayesian displacement estimator to be solved two orders of magnitude faster. Inputting the Hessian matrix did not provide much computational benefit using the pre-existing optimization solvers discussed in this chapter.

We have shown that Newton's method is stable with the derived analytical gradient and Hessian of the Bayesian displacement equation. In ultrasonic displacement estimation, the axial range and sampling is such that it is not too costly to construct a Hessian matrix for the range of axial locations. Depending on how much data is included in the Hessian, the method could get more costly or the Hessian could become ill-conditioned. However, in our applications, the Hessian of the Bayesian displacement estimator is invertible. Additionally, the method requires correct boundary conditions to maintain stability.

The fastest method to compute a full, regularized Bayesian displacement solution was to use the analytical gradient and minFunc's quasi-Newton algorithm. This method may be reducing computations by approximating the Hessian rather than computing the full Hessian at each iteration in Newton's method. Coding Newton's method manually was faster than using the pre-existing solvers when using the full Hessian matrix. The optimization programs described also have more checks on the Hessian's properties that slow it down. Our problem is well-behaved, so we did not include additional modifications.

There is a trade off between the regularization included with the prior term and run time. If not as much regularization is needed, the method can be run for fewer iterations or an increased tolerance, but still have the benefits of the Bayesian displacement estimator. Figure 5.5 shows a result that has not reached full convergence, but still has an improved estimate over normalized cross-correlation. Because the Bayesian displacement estimator terms are separable, we can also remove the prior terms to reach an unregularized solution even faster. The likelihood-only solution can be solved in only a few iterations starting at

the initial guess of zero.

The analytical gradient and Hessian solutions to the Bayesian displacement estimator improve computational cost and run time. The run times may change based on the device or CPU used to run the code. We have observed changes in run time on different systems, but the trends have been the consistent. There is also potential to code these methods faster in different programming languages. Other ways to reduce computational cost and make the method more robust could be applying an adaptive step size. This method could be improved by automatically choosing a step size for stability.

5.5 Conclusion

We have made improvements in optimizing the advanced Bayesian displacement estimator. We have shown a large improvement in the run time by supplying an optimizing solver function with the analytical gradient. There is also improvement in reducing computational cost by solving for a Hessian matrix and implementing Newton's method. The Bayesian displacement estimator can be solved using full Newton's method with the gradient and Hessian. Additionally, a Bayesian likelihood solution can be reached faster than a normalized cross-correlation solution using Newton's method.

Chapter 6

On-Axis Acoustic Radiation Force-based Elasticity in Layered, Skin-Mimicking Phantoms

Parts of this work were originally presented at and published as a proceedings paper in [93]: Walsh, Kristy, et al. "On-axis acoustic radiation force-based elasticity measurement in homogeneous and layered, skin-mimicking phantoms " *Proc. IEEE Int. Ultrason. Symp. (IUS)* (2018): 1-3. © 2018 IEEE.

6.1 Introduction

An area of ultrasound elasticity imaging that needs improvement is quantitatively measuring skin elasticity. Currently, it is challenging to quantify the elasticity in skin due to the boundary conditions and complex structure. As described in Section 1.3.2, elasticity imaging in the skin has been difficult due to the skin's thin nature and complicated surrounding structures, including subcutaneous fat, muscle, and bone [40, 41]. The skin structure also introduces new challenges to the mechanical models in elasticity because it is composed of thin layers bounded to the substrate, or subcutaneous tissue [40, 42]. Some groups use an external vibration or apply a displacement to the surface of the skin and measure the response using ultrasound. Similar to the FibroScan® system for the liver, a dynamic elastography technique using a vibrator has been tested in the skin, but the proximity of the skin to the transducer and vibrator make it difficult to quantify any shear wave propagation in the skin layer [56]. Another method that has been tested in skin is strain imaging which applies a quasi-static displacement to the tissue surface using the ultrasound transducer and measures the strain. [57, 58]. Others have applied a vacuum suction to the tissue and use high frequencies, around 20 MHz, to measure the strain response [59]. These methods only

estimate relative strain measurements and are not quantitative [59, 57, 58]. They can also be subject to operator variability and often require a contralateral control measurement on the patient which may not be available in all patient populations if the disease is bilateral.

Acoustic radiation forced-based methods can be used to induce a reproducible displacement. Currently, the most common method being developed to quantify the elasticity of skin is shear wave elasticity imaging (SWEI) [41, 60, 61, 62]. SWEI can estimate tissue elastic properties by monitoring displacement induced by shear waves following an acoustic radiation force (ARF) excitation [15]. Assuming the tissue is linearly elastic and isotropic, shear wave speed, c_T, can be related to shear modulus, μ, by $c_T = \sqrt{\mu/\rho}$ at a constant density, ρ. [6]. Common SWEI methods use this equation to reconstruct shear modulus from shear wave speed which can be measured as displacement arriving at lateral locations [31], [16].

Shear wave speed is difficult to measure in heterogeneous and anisotropic regions where there are changes in stiffness and mechanical behavior based on orientation [31, 4]. Also, lesions or tissue boundaries have complex shear wave reflections that corrupt the shear wave speed measurements [4]. From these factors and the thin nature of the skin, SWEI measurements in the skin are biased based on the skin thickness [41]. Some groups attempt to offset this layer-dependent bias by normalizing the shear wave speed measurements by the width of the skin layer, but they still rely on measuring the velocity of a complex shear wave and do not have an analytical model to convert to shear modulus [41, 61, 62]. To get accurate measurements of elasticity from patient to patient, there needs to be an improved quantitative measurement technique. This chapter applies the ARF-based elasticity technique that measures on-axis displacement rather than lateral shear wave speed to reduce the effects of a complicated shear wave propagation in the skin.

We use a finite element method (FEM)-based look-up table to estimate shear modulus at the on-axis location rather than at lateral locations. We estimate the time-to-peak on-axis displacement at each depth in the focal region and use a look-up table to esti-

mate shear modulus. We have shown that measuring on-axis displacements requires an advanced displacement estimator, such as a Bayesian displacement estimator, which we have demonstrated in homogeneous simulations and phantoms [66], [72], [65]. Here, we test the ability to quantify elasticity in layered phantoms using the on-axis method with an FEM look-up table and compare the results to shear wave speed-derived shear modulus estimates in the layers. To quantify the elasticity of the layers, we first measure a robust shear wave speed in a homogeneous region of a phantom. Then, we slice the phantoms into thin layers where the shear wave speed estimate was measured and acquire another matched shear wave speed and on-axis estimate in the layers. We construct layered phantoms using two materials: Polyvinyl alcohol (PVA), which changes elasticity after freeze/thaw cycles and gelatin, which changes elasticity by varying the concentration of gelatin powder. We analyzed both materials because the freeze/thaw cycles of polyvinyl alcohol cause large changes in stiffness and we can observe more elasticities by creating phantoms using different concentrations of gelatin. This chapter shows a method of validating the elasticity in each of the thin, layered phantoms and the preliminary shear modulus estimates.

6.2 Methods

6.2.1 FEM Simulation-based Stiffness Look-up Table

We generated a stiffness look-up table using a 3D FEM model coupled to Field-II simulations [73, 19]. We simulated the response of tissues with shear moduli of 0.33-13kPa using the parameters listed in Table 6.1. The ARF excitation was modeled in Field II with a CL15-7 transducer, 1.1 cm axial push focus, 8.9286 MHz push center frequency, push F/3, and elevational focus of 1.5 cm. We also tested changing the location of the modeled transducer's elevational focus to 1.1 cm to correspond to the focus of the push and the layered phantom location. We simulated isotropic, linearly elastic, and homogeneous tissue with an attenuation of 0.5 dB/cm/MHz, constant density of 1.0 g/cm^3 and a Poisson's ratio

Table 6.1: CL15-7 simulation parameters

Option	Parameter Value
Transducer	CL15-7
Attenuation	0.5 dB/cm/MHz
Speed of Sound	1540 m/s
Push Center Freq.	8.9286 MHz
Excitation F/#	3
Excitation Focal Depth	1.1 cm
Push Duration	180 μs
Tracking Center Freq. (f_c)	10.4167 MHz
Tracking Pulse Repetition Freq. (PRF)	20 kHz
Receive F/#	1
Sampling Freq. (Field-II Simulation)	160 MHz
Sampling Freq. (RF Down-Sampled)	40 MHz
Sampling Freq. f_s (Disp. Est.)	120 MHz
Bayesian Likelihood Kernel Length	$3f_s/f_c$

of 0.495 in a 3D mesh extending 3.0 cm axially, 0.8 cm laterally, and 0.2 cm in elevation using LS-DYNA (Livermore Software Technology Corporation, Livermore, CA) [19]. The tracking was performed in Field II with a 10.4167 MHz tracking center frequency, pulse repetition frequency (PRF) of 20 kHz, and plane wave tracking [73, 74]. To ensure fully developed speckle, there were 1,300,000 scatterers/cm^3 and over 12 scatterers per resolution cell. The simulated RF data were filtered using a 4^{th}-order, high-pass Butterworth filter with a cutoff frequency of 8 kHz to account for a simulation artifact. The displacements were estimated using the Bayesian displacement estimator described in Section 2.2 [25], [26], [67], [68]. For each shear moduli simulated in the look-up table, we simulated 20 independent speckle realizations and averaged the time-to-peak displacement for each.

6.2.2 Homogeneous PVA Phantoms

Polyvinyl alcohol (PVA) is a material that has shown to be well suited for imaging applications, such as modeling vasculature, and is attractive for phantoms because it is nontoxic and the mechanical properties can be adjusted during construction [94]. PVA

is mixed as a cryogel and then frozen to maintain its form. By subjecting the PVA to additional freeze-thaw cycles, the PVA cross-links and becomes increasingly stiffer [94].

The PVA mixture was created by dissolving 17.5 g (7% weight) of PVA (molecular weight 89,000-98,000, 99% hydrolyzed, Sigma-Aldrich Inc., St. Louis, MO) into 250 mL of water and heated to 85°C. Then, 8% concentration by weight of graphite powder (General Pencil Company, Inc., Jersey City, NJ) was added for scattering. The mixture was poured into eight phantom molds and frozen for about 12 hours. After the phantoms were completely frozen, they were completely thawed at room temperature. This freeze-thaw cycle can be repeated to further stiffen the phantom. The phantoms underwent one freeze-thaw cycle.

We estimated the shear modulus in these homogeneous phantoms using a shear wave speed-derived estimate and the on-axis look-up table. We used a Verasonics Vantage 128 System (Verasonics Inc., Kirkland, WA) and the same push and tracking configurations as the simulated look-up table and the parameters are shown in Table 6.2. The displacements were estimated using the Bayesian displacement estimator and then motion filtered at each depth by subtracting a quadratic fitted to data outside of the ARF motion [75]. To measure the shear wave speed, we used a time-of-flight-based method and the random sample consensus (RANSAC) algorithm, which is robust in homogeneous tissue, and converted to shear modulus [33]. Before these homogeneous phantoms were sliced into thin layers, we computed five independent shear wave speeds at the depth that would be sliced and took the median. We also found the time-to-peak displacement at each depth and used the look-up table to estimate shear modulus.

6.2.3 Layered PVA Phantoms

We constructed layered phantom models by thinly slicing the homogeneous phantoms and laying them on top of a stiffer PVA phantom that underwent two freeze-thaw cycles. We cut the PVA using a mandoline food slicer and used slices of the phantoms from the

Table 6.2: CL15-7 phantom imaging parameters

Option	Parameter Value
Transducer	CL15-7
Push Center Freq.	8.9286 MHz
Excitation F/#	3
Excitation Focal Depth	1.1 cm
Push Duration	180 μs
Tracking Center Freq. (f_c)	10.4167 MHz
Tracking Pulse Repetition Freq. (PRF)	20 kHz
Receive F/#	1
Sampling Freq. (Acquired)	41.67 MHz
Sampling Freq. (f_s) (Disp. Est.)	125 MHz
Bayesian Likelihood Kernel Length	$3f_s/f_c$

focal depth location (1.1 cm). The layered phantoms had a top layer between 2.5-4 mm thick (1 freeze/thaw cycle) and a thicker, stiffer bottom layer (2 freeze/thaw cycles, shear moduli of 14.2$\pm$0.75 kPa). Figure 6.1 shows the experimental set-up using the CL15-7 transducer imaging through a 1 cm stand-off pad into the thin layer on top of a thicker, stiffer bottom phantom. A B-mode image of a layered phantom is shown on the right. After slicing and layering the phantoms, we imaged them using the parameters listed in Table 6.2 and plane wave tracking. The same acquisition sequence was used to generate the shear wave speed-derived estimate and the on-axis estimate for a direct comparison at the specific location and time. We estimated displacements using the Bayesian displacement estimator. We tested the on-axis method using the look-up table and compared it to shear wave speed-derived shear modulus estimates using the RANSAC algorithm. We took three acquisitions at slightly different locations in each of the eight phantoms and took the median to get our estimates. Two phantoms were omitted because the error was over 200% using both estimation methods. This may have been due to the imperfect slicing of the layers.

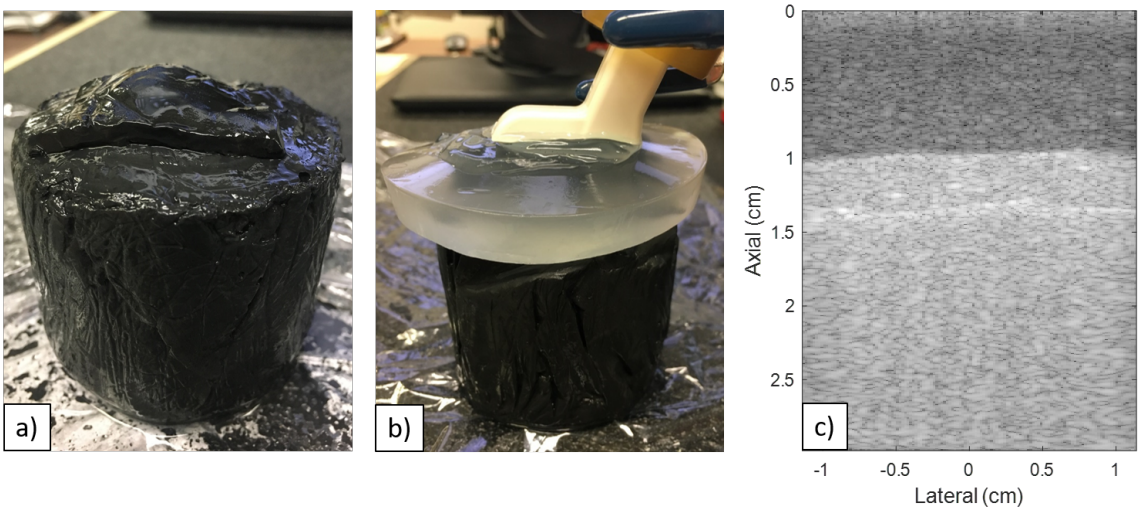

Figure 6.1: a) Layered PVA phantom with the top layer of PVA 1 freeze/thaw cycle and the bottom phantom of 2 freeze/thaw cycles. The layer was coupled with ultrasound gel. b) Experimental imaging set-up using a CL15-7 transducer. We used a 1 cm stand-off pad on top of the thin layered phantom and the thicker, stiffer phantom. We focused the ARF push at a 1.1 cm depth in the thin layer. c) B-mode image of a layered phantom. The layer is between 1-1.4 cm in depth.

6.2.4 Homogeneous Gelatin Phantoms

We also constructed layered tissue-mimicking phantoms made of different concentrations of gelatin to more finely vary the elasticity [86, 87, 88]. We mixed gelatin powder (Gelatin from porcine skin, 300 Bloom strength, Sigma-Aldrich Inc., St. Louis, MO) with degassed, deionized water and isopropyl alcohol to increase the sound speed. We stirred and heated the solution until the gelatin powder was dissolved and the solution turned clear. We also degassed the solution to further remove air bubbles. While it was still in liquid form, we stirred in 6% concentration by weight of graphite (General Pencil Company, Inc., Jersey City, NJ) for scattering properties. The solution was poured into phantom molds, securely sealed, and slowly rotated for about four hours until it cooled and congealed. We rotated the phantoms so that the graphite did not settle to bottom while congealing. The gels were then refrigerated overnight. By increasing the gelatin concentration, it increases the stiffness. We made three 6% gelatin, three 8% gelatin, and two 10% gelatin phantoms.

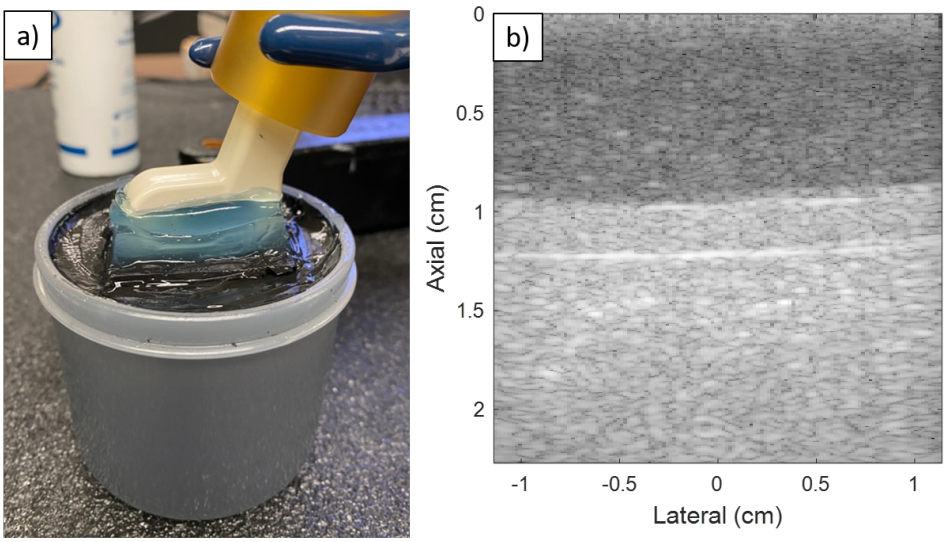

Figure 6.2: a) Experimental imaging set-up using a CL15-7 transducer and gelatin phantoms. We used a 1 cm stand-off pad on top of the thin layered gelatin phantom and the thicker, stiffer gelatin phantom. We focused the ARF push at a 1.1 cm depth in the thin layer. a) B-mode image of a layered gelatin phantom. The layer is between 1-1.25 cm in depth.

To quantify the elasticity of the material before slicing into layers, we measured the shear wave speed in the homogeneous phantoms using the random sample consensus (RANSAC) algorithm and converted to shear modulus [33]. We computed three independent shear wave speeds at the approximate depth that would be sliced and took the median to get that phantom's gold standard elasticity.

6.2.5 Layered Gelatin Phantoms

Layered gelatin phantoms were constructed similar to method of the PVA layered phantoms. In each of the eight homogeneous phantoms, we sliced two or three thin layers at a central location where the shear wave speed was captured. We cut the layers with a sharp knife using one continuous motion to reduce jagged edges. The gelatin layered phantoms had thicknesses of about 1-3.5 mm, which is slightly thinner than the PVA layers. We placed the layers on top of a larger homogeneous phantom (10% gelatin) and coupled them with ultrasound gel. Figure 6.2 shows the experimental set-up using the CL15-7 trans-

ducer imaging through a 1 cm stand-off pad into the thin layer on top of a thicker, stiffer homogeneous phantom. After slicing and layering the phantoms, we imaged them using the same push and tracking configurations modeled in the FEM simulations and described in Table 6.2. The same focused push and plane wave tracking sequence was used to generate the shear wave speed-derived estimate and the on-axis estimate simultaneously for a direct comparison at the specific location. Each homogeneous phantom resulted in two or three sliced layers and each layer had three acquisitions to acquire median shear wave speeds and on-axis measurements simultaneously. We estimated displacements using the Bayesian displacement estimator. We tested the on-axis method using the look-up table and compared it to shear wave speed-derived shear modulus estimates using the RANSAC algorithm. For the shear wave speed time-of-flight estimates, we cropped the data so that the axial range was between 0.99-1.2 cm and within the depth of the layer. We took three acquisitions at slightly different speckle regions in each of the 20 layered phantoms and took the median to get our estimates. The error was computed between the shear modulus estimates in the layers and the gold standard, the shear wave speed-derived shear modulus estimates taken from the pre-sliced, homogeneous region of the phantom.

6.3 Results

6.3.1 PVA Phantom Results

The pre-sliced homogeneous PVA phantoms had a mean shear wave speed-derived shear modulus of 5.46$\pm$1.06 kPa. The time-to-peak displacement results are shown in Figure 6.3 for all of the eight phantoms with three different speckle realizations for each in the dotted lines. The solid lines show the simulated look-up table described in Section 6.2.1 using an elevational focus of 1.5 cm. The on-axis time-to-peak displacement results are most accurate at the focal depth of 1.1 cm which is where we estimate a shear moduli from the look-up table. The on-axis method estimated the phantoms to have a mean shear

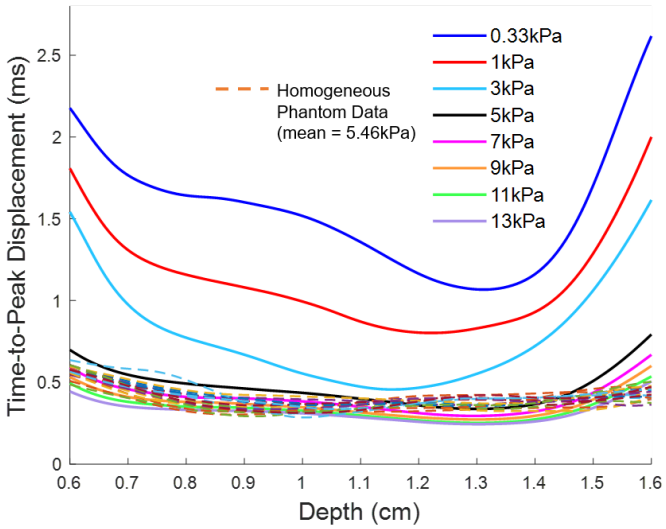

Figure 6.3: Homogeneous PVA phantom time-to-peak displacement curves (dotted lines) plotted on the Bayesian displacement-derived stiffness look-up table (solid lines). Using the RANSAC algorithm, they had a shear modulus of 5.46±1.06 kPa. The on-axis shear moduli are estimated at the focal depth of 1.1 cm.

moduli of 5.56±0.76 kPa.

Figure 6.4 shows the time-to-peak displacements for the layered phantoms. The dotted sections show the general locations of the stand-off pad, thin layer, and bottom layer. The time-to-peak displacement in the layer is consistent between the simulated look-up table and the gold standard shear modulus using the RANSAC algorithm that was measured before the phantom was sliced. The mean shear moduli for the on-axis method and shear wave speed-derived estimates in the layer were 5.92±1.15 kPa and 6.50±0.31 kPa, respectively.

Figure 6.5 shows the error in both methods compared to the gold standard using the RANSAC algorithm before the phantoms were sliced into layers (mean of 5.46±1.06 kPa). The shear wave speed-derived estimates had a bias of -1.04 kPa and the on-axis method had a bias of -0.46 kPa. This shows that the shear wave speed-derived estimates tend to overestimate the shear wave speed and stiffness in the thin layer more than the on-axis method.

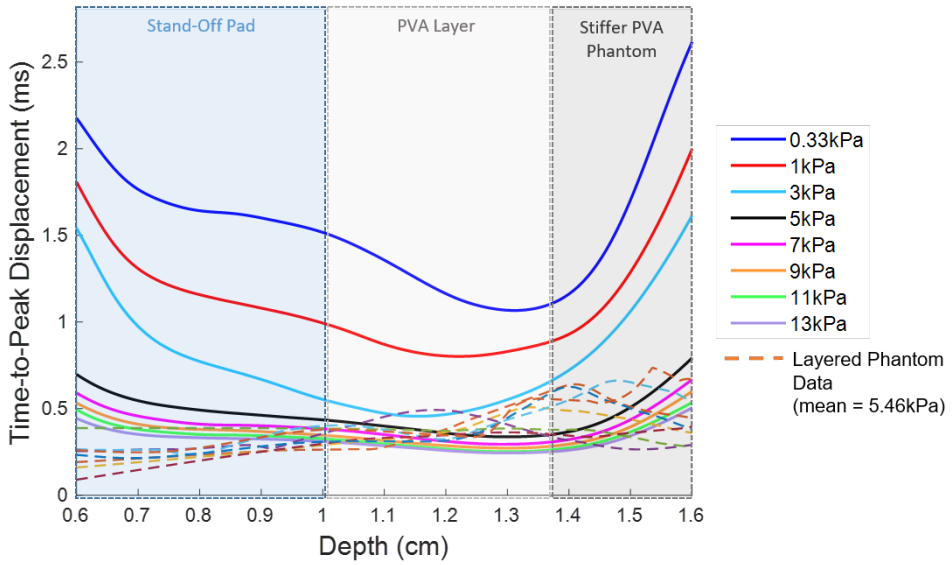

Figure 6.4: Layered PVA phantom time-to-peak displacement curves (dotted lines) plotted on the Bayesian displacement-derived stiffness look-up table (solid lines). Using the RANSAC algorithm before the phantoms were sliced, they had a shear modulus of 5.46±1.06 kPa. The on-axis shear moduli are estimated at the focal depth of 1.1 cm.

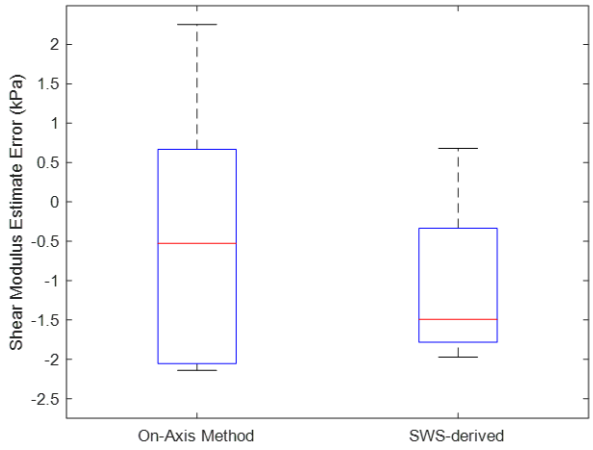

Figure 6.5: Error in shear modulus estimates of thin layered PVA phantoms. The error is computed between the shear wave speed-derived estimate before the phantom was sliced and after they were sliced by either the on-axis look-up table method or the shear wave speed-derived method using the RANSAC algorithm. The on-axis method has a larger variance, but a smaller bias than the shear wave speed-derived estimates.

Table 6.3: Homogeneous gelatin phantom shear wave speed-derived shear moduli

	Mean (kPa)	St. Deviation (kPa)
6% Gelatin		
1	4.66	0.06
2	2.77	0.02
3	5.55	0.03
8% Gelatin		
4	6.83	0.44
5	7.03	0.02
6	13.7	0.19
10% Gelatin		
7	8.37	0.09
8	21.8	0.24

6.3.2 Gelatin Phantom Results

The pre-sliced homogeneous gelatin phantoms each had robust shear wave speed measurements using the RANSAC algorithm. Within each gelatin concentration batch, the phantoms had a larger range of elasticity, possibly due to warming or lacking a preservative. The shear wave speed-derived shear moduli are shown in Table 6.3.

For the layered gelatin phantom shear modulus estimates, we first used the look-up table described in Section 6.2.1 that modeled the elevational focus of the CL15-7 transducer as 1.5 mm. This look-up table was also used in the PVA phantom experiments. Figure 6.6 shows the time-to-peak displacements through depth for each layered gelatin phantom acquisition. Each of the eight plots represent results from the layers sliced from corresponding homogeneous phantom listed in Table 6.3 and described above each plot with the gold standard elasticity estimate derived from the shear wave speed in the homogeneous region. The solid lines show the simulated look-up table and the dotted lines are each layered phantom's on-axis time-to-peak displacement. Each subplot of Figure 6.6 shows results for two or three sliced layers with three acquisitions each.

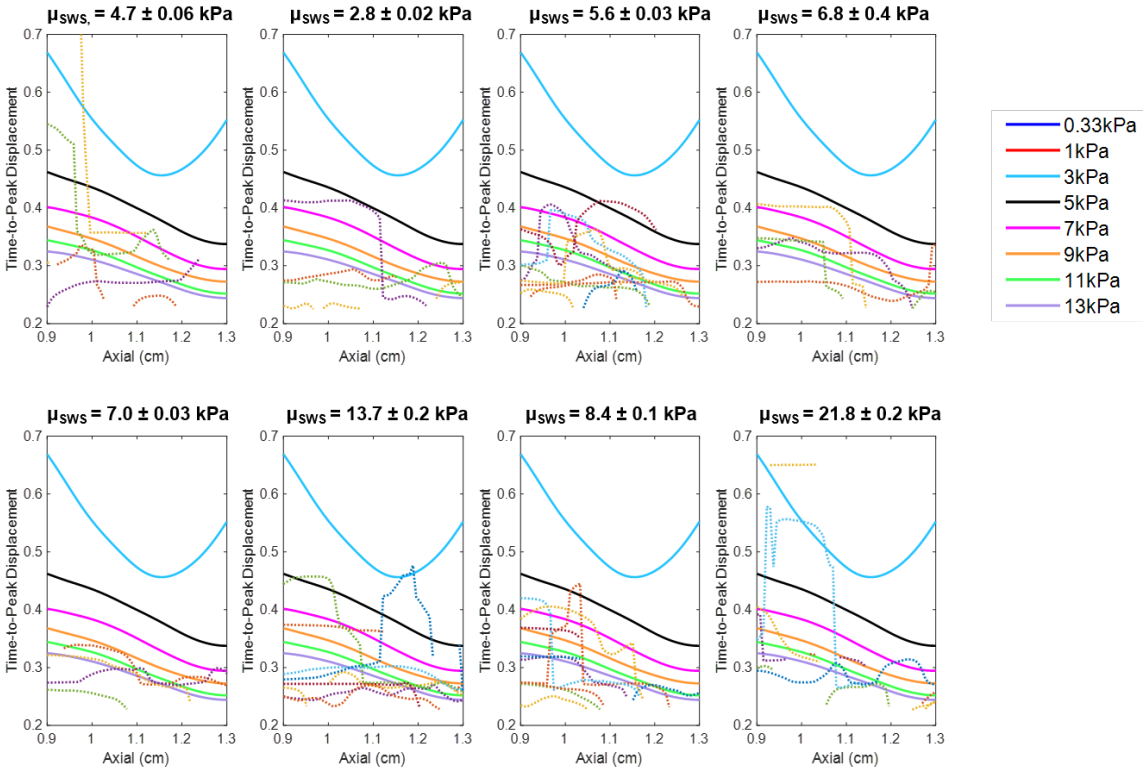

Figure 6.6: Layered gelatin phantom time-to-peak displacement curves (dotted lines) plotted on the Bayesian displacement-derived stiffness look-up table (solid lines) modeling a CL15-7 with an elevational focus of 1.5 cm. The elasticity of each pre-sliced homogeneous phantom that the layers are cut from is in the title of each subplot. The ARF focal depth is 1.1 cm and the layers are approximately located between 1-1.3 mm. The on-axis estimates are taken at 0.99-1.2 cm in depth.

In the results shown in Figure 6.6 using a 1.5 cm elevational focus for the transducer, we observed a large bias and a simulation mismatch. The on-axis elasticity measurements are taken around the focal depth location of 1.1 cm. Many of these time-to-peak displacements fall outside of the simulated look-up table resulting in elasticity estimates that are over 100% error in the soft phantoms. We simulated another look-up table changing the elevational focus of the CL15-7 to 1.1 cm, the location of the push focus. The same time-to-peak displacement results are shown in Figure 6.7 with the new look-up table with the transducer's elevational focus modeled as 1.1 cm. This look-up table has a more consistent time-to-peak displacement across the focal depth that is observed in the experiments. The experimental time-to-peak displacement results match better with the 1.1 cm elevational focus look-up table and there is a large reduction in bias. These results are shown next in the error analysis.

Figure 6.8 shows the layered gelatin phantom shear modulus estimates. Each subplot represents the eight homogeneous phantoms labeled in the top left corner. The black solid line represents the shear wave speed-derived elasticity measured in the pre-sliced homogeneous region. The blue dotted lines represent the on-axis simulated look-up table shear modulus estimates for each layered phantom acquisition. The red dashed lines represent the shear wave speed-derived shear modulus estimates in the layered phantoms. The shear wave speed is measured at lateral locations within the axial range of 0.99-1.2 cm and we show it here as a constant value to compare to the on-axis results. The y-axis was limited to 25 kPa, but some shear wave speed (SWS)-derived estimates had high error and are not seen below 25 kPa. Phantom #4 had a SWS-derived shear modulus estimate of 145 kPa, phantom #5 had six SWS-derived estimates between 80-420 kPa and phantom #7 had one SWS-derived estimate of 52 kPa. The on-axis shear modulus estimates of this particular imaging set-up and parameters have a fundamental limit of the elasticity that can be measured based the time of the first tracking acquisition. This limit can be seen around 10-15 kPa where we do not resolve time-to-peak estimates because the peak occurred at or before

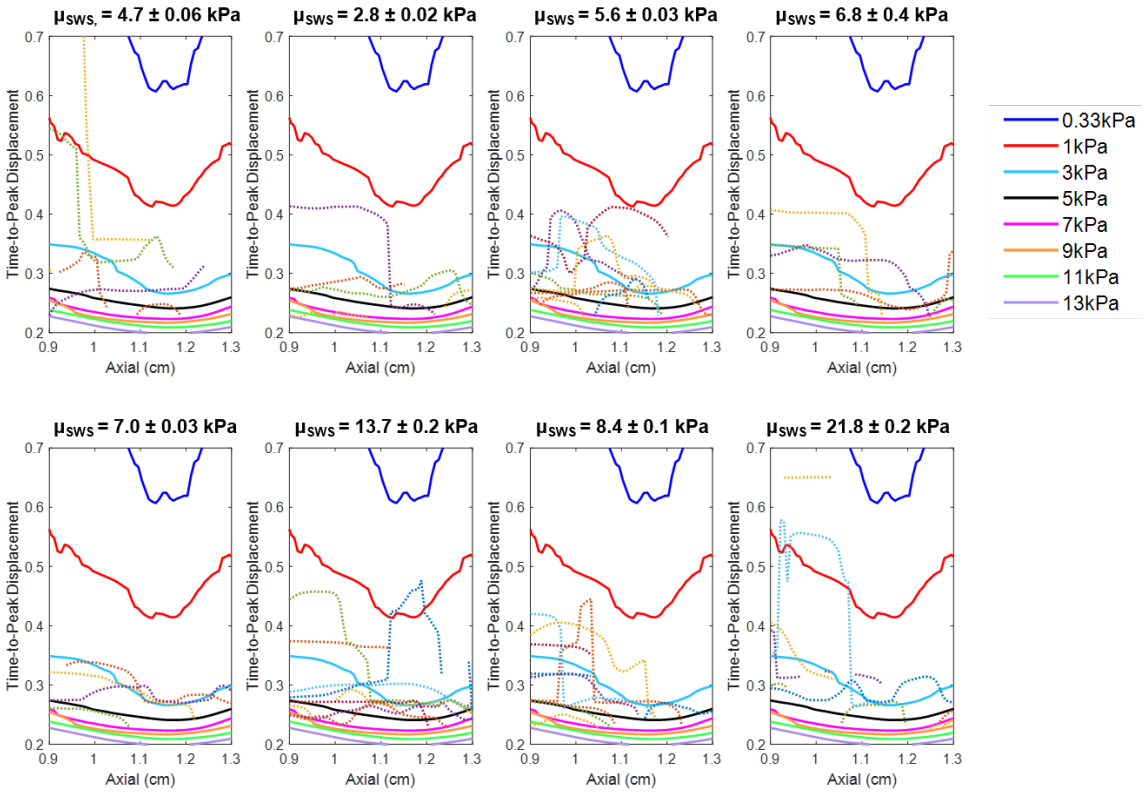

Figure 6.7: Layered gelatin phantom time-to-peak displacement curves (dotted lines) plotted on the Bayesian displacement-derived stiffness look-up table (solid lines) modeling a CL15-7 with an elevational focus of 1.1 cm (changed from 1.5 cm previously). The elasticity of each pre-sliced homogeneous phantom that the layers are cut from is in the title of each subplot. The ARF focal depth is 1.1 cm and the layers are approximately located between 1-1.3 cm. The on-axis estimates are taken at 0.99-1.2 cm in depth.

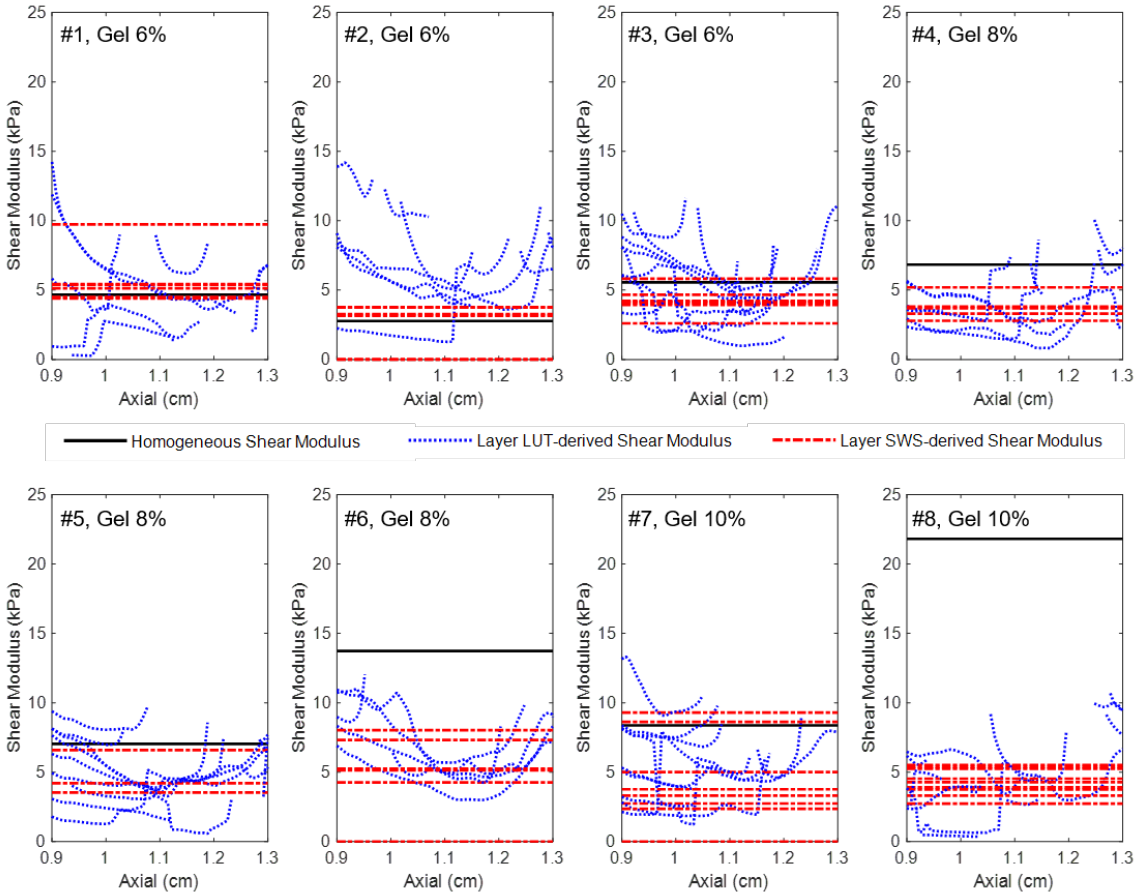

Figure 6.8: Layered gelatin phantom shear modulus estimates. The black lines show the gold standard shear moduli for each phantom measured in the pre-sliced homogeneous regions. The blue dotted lines show the on-axis look-up table derived shear modulus estimates for each acquisition in the layered phantoms and the red dashed lines show the shear wave speed-derived shear modulus estimates in each layer.

the first time step.

Table 6.4 show the shear modulus estimate results for the layered gelatin phantoms using the on-axis method or the shear wave speed-derived method. The shear modulus results were taken as a median of three shear modulus estimates in each method for each 20 layered phantoms, then reported as a mean and standard deviation for each batch of layers numbered 1-8. In both the on-axis method and in shear wave speed-derived shear moduli, the root mean square error (RMSE) tends to increase with increasing stiffness. The shear wave speed-derived estimates have lower RMS error than the on-axis method in the

Table 6.4: Layered gelatin phantom shear modulus estimates and errors for both on-axis estimates and shear wave speed-derived estimates measured within the gelatin layers (all shown in kPa). Error in both methods are measured against the shear wave speed-derived estimates from the homogeneous phantoms.

	On-Axis FEM-based Results				SWS-derived Results			
	Mean	St. Dev.	RMSE	Bias	Mean	St. Dev.	RMSE	Bias
6% Gel.								
1	4.0	2.5	1.9	0.62	4.9	0.63	0.52	-0.28
2	5.4	1.0	2.7	-2.6	3.4	0.41	0.74	-0.68
3	4.6	1.7	1.6	0.80	4.3	0.32	1.3	1.3
8% Gel.								
4	3.2	1.1	3.7	3.7	3.6	0.35	3.3	3.3
5	4.6	2.3	3.1	2.5	120	110	145	-114
6	5.6	0.8	8.2	8.1	5.8	2.2	8.1	7.9
10% Gel.								
7	4.8	2.3	4.0	3.6	4.9	3.3	4.4	3.5
8	3.1	2.2	19	19	4.2	0.32	18	18

successfully measured softer phantoms, but has potential to fail badly as seen in phantom batch #5. The on-axis method and the shear wave speed-derived estimates have similar amounts of bias across the phantoms. These results are also shown in Figure 6.9 using a boxplot for each phantom.

6.4 Discussion

The on-axis stiffness estimation technique using a simulated stiffness look-up table was applied to estimate shear modulus in thin, layered phantoms. We compared the on-axis look-up table method to shear wave speed-derived shear moduli. The two elasticity methods had similar performance in the layered phantoms. The on-axis method had a larger variance in shear modulus estimates than shear wave speed-derived estimates. The layered PVA phantoms showed a reduced bias using the on-axis method. In the layered gelatin phantoms, the shear wave speed-derived estimates had lower root mean square error, but

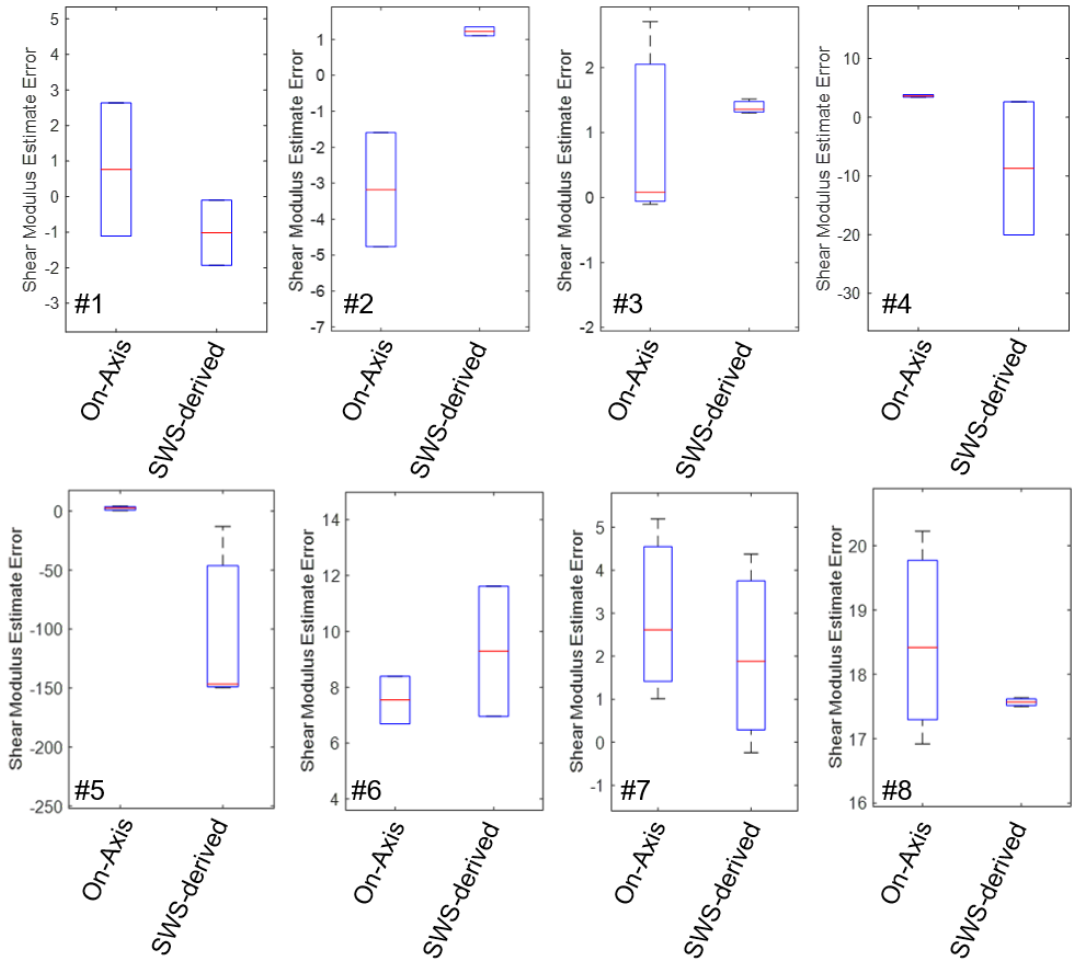

Figure 6.9: Each layered gelatin phantom on-axis and shear wave speed (SWS)-derived shear modulus estimate error. Error in both methods are measured against the shear wave speed-derived estimates from the homogeneous phantoms.

had more outliers that persisted in the results even after taking the median of three shear modulus estimates. The two methods had similar bias results across the gelatin layered phantoms. Both the shear wave speed and the on-axis method failed in the stiffer phantoms #6 and #8. These results show potential to quantify skin elasticity at the acoustic radiation force push location and comparable performance as shear wave speed-derived methods.

The on-axis method using this particular transducer and imaging sequence for the look-up table had a fundamental limit around 10 kPa at the focal depth. This can be limited by several parameters, including the imaging depth and the highest achievable pulse repetition frequency to capture consecutive RF lines. The acoustic radiation force also causes high signal decorrelation after it is applied that can corrupt the signals captured closely after the push. A shorter push pulse may be better suited for this task rather than a longer pulse typically used to increase SNR. The parameters selected to model the transducer's imaging configuration can affect this as well. We have observed changes in the time-to-peak on-axis displacement profiles when changing acquisition parameters, such as F/# and elevational focus. We saw better performance when matching the location of the modeled elevational focus in the look-up table to the focal depth of the push. However, further work could be done to evaluate the true elevational focus of the transducer. Also, pushing at the manufactured elevational focus may give a higher displacement SNR that could be advantageous.

The phantom materials and construction can also be a source of variation. The PVA and gelatin may have different acoustic properties that can lead to model mismatch. There could be changes in attenuation, sound speed, or inhomogeneities. Also, the gelatin phantoms were not constructed using a hardener or added preservative. Therefore, the phantoms may have been warming if they were not fully at room temperature which could lead to elasticity differences and bias in consecutive acquisitions of the layer. Some of the gelatin phantom may have had longer refrigeration time that can also increase the stiffness within the batch of the same gelatin concentration. However, the gold standard acquisitions in the

homogeneous phantoms were imaged immediately before slicing and imaging the layers. Additionally, the thickness of the layers varied between slices. This could affect the range that both measurements average across, as well as lead to bias. Also, the act of slicing the material could lead to softening or fractures that can contribute to error.

The mechanical validation of quantitative skin measurements is difficult *ex vivo*. Excised tissue can have structural changes and dehydration that change the mechanical properties. The method in this chapter can be used to validate elasticity methods by providing a way of capturing a gold standard in a homogeneous region. This could help validate elasticity methods used in the skin instead of relying on a shear wave speed to compare between patient to patient that could have different bias behavior in different tissues. We were able to get quantitative on-axis stiffness estimates in thin layered soft phantoms similar to shear wave speed-derived estimates. Both shear wave speed and on-axis methods failed in stiffer layered phantoms, but further work can be done to optimize imaging parameter to image stiffer tissues using the on-axis method.

6.5 Conclusion

The methods used to create skin-mimicking PVA and gelatin phantoms can be used to validate quantitative elasticity imaging in thin layers. The results show that we can get shear modulus estimates close to the value of the pre-sliced shear wave speed-derived estimates in soft phantoms. The on-axis method performs similarly to the shear wave speed derived stiffness estimate. The on-axis method has a larger variance, but a smaller bias than the shear wave speed-derived estimates in the PVA layered phantoms and similar bias in the gelatin phantoms. These preliminary results show ability to quantify on-axis elasticity in layered media.

Chapter 7

Conclusions and Future Work

This dissertation developed an ARF-based elasticity technique that measures on-axis displacement rather than lateral shear wave speed to attempt to reduce the effects of a complicated shear wave propagation in the skin. The clinical motivation of this work is to improve quantitative elasticity in post-treatment head and neck cancer patients developing secondary lymphedema and fibrosis. As previously described, elasticity imaging in the skin has been difficult due to the skin's thin nature and complicated surrounding structures, including subcutaneous fat, muscle, and bone [40, 41]. Acoustic radiation force (ARF)-based elasticity imaging can provide stiffness information that is less operator dependent and also allows us to image deeper muscle regions that may be affected by fibrosis and lymphedema that could not as easily be quantified using a surface technique or palpitation [5, 13]. Shear wave speed methods in the skin have shown to be biased based on the skin thickness and can corrupt the shear wave speed measurements [41]. Some groups attempt to offset this layer-dependent bias by normalizing the shear wave speed measurements by the width of the skin layer, but they still rely on measuring the velocity of a complex shear wave and do not have an analytical model to convert to shear modulus [41, 61, 62]. There is still a significant gap in the field for validating ultrasound elastography in skin [95]. To get accurate measurements of elasticity from patient to patient, there needs to be an improved quantitative measurement technique. The impact of improving skin elasticity imaging would be early detection of fibrosis that may not be noticed in a physical examination of the skin and ability to compare quantitative stiffness across different patients. This could improve patients' quality of life, symptom management, and survival by informing the need for therapy before fibrosis progression.

We demonstrated a method to use a simulated stiffness look-up table for on-axis acous-

tic radiation force-based elasticity estimation. We have shown the on-axis method coupled with a Bayesian displacement estimator produces stiffness estimates comparable to laterally offset shear wave methods and we can apply a simulated look-up table to real experimental data. We have shown that we can produce quantitative stiffness estimates at the acoustic radiation force location in phantoms of different elasticities and have validated the technique in homogeneous simulations and phantoms. We have also tested the on-axis method in simulations of different attenuation, signal-to-noise ratio, and sound speed to show the importance of selection of realistic parameters for the simulation model.

In addition to the development of the on-axis elasticity method, we have made improvements in optimizing the advanced Bayesian displacement estimator to greatly improve run time. This dissertation work shows the importance of an advanced displacement estimator, such as the Bayesian displacement estimator, when measuring displacement at the acoustic radiation force location. The addition of Bayesian displacement estimator allows us to reduce displacement estimation variance enough to achieve on-axis elasticity estimates comparable to shear wave speed-derived estimates. Therefore, the Bayesian displacement estimator is an important aspect of this work. We made large improvements in reducing the run time by two orders of magnitude by supplying an optimizing solver function with the analytical gradient. There is also improvement in reducing computational cost by solving for a Hessian matrix and implementing Newton's method. The Bayesian displacement estimator can be solved using full Newton's method with the gradient and Hessian. Additionally, a Bayesian likelihood solution can be reached faster than a normalized cross-correlation solution using Newton's method.

The faster solution of the Bayesian displacement equation can be applied broadly in the field of elasticity imaging in ultrasound and is more likely to be adopted for displacement estimation. We plan to publish the code to make it available for other groups to easily implement our method. Additionally, there is the ability to tailor the Bayesian equation to solve for the only the likelihood function to achieve fast, high quality displacement imag-

ing. In this work, we mainly show displacement at the region of excitation which is quite challenging to estimate already. However, normalized cross-correlation is commonly used as one of the best unbiased displacement estimators and reaching a likelihood solution in less time than normalized cross-correlation is an exciting result. This method also allows us to tailor the amount of regularization of the prior function to reduce the computational time of a regularized solution. There is potential to code these methods faster in different programming languages and further optimize the code. Also, this method could be improved by automatically choosing a step size. Further exploration into other optimization routines has not been explored, but the first and second-order derivative solutions of the Bayesian displacement equation that we have solved for can be applied to many other optimization algorithms.

This dissertation also presented a method to create skin-mimicking polyvinyl alcohol (PVA) and gelatin phantoms that can be used to validate quantitative elasticity imaging in thin layers. The results show that we can get shear modulus estimates close to the value of the pre-sliced shear wave speed-derived estimates in soft phantoms and the on-axis method performs similarly to the shear wave speed-derived stiffness estimate. The on-axis method has a larger variance, but a smaller bias than the shear wave speed-derived estimates in the PVA layered phantoms and similar bias in the gelatin phantoms. In the future, using a preservative in the gelatin phantoms could help improve the structural stability and reduce variance. These preliminary results show ability to quantify on-axis elasticity in layered media, but there is a lot of future work to be done to further validate elasticity in thin layers.

We have demonstrated results in layered phantoms using two types of simulated look-up tables. Future work includes optimizing the simulation and imaging parameters to increase the stiffness it can measure, or measure faster time-to-peak displacement. This has been optimized for the homogeneous phantoms set-ups in this dissertation, but further analysis needs to be done to characterize the changes in measureable time-to-peak displacement

in the layered phantoms. Next, we can model the look-up tables and perform imaging studies in layers to determine the model we want to use. The look-up tables and imaging sequences used in this work were optimized to achieve the highest displacement SNR in homogeneous material, but this may not be the best approach for layered phantoms. We can achieve good displacements at low SNRs with the Bayesian displacement estimator [68]. Instead, we should optimize for a sequence that has the lowest push decorrelation and highest measureable time-to-peak displacement for a particular pushing configuration. In the homogeneous phantoms, we performed F/# studies to have a larger axial region of displacement to average over. Then, we observed displacements in the layers using these pushing sequences, but another F/# study should be performed to determine the best simulation model to match thin layers. A tighter axial focus could be better in the layers. Other future studies in the layered phantoms include testing the receive F/#, comparing plane wave and focused tracking schemes, further increasing pulse repetition frequency by limiting depth, and changing the elevational focus. Then, this method should be further validated in stiffer layered phantoms to reach a range of elasticity found in human skin.

The simulated look-up table also makes some assumptions about how the acoustic radiation force (Equation 1.3) generates displacements. This could be further studied because we do not model the entire complex process of momentum transfer of the acoustic radiation force into the tissue. We typically subtract the push duration time being applied and start tracking at time zero to mimic the simulation. However, this could be studied further to determine if there are changes in how the force transfers into tissue of different properties. Other assumptions about the tissue being imaged need to be considered when generating the stiffness look-up table such as attenuation, sound speed, and perhaps viscosity. Additionally, because we are imaging thin layers, we can test modeling the layers into the finite element models or making a layered look-up table model. This presents another variable of measuring and modeling the skin thickness, but it could provide more insight in the best parameter selection or be an improvement to the look-up table. We could also segment the

B-mode images to determine the thickness for the model.

The on-axis elasticity method was developed with the goal of improving quantitative skin elasticity imaging. This method has potential to be applied in other areas of elasticity imaging as well, such as cervical elastography in pregnancy, determatology applications, muscular imaging, or anywhere a quantitative elasticity estimate could be clinically useful. This on-axis method could also be implemented in the future on a single element probe rather than a typical array-based transducer which could allow cheaper elasticity measurements without needing a more expensive clinical scanner.

BIBLIOGRAPHY

[1] Martin E Anderson and Gregg E Trahey. A seminar on k-space applied to medical ultrasound. *Department of Biomedical Engineering, Duke University*, 2000.

[2] Richard SC Cobbold. *Foundations of biomedical ultrasound*. Oxford university press, 2006.

[3] Michael F Insana and David G Brown. Acoustic scattering theory applied to soft biological tissues. *Ultrasonic scattering in biological tissues*, pages 75–124, 1993.

[4] Mark L. Palmeri. Elasticity imaging: Methods and applications. Short Course at IEEE Int. Ultrason. Symp. (IUS) 2015, October 2015.

[5] Joshua R Doherty, Gregg E Trahey, Kathryn R Nightingale, and Mark L Palmeri. Acoustic radiation force elasticity imaging in diagnostic ultrasound. *IEEE Trans. Ultrason., Ferroelectr., Freq. Control*, 60(4):685–701, Apr. 2013.

[6] W. Michael Lai, David Rubin, and Erhard Krempl. *Introduction to Continuum Mechanics*. Butterworth-Heinmann, Burlington, MA, 4 edition, 2010.

[7] Jonathan Ophir, Ignacio Cespedes, Hari Ponnekanti, Youseph Yazdi, and Xin Li. Elastography: a quantitative method for imaging the elasticity of biological tissues. *Ultrasonic imaging*, 13(2):111–134, 1991.

[8] Matthew O'Donnell, Andrei R Skovoroda, Benjamin M Shapo, and Stanislav Y Emelianov. Internal displacement and strain imaging using ultrasonic speckle tracking. *IEEE transactions on ultrasonics, ferroelectrics, and frequency control*, 41(3):314–325, 1994.

[9] KJ Parker, SR Huang, RA Musulin, and RM Lerner. Tissue response to mechanical

vibrations for sonoelasticity imaging. *Ultrasound in medicine & biology*, 16(3):241–246, 1990.

[10] Laurent Sandrin, Mickaël Tanter, J-L Gennisson, Stefan Catheline, and Mathias Fink. Shear elasticity probe for soft tissues with 1-d transient elastography. *IEEE transactions on ultrasonics, ferroelectrics, and frequency control*, 49(4):436–446, 2002.

[11] Laurent Sandrin, Bertrand Fourquet, Jean-Michel Hasquenoph, Sylvain Yon, Céline Fournier, Frédéric Mal, Christos Christidis, Marianne Ziol, Bruno Poulet, Farad Kazemi, et al. Transient elastography: a new noninvasive method for assessment of hepatic fibrosis. *Ultrasound in medicine & biology*, 29(12):1705–1713, 2003.

[12] James F Greenleaf, Mostafa Fatemi, and Michael Insana. Selected methods for imaging elastic properties of biological tissues. *Annual review of biomedical engineering*, 5(1):57–78, 2003.

[13] Kathy R. Nightingale. Acoustic radiation force impulse (arfi) imaging: a review. *Curr. Med. Imag. Rev.*, 7(4):328–339, Nov. 2011.

[14] Kathryn Nightingale, Mary Scott Soo, Roger Nightingale, and Gregg Trahey. Acoustic radiation force impulse imaging: in vivo demonstration of clinical feasibility. *Ultrasound in medicine & biology*, 28(2):227–235, 2002.

[15] A. P. Sarvazyan, O. V. Rudenko, S. D. Swanson, J. B. Fowlkes, and S. Y. Emelianov. Shear wave elasticity imaging: a new ultrasonic technology of medical diagnostics. *Ultrasound Med. Biol.*, 24(9):1419–1435, Dec. 1998.

[16] Jérémy Bercoff, Mickaël Tanter, and Mathias Fink. Supersonic shear imaging: a new technique for soft tissue elasticity mapping. *IEEE Trans. Ultrason., Ferroelectr., Freq. Control*, 51(4):396–409, Apr. 2004.

[17] G. R. Torr. The acoustic radiation force. *Am. J. of Phys.*, 52(5):402–408, May 1984.

[18] Kevin J Parker. Ultrasonic attenuation and absorption in liver tissue. *Ultrasound Med. Biol.*, 9(4):363–369, Jul.-Aug. 1983.

[19] Mark L. Palmeri, Amy C. Sharma, Richard R. Bouchard, Roger W. Nightingale, and Kathryn R. Nightingale. A finite-element method model of soft tissue response to impulsive acoustic radiation force. *IEEE Trans. Ultrason., Ferroelectr., Freq. Control*, 52(10):1699–1712, Oct. 2005.

[20] Francesco Viola and William F Walker. A comparison of the performance of time-delay estimators in medical ultrasound. *IEEE Trans. Ultrason., Ferroelectr., Freq. Control*, 50(4):392–401, Apr. 2003.

[21] Gianmarco F. Pinton, Jeremy J. Dahl, and Gregg E. Trahey. Rapid tracking of small displacements with ultrasound. *IEEE Trans. Ultrason., Ferroelectr., Freq. Control*, 53(6):1103–1117, Jun. 2006.

[22] Chihiro Kasai, Koroku Namekawa, Akira Koyano, and Ryozo Omoto. Real-time two-dimensional blood flow imaging using an autocorrelation technique. *IEEE Transactions on sonics and ultrasonics*, 32(3):458–464, 1985.

[23] Thanasis Loupas, JT Powers, and Robert W Gill. An axial velocity estimator for ultrasound blood flow imaging, based on a full evaluation of the doppler equation by means of a two-dimensional autocorrelation approach. *IEEE transactions on ultrasonics, ferroelectrics, and frequency control*, 42(4):672–688, 1995.

[24] William F Walker and Gregg E Trahey. A fundamental limit on delay estimation using partially correlated speckle signals. *IEEE Trans. Ultrason., Ferroelectr., Freq. Control*, 42(2):301–308, Mar. 1995.

[25] Brett C. Byram, Gregg E. Trahey, and Mark L. Palmeri. Bayesian speckle tracking. part i: an implementable perturbation to the likelihood function for ultrasound dis-

placement estimation. *IEEE Trans. Ultrason., Ferroelectr., Freq. Control*, 60(1):132–143, Jan 2013.

[26] Brett C. Byram, Gregg E. Trahey, and Mark L. Palmeri. Bayesian speckle tracking. part ii: biased ultrasound displacement estimation. *IEEE Trans. Ultrason., Ferroelectr., Freq. Control*, 60(1):144–157, Jan 2013.

[27] B J Fahey, S J Hsu, P D Wolf, R C Nelson, and G E Trahey. Liver ablation guidance with acoustic radiation force impulse imaging: challenges and opportunities. *Phys. Med. Biol.*, 51(15):3785–3808, Jul. 2006.

[28] Stephanie A Eyerly, Maryam Vejdani-Jahromi, Douglas M Dumont, Gregg E Trahey, and Patrick D Wolf. The evolution of tissue stiffness at radiofrequency ablation sites during lesion formation and in the peri-ablation period. *J. Cardiovasc. Electrophysiol.*, 26(9):1009–1018, Sept. 2015.

[29] Douglas M. Dumont, Russell H Behler, Timothy C Nichols, Elizabeth P Merricks, and Caterina M Gallippi. Arfi imaging for noninvasive material characterization of atherosclerosis. *Ultrasound Med. Biol.*, 32(11):1703–1711, Nov. 2006.

[30] Tomasz J Czernuszewicz, Jonathon W Homeister, Melissa C Caughey, Mark A Farber, Joseph J Fulton, Peter F Ford, William A Marston, Raghuveer Vallabhaneni, Timothy C Nichols, and Caterina M Gallippi. Non-invasive in vivo characterization of human carotid plaques with acoustic radiation force impulse ultrasound: Comparison with histology after endarterectomy. *Ultrasound Med. Biol.*, 41(3):685–697, Mar. 2015.

[31] Kathryn R. Nightingale, Stephen A. McAleavey, and Gregg E. Trahey. Shear-wave generation using acoustic radiation force: in vivo and ex vivo results. *Ultrasound Med. Biol.*, 29(12):1715–1723, Dec. 2003.

[32] M. L. Palmeri, M. H. Wang, J. J. Dahl, K. D. Frinkley, and K. R. Nightingale. Quantifying hepatic shear modulus in vivo using acoustic radiation force. *Ultrasound Med. Biol.*, 34(4):546–558, Apr. 2008.

[33] Michael H Wang, Mark L Palmeri, Veronica M Rotemberg, Ned C Rouze, and Kathryn R Nightingale. Improving the robustness of time-of-flight based shear wave speed reconstruction methods using ransac in human liver in vivo. *Ultrasound Med. Biol.*, 36(5):802–813, May 2010.

[34] Ned C Rouze, Michael H Wang, Mark L Palmeri, and Kathryn R Nightingale. Parameters affecting the resolution and accuracy of 2-d quantitative shear wave images. *IEEE Trans. Ultrason., Ferroelectr., Freq. Control*, 59(8):1729–1740, Aug. 2012.

[35] Roee S. Lazebnik. *Tissue Strain Analytics: Virtual Touch Tissue Imaging and Quantification*. Siemens Medical Solutions USA, Inc., Mountain View, CA USA, 2008.

[36] Mark L Palmeri, Michael H Wang, Ned C Rouze, Manal F Abdelmalek, Cynthia D Guy, Barry Moser, Anna Mae Diehl, and Kathryn R Nightingale. Noninvasive evaluation of hepatic fibrosis using acoustic radiation force-based shear stiffness in patients with nonalcoholic fatty liver disease. *J. Hepatol.*, 55(3):666–672, Sept. 2011.

[37] Timothy J Hall, Andy Milkowski, Brian Garra, Paul Carson, Mark Palmeri, Kathy Nightingale, Ted Lynch, Abdullah Alturki, Michael Andre, Stephane Audiere, J. Bamber, R. Barr, J. Bercoff, J. Bercoff, M. Bernal, J. Brum, H. W. Chan, S. Chen, C. Cohen-Bacrie, M. Couade, A. Daniels, R. DeWall, J. Dillman, R. Ehman, S. F. Franchi-Abella, J. Fromageau, J.-L. Gennisson, J. P. Henry, N. Ivancevich, J. Kalin, S. Kohn, J. Kugel, K. Lee, N. L. Liu, T. Loupas, J. Mazernik, S. McAleavey, V. Miette, S. Metz, B. M. Morel, T. Nelson, E. Nordberg, J. Oudry, M. Padwal, N. Rouze, A. Samir, L. Sandrin, J. Schaccitti, C. Schmitt, V. Shamdasani, P. Song, P. Switalski, M. Wang, K. Wear, H. Xie, and H. Zhao. Rsna/qiba: Shear wave speed as a biomarker

for liver fibrosis staging. In *Proc. IEEE Int. Ultrason. Symp. (IUS)*, pages 397–400, Jul. 2013.

[38] F Sebag, J Vaillant-Lombard, J Berbis, V Griset, JF Henry, Pet al Petit, and C Oliver. Shear wave elastography: a new ultrasound imaging mode for the differential diagnosis of benign and malignant thyroid nodules. *The Journal of Clinical Endocrinology & Metabolism*, 95(12):5281–5288, 2010.

[39] Kemal Arda, Nazan Ciledag, Elif Aktas, Bilgin Kadri Aribas, and Kenan Köse. Quantitative assessment of normal soft-tissue elasticity using shear-wave ultrasound elastography. *AJR-American Journal of Roentgenology*, 197(3):532, 2011.

[40] Christopher Edwards and Ronald Marks. Evaluation of biomechanical properties of human skin. *Clinics in dermatology*, 13(4):375–380, 1995.

[41] Seung Yun Lee, Adela R Cardones, Joshua Doherty, Kathryn Nightingale, and Mark Palmeri. Preliminary results on the feasibility of using arfi/swei to assess cutaneous sclerotic diseases. *Ultrasound in medicine & biology*, 41(11):2806–2819, 2015.

[42] C Pailler-Mattei, S Bec, and H Zahouani. In vivo measurements of the elastic mechanical properties of human skin by indentation tests. *Medical engineering & physics*, 30(5):599–606, 2008.

[43] World Cancer Research Fund International. Cancer trends- worldwide cancer data. https://www.wcrf.org/cancer-trends/worldwide-cancer-data/, 2022.

[44] Jie Deng, Mary S Dietrich, Sheila H Ridner, Arthur C Fleischer, Nancy Wells, and Barbara A Murphy. Preliminary evaluation of reliability and validity of head and neck external lymphedema and fibrosis assessment criteria. *European Journal of Oncology Nursing*, 22:63–70, 2016.

[45] American Society of Clinical Oncology (ASCO). Head and neck cancer. http://www.cancer.net/cancer-types/head-and-neck-cancer/introduction, 2016.

[46] Anil K Chaturvedi, Eric A Engels, Ruth M Pfeiffer, Brenda Y Hernandez, Weihong Xiao, Esther Kim, Bo Jiang, Marc T Goodman, Maria Sibug-Saber, Wendy Cozen, et al. Human papillomavirus and rising oropharyngeal cancer incidence in the united states. *Journal of clinical oncology*, 29(32):4294, 2011.

[47] Jie Deng, Sheila H Ridner, Nancy Wells, Mary S Dietrich, and Barbara A Murphy. Development and preliminary testing of head and neck cancer related external lymphedema and fibrosis assessment criteria. *European Journal of Oncology Nursing*, 19(1):75–80, 2015.

[48] Barbara A Murphy et al. Lymphedema in patients with head and neck cancer. In *Oncology nursing forum*, volume 38, page E1. Oncology Nursing Society, 2011.

[49] Katarzyna Hojan and Piotr Milecki. Opportunities for rehabilitation of patients with radiation fibrosis syndrome. *Reports of practical oncology and radiotherapy*, 19(1):1–6, 2014.

[50] Jie Deng, Sheila H Ridner, Joseph M Aulino, and Barbara A Murphy. Assessment and measurement of head and neck lymphedema: state-of-the-science and future directions. *Oral oncology*, 51(5):431–437, 2015.

[51] Raghu P Kataru, Itay Wiser, Jung Eun Baik, Hyeung Ju Park, Sonia Rehal, Jin Yeon Shin, and Babak J Mehrara. Fibrosis and secondary lymphedema: chicken or egg? *Translational Research*, 209:68–76, 2019.

[52] Jie Deng, Mary S Dietrich, Kenneth J Niermann, Robert J Sinard, Anthony J Cmelak, Sheila H Ridner, Jill Gilbert, and Barbara A Murphy. Refinement and validation of the head and neck lymphedema and fibrosis symptom inventory. *International Journal of Radiation Oncology* Biology* Physics*, 109(3):747–755, 2021.

[53] Barbara A Murphy and Jie Deng. Advances in supportive care for late effects of head and neck cancer. *Journal of clinical oncology*, 33(29):3314–3321, 2015.

[54] Jie Deng, Sheila H Ridner, Barbara A Murphy, and Mary S Dietrich. Preliminary development of a lymphedema symptom assessment scale for patients with head and neck cancer. *Supportive Care in Cancer*, 20(8):1911–1918, 2012.

[55] Joseph M Aulino, Elizabeth M Wulff-Burchfield, Mary S Dietrich, Sheila H Ridner, Kenneth J Niermann, Jie Deng, Bethany A Rhoten, Jennifer K Doersam, Lee Ann Jarrett, Kyle Mannion, et al. Evaluation of ct changes in the head and neck after cancer treatment: development of a measurement tool. *Lymphatic Research and biology*, 16(1):69–74, 2018.

[56] J-L Gennisson, Thérèse Baldeweck, Mickaël Tanter, Stefan Catheline, Mathias Fink, Laurent Sandrin, Céline Cornillon, and Bernard Querleux. Assessment of elastic parameters of human skin using dynamic elastography. *IEEE transactions on ultrasonics, ferroelectrics, and frequency control*, 51(8):980–989, 2004.

[57] CY Lim, HG Seo, K Kim, SG Chung, and Kwan Sik Seo. Measurement of lymphedema using ultrasonography with the compression method. *Lymphology*, 44(2):72–81, 2011.

[58] Hoda S Hashemi, Stefanie Fallone, Mathieu Boily, Anna Towers, Robert D Kilgour, and Hassan Rivaz. Assessment of mechanical properties of tissue in breast cancer-related lymphedema using ultrasound elastography. *IEEE transactions on ultrasonics, ferroelectrics, and frequency control*, 66(3):541–550, 2018.

[59] Michael Vogt and Helmut Ermert. Development and evaluation of a high-frequency ultrasound-based system for in vivo strain imaging of the skin. *ieee transactions on ultrasonics, ferroelectrics, and frequency control*, 52(3):375–385, 2005.

[60] Yong Hou, Qing-li Zhu, He Liu, Yu-xin Jiang, Liang Wang, Dong Xu, Meng-tao Li, Xiao-feng Zeng, and Feng-chun Zhang. A preliminary study of acoustic radiation force impulse quantification for the assessment of skin in diffuse cutaneous systemic sclerosis. *The Journal of rheumatology*, 42(3):449–455, 2015.

[61] Yujia Yang, Li Qiu, Liyun Wang, Xi Xiang, Yuanjiao Tang, Haocheng Li, and Feng Yan. Quantitative assessment of skin stiffness using ultrasound shear wave elastography in systemic sclerosis. *Ultrasound in Medicine & Biology*, 45(4):902–912, 2019.

[62] Cátia Pinto Carvalho, José Francisco Silva Costa-Júnior, Camilla da Silva Rangel, and Wagner Coelho de Albuquerque Pereira. Measurement of shear wave speed and normalized elastic modulus of human skin with and without dermal striae using shear wave elastography. *Ultrasound in Medicine & Biology*, 47(3):454–470, 2021.

[63] L Pedersen, B Hansen, and GBE Jemec. Mechanical properties of the skin: a comparison between two suction cup methods. *Skin Research and Technology*, 9(2):111–115, 2003.

[64] Tânia Santiago, Begonya Alcacer-Pitarch, Maria João Salvador, Francesco Del Galdo, Anthony C Redmond, and JA Da Silva. A preliminary study using virtual touch imaging and quantification for the assessment of skin stiffness in systemic sclerosis. *Clin Exp Rheumatol*, 34(Suppl 100):137–141, 2016.

[65] Kristy M. Walsh, Mark L. Palmeri, and Brett C. Byram. On-axis acoustic radiation force-based stiffness estimation in phantoms. In *Proc. IEEE Int. Ultrason. Symp. (IUS)*, pages 1–3, Sept. 2016.

[66] Mark L. Palmeri, David Xu, Liang Zhai, and Kathryn R. Nightingale. Acoustic radiation force based quantification of tissue shear modulus within the region of excitation. In *Proc. IEEE Int. Ultrason. Symp. (IUS)*, pages 2009–2012, Nov. 2008.

[67] Douglas M. Dumont and Brett C. Byram. Robust tracking of small displacements with a bayesian estimator. *IEEE Trans. Ultrason., Ferroelectr., Freq. Control*, 63(1):20–34, Jan. 2016.

[68] Douglas M Dumont, Kristy M Walsh, and Brett C Byram. Improving displacement signal-to-noise ratio for low-signal radiation force elasticity imaging using bayesian techniques. *Ultrasound Med. Biol.*, 42(8):1986–1997, Aug. 2016.

[69] C. Bouman and K. Sauer. A generalized gaussian image model for edge-preserving map estimation. *IEEE Trans. Image Process.*, 2(3):296–310, Jul. 1993.

[70] Mark Schmidt. minfunc: unconstrained differentiable multivariate optimization in matlab. http://www.cs.ubc.ca/ schmidtm/Software/minFunc.html, 2005.

[71] Xiaoming Lai and Hans Torp. Interpolation methods for time-delay estimation using cross-correlation method for blood velocity measurement. *IEEE Trans. Ultrason., Ferroelectr., Freq. Control*, 46(2):277–290, Mar. 1999.

[72] Kristy M. Walsh, Douglas M. Dumont, Mark L. Palmeri, and Brett C. Byram. On-axis radiation-force-based quantitative stiffness estimation with a bayesian displacement estimator. In *Proc. IEEE Int. Ultrason. Symp. (IUS)*, pages 1–4, Oct. 2015.

[73] Jørgen Arendt Jensen and Niels Bruun Svendsen. Calculation of pressure fields from arbitrarily shaped, apodized, and excited ultrasound transducers. *IEEE Trans. Ultrason., Ferroelectr., Freq. Control*, 39(2):262–267, Mar. 1992.

[74] Mark L. Palmeri, Stephen A. McAleavey, Gregg E. Trahey, and Kathryn R. Nightingale. Ultrasonic tracking of acoustic radiation force-induced displacements in homogeneous media. *IEEE Trans. Ultrason., Ferroelectr., Freq. Control*, 53(7):1300–1313, Jul. 2006.

[75] Doug M. Giannantonio, Douglas M. Dumont, Gregg E. Trahey, and Brett C. Byram. Comparison of physiological motion filters for in vivo cardiac arfi. *Ultrason. Imag.*, 33(2):89–108, Apr 2011.

[76] JC Bamber and CR Hill. Acoustic properties of normal and cancerous human liveri. dependence on pathological condition. *Ultrasound in medicine & biology*, 7(2):121–133, 1981.

[77] T Lin, J Ophir, and G Potter. Correlations of sound speed with tissue constituents in normal and diffuse liver disease. *Ultrasonic imaging*, 9(1):29–40, 1987.

[78] Zheng Feng Lu, JA Zagzebski, and FT Lee. Ultrasound backscatter and attenuation in human liver with diffuse disease. *Ultrasound in medicine & biology*, 25(7):1047–1054, 1999.

[79] Yufeng Deng, Ned C Rouze, Mark L Palmeri, and Kathryn R Nightingale. Ultrasonic shear wave elasticity imaging sequencing and data processing using a verasonics research scanner. *IEEE transactions on ultrasonics, ferroelectrics, and frequency control*, 64(1):164–176, 2017.

[80] Brian J Fahey, Kathryn R Nightingale, Rendon C Nelson, Mark L Palmeri, and Gregg E Trahey. Acoustic radiation force impulse imaging of the abdomen: demonstration of feasibility and utility. *Ultrasound Med. Biol.*, 31(9):1185–1198, Sept. 2005.

[81] Stephen J Hsu, Richard R Bouchard, Douglas M Dumont, Patrick D Wolf, and Gregg E Trahey. In vivo assessment of myocardial stiffness with acoustic radiation force impulse imaging. *Ultrasound Med. Biol.*, 33(11):1706–1719, Nov. 2007.

[82] Liang Zhai, Thomas J Polascik, Wen-Chi Foo, Stephen Rosenzweig, Mark L Palmeri, John Madden, and Kathryn R Nightingale. Acoustic radiation force impulse imaging

of human prostates: initial in vivo demonstration. *Ultrasound Med. Biol.*, 38(1):50–61, Jan. 2012.

[83] Amy C Sharma, Mary Scott Soo, Gregg E Trahey, and Kathryn R Nightingale. Acoustic radiation force impulse imaging of in vivo breast masses. In *Proc. IEEE Int. Ultrason. Symp. (IUS)*, pages 728–731, Aug. 2004.

[84] Giovanna Ferraioli, Carlo Filice, Laurent Castera, Byung Ihn Choi, Ioan Sporea, Stephanie R Wilson, David Cosgrove, Christoph F Dietrich, Dominique Amy, Jeffrey C Bamber, Richard Barr, Yi-Hong Chou, Hong Ding, Andre Farrokh, Mireen Friedrich-Rust, Timothy J Hall, Kazutaka Nakashima, Kathryn R Nightingale, Mark L Palmeri, Fritz Schafer, Tsuyoshi Shiina, Shinichi Suzuki, and Masatoshi Kudo. Wfumb guidelines and recommendations for clinical use of ultrasound elastography: part 3: liver. *Ultrasound Med. Biol.*, 41(5):1161–1179, May 2015.

[85] Matthew McCormick, Nicholas Rubert, and Tomy Varghese. Bayesian regularization applied to ultrasound strain imaging. *IEEE transactions on biomedical engineering*, 58(6):1612–1620, 2011.

[86] Timothy J Hall, Mehmet Bilgen, Michael F Insana, and Thomas A Krouskop. Phantom materials for elastography. *IEEE transactions on ultrasonics, ferroelectrics, and frequency control*, 44(6):1355–1365, 1997.

[87] Ernest L Madsen, Maritza A Hobson, Hairong Shi, Tomy Varghese, and Gary R Frank. Tissue-mimicking agar/gelatin materials for use in heterogeneous elastography phantoms. *Physics in Medicine & Biology*, 50(23):5597, 2005.

[88] Carolina Amador, Matthew W Urban, Shigao Chen, Qingshan Chen, Kai-Nan An, and James F Greenleaf. Shear elastic modulus estimation from indentation and sduv on gelatin phantoms. *IEEE Transactions on Biomedical Engineering*, 58(6):1706–1714, 2011.

[89] Douglas Dumont, Mark Palmeri, Stephanie Eyerly, Patrick Wolf, and Brett Byram. Feasibility of using a generalized-gaussian markov random field prior for bayesian speckle tracking of small displacements. In *2014 IEEE International Ultrasonics Symposium*, pages 1845–1848. IEEE, 2014.

[90] Erwin Kreyszig, K Stroud, and G Stephenson. Advanced engineering mathematics. *Integration*, 9(4), 2008.

[91] Ken Binmore and Joan Davies. *Calculus: concepts and methods*. Cambridge University Press, 2001.

[92] Su-In Lee, Honglak Lee, Pieter Abbeel, and Andrew Y Ng. Efficient l˜ 1 regularized logistic regression. In *Aaai*, volume 6, pages 401–408, 2006.

[93] Kristy Walsh, Mark Palmeri, and Brett Byram. On-axis acoustic radiation force-based elasticity measurement in homogeneous and layered, skin-mimicking phantoms. In *2018 IEEE International Ultrasonics Symposium (IUS)*, pages 1–3. IEEE, 2018.

[94] Douglas Dumont, Jeremy Dahl, Elizabeth Miller, Jason Allen, Brian Fahey, and Gregg Trahey. Lower-limb vascular imaging with acoustic radiation force elastography: demonstration of in vivo feasibility. *IEEE Trans. Ultrason., Ferroelectr., Freq. Control*, 56(5), 2009.

[95] Tânia Santiago, Eduardo Santos, Barbara Ruaro, Gemma Lepri, Lorraine Green, Marie Wildt, Shinji Watanabe, Alain Lescoat, Roger Hesselstrand, Francesco Del Galdo, et al. Ultrasound and elastography in the assessment of skin involvement in systemic sclerosis: A systematic literature review focusing on validation and standardization–wsf skin ultrasound group. In *Seminars in Arthritis and Rheumatism*, volume 52, page 151954. Elsevier, 2022.